Charge and current responses of spin-orbit coupled two-dimensional materials

DISSERTATION ZUR ERLANGUNG DES DOKTORGRADES DER NATURWISSENSCHAFTEN (DR. RER. NAT.) DER FAKULTÄT FÜR PHYSIK DER UNIVERSITÄT REGENSBURG

vorgelegt von

Andreas Scholz

aus

Regensburg

im

Jahr 2013

Die Arbeit wurde angeleitet von: Prof. Dr. John Schliemann

Promotionsgesuch eingereicht am: 16.10.2013
Das Promotionskolloquium fand statt am: 19.12.2013

Prüfungsausschuss:

Vorsitzender:	Prof. Dr. John Lupton
1. Gutachter:	Prof. Dr. John Schliemann
2. Gutachter:	Prof. Dr. Klaus Richter
weiterer Prüfer:	Prof. Dr. Gunnar Bali

Contents

List of abbreviations

2D	Two-dimensional
2DEG	Two-dimensional electron gas
BZ	Brillouin zone
DF	Dielectric function
DOS	Density of states
EHC	Electron-hole continuum
ELF	Energy loss function
HREELS	High-resolution electron-energy-loss spectroscope
KMM	Kane-Mele model
ML-MDS	Monolayer molybdenum disulfide
OMS	Orbital magnetic susceptibility
QW	Quantum well
RPA	Random Phase Approximation
SOC	Spin-orbit coupling
SOI	Spin-orbit interaction
TB	Tight-binding
TBZ	Time Brillouin zone
THz	Terahertz

Chapter 1.

Introduction

Carbon, one of the lightest elements and a cornerstone of the existence of living beings, has awaken gorgeous hopes among material scientists in the recent decades. Although its two most prominent allotropes, graphite and diamond, have been well-known for hundreds of years, the current interest in carbon-based nanostructures mainly began due to three sequential discoveries: In the 1970s theoretical investigations of Eiji Osawa [1] predicted the stability of large molecules solely made of carbon. These molecules, known as fullerenes, were eventually discovered in 1985 [2] by Robert Curl, Harold Kroto, and Richard Smalley, earning them the Nobel Prize in Chemistry in the year 1996 [3]. Apart from established applications in anti-aging products, the fullerenes are traded as compounds of future semi- and superconducting materials, as catalysts in chemical reactions, and for medical purposes [4]. Only a few years after the experimental proof of the fullerenes succeeded, a serendipity in an electron microscope again demonstrated carbon's manifold appearances after few layers of graphite, wrapped up cylindrically to form so-called carbon nanotubes, were discovered in the early 1990s [5]. The new research field based on carbon nanotubes offers a variety of possible applications such as transistors, energy storages, and as substitutes for heavier materials [6]. Having seen manifestations of carbon in three (graphite and diamond), one (carbon nanotubes), and zero dimensions (fullerenes), it is natural to ask for a stable two-dimensional (2D) configuration. Unfortunately, early theoretical investigations gave a very disappointing answer regarding the crystallographic long-range order in two dimensions, and hence 2D (carbon) lattices were expected not to exist [7, 8].

In fact, until 2004 2D solids were mainly studied in quantum well (QW) heterostructures such as GaAs/GaAlAs compounds, where the charge carrier movement is confined along one direction. This changed in 2004 when the research group of Andre Geim and Konstantin Novoselov isolated, detected, and gated a monolayer of graphite known as graphene for the first time [9]. Although single sheets of graphite had already been reported by Hanns-Peter Boehm in 1962 [10], compared to the mechanical exfoliation method of Geim and Novoselov the reduction of graphite oxide used in Boehm's experiments diminished some of the special characteristics of graphene [11]. Moreover, gating the flake was a subtle point to demonstrate that graphene is a fascinating material not only because of its dimensionality, but also due to its outstanding electrical, mechanical, and optical properties; see Refs. [12, 13] for an overview. As a consequence, the zero-gap semiconduc-

tor graphene with its characteristic linear bands at low energies [14] soon attracted a huge amount of interest in the scientific community due to fundamental questions ('quantum electrodynamics in a pencil trace' [15]), and because of a variety of possible applications [13, 15]. The significance of graphene was even underlined in 2010 when the Nobel Prize of Physics was awarded to Geim and Novoselov 'for groundbreaking experiments regarding the two-dimensional material graphene' [16]. Even nine years after the marvelous experiments of Geim and coworkers, graphene remains one of the most intensively studied materials and an enormous interest still exists in this remarkable carbon-based structure, as evident by the recent funding of the *Graphene Flagship* by the European Union which allocated one billion euro for the next ten years to support scientists working in various research fields of graphene [17].

Since the birth of graphene in 2004 a hunt on other truly 2D materials with prominent characteristics has begun. It has been demonstrated that single sheets of boron nitride [18], molybdenum disulfide [18, 19], and silicon [20, 21] can be isolated and it is very likely that others will follow as time goes by. Moreover, some of the properties of graphene are not set in stone, but they can rather be modified by chemical manipulation. The two most prominent examples are graphane [22, 23, 24] and fluorographene [25, 26]. In the former the carbon atoms are bound to hydrogen atoms which leads to a remarkable band gap opening (of the order of electron Volt), while in the latter fluorine atoms induce a finite magnetization in the sample.

Among the many peculiarities of graphene [12, 13, 15] are the high carrier mobility, allowing quantum Hall measurements even at room temperature, the low resistivity, making graphene potentially useful as a substitute of silicon in transistors, the very large in-plane stiffness leading to relatively high phonon energies [27], and the high absorption rate of 2.3% per layer [28]. Apart from a variety of possible applications such as transistors, solar cells, sensors, or displays, graphene recently came in the focus of plasmonics [29, 30, 31, 32, 33, 34, 35, 36], where density waves created by an incident light beam carry optical signals through a nanostructure. Compared to the surface plasmons in metals, graphene offers a number of striking advantages:

(i) The measured plasmon wavelengths of about 250 nm are very short and in particular roughly 40 times smaller than the wavelength of the laser source [31, 32, 33], which in turn leads to a high localization of the electric field.

(ii) The optical absorption at the plasmon resonance is about one order of magnitude larger than in metals, hence dropping the requirement of having low temperatures in experiments [31].

(iii) The Fermi energy and thus the plasmon wavelength in graphene is widely tunable by means of an electric gate voltage [31, 32, 33]. As very large carrier concentrations up to values of 10^{14} cm^{-2} have been reported in the literature [35], this allows wavelengths ranging from the terahertz (THz) to the visible regime.

(iv) It was demonstrated that the damping rate of the plasmons in graphene can be enhanced by approaching the charge neutrality point, allowing to switch on/off the plasmon propagation depending on the Fermi energy [32].

In order to understand the dynamics of the collective charge excitations in graphene and related materials, a detailed analysis of the dynamical dielectric function (DF), or equivalently of the conductivity is indispensable. The DF is relevant not only in view of plasmonics, but also for the transport characteristics, the screening behavior of the Coulomb potential of charged particles, and the phonon spectra. Moreover, the interaction between electrons and plasmons leads to bound states known as plasmarons [37], which have been observed previously in graphene [38, 39].

The aim of the present work is to give a detailed study of the single- and many-particle properties of three different 2D materials: graphene, a monolayer of molybdenum disulfide (ML-MDS), and p-doped III-V semiconductor QWs. As a generalization of previous works we explicitly take into account the effect of the various types of spin-orbit interactions (SOIs). While SOIs in graphene were initially considered as being negligible [40], recent experimental and theoretical works have demonstrated that spin-orbit coupling (SOC) might be relevant in graphene as the characteristic parameters can be enlarged significantly by changing the environment of the sample [41, 42, 43, 44, 45]. Moreover, the discussion of SOIs in graphene deserves attention also in view of other honeycomb lattices with similar properties such as silicene [46, 47] or ML-MDS [48]. The latter is considered as a possible alternative to graphene and as an auspicious candidate for valley- [49, 50, 51] and spintronics [52] due to the distinct band gap of about 1.82 eV, the large intrinsic SOC of 80 meV [53, 54, 55], and the lack of a center of inversion. On the other hand, quantum well structures provide a fertile ground to investigate the effects of SOIs on the plasmon spectrum due to their inherently large SOIs [56] and because of the established controllability of the Rashba SOC by means of external electric fields [57].

This thesis is organized in the following way: In Chap. 2 we introduce the low-energy description of graphene, ML-MDS, and p-doped III-V semiconductors and discuss the influence of the different types of SOIs on the single-particle properties.

Chapter 3 summarizes the formalism of linear response and introduces the Kubo susceptibility as the central transport quantity. We describe how the Random Phase Approximation (RPA) applied to the charge and current responses can be used to extract information on the collective charge excitations of the system and briefly comment on recent measurements of the plasmon energies in graphene by means of energy loss spectroscopy [58, 59].

In Chapter 4 we study the dielectric properties of graphene in the presence of SOIs of the intrinsic and Rashba type. The main result of this chapter consists in the derivation of closed analytical expressions for the DF in RPA for arbitrary frequency, wave vector, doping, and SOC parameters. We show how SOIs in graphene might be used to change the plasmon energy and lifetime, which in turn might be interesting in view of plasmonics. For a sufficiently large Rashba SOC the system exhibits a new plasmon mode with an energy much larger than those of the long-wavelength result. However, this mode always lies in the region where the creation of electron-hole pairs is permitted and thus has a finite lifetime. From the static limit of the DF the asymptotic behavior of the screened Coulomb potential of a charged impurity is investigated. Away from the charge neutrality point the Coulomb potential exhibits characteristic Friedel oscillations due to the existence of a sharp Fermi surface. In case the spin degeneracy of the bands gets lifted due to the

Rashba SOC, a beating of the Friedel oscillations is predicted.

After discussing the effect of an external charge density we analyze the current response of graphene in Chap. 5. Restricting ourselves in this chapter to the intrinsic SOC, we present analytical results for the transversal and longitudinal parts of the current-current susceptibility for arbitrary frequency, wave vector, and doping. The static limit of the current-current susceptibility allows to derive the orbital and Pauli part of the magnetic susceptibility. The orbital part for undoped graphene is shown to be proportional to the inverse of the SOC strength and in particular diverges for vanishing SOIs. By taking the nonrelativistic limit of gapped graphene, i.e., the limit of a band gap parameter comparable to the Fermi energy, we reproduce the results of an ordinary 2D electron gas (2DEG), but with a pseudospin Zeeman term due to the existence of a pseudospin degree of freedom [60]. The nonrelativistic limit is not of purely academic interest, but is closely related to other honeycomb structures with a large band gap in the energy spectrum such as ML-MDS.

This brings us to Chap. 6 where a numerical discussion of the dynamical DF of ML-MDS within the RPA is carried out. While in graphene damping of plasmons is caused by interband transitions [61, 62], due to the large direct band gap in ML-MDS, collective charge excitations enter the intraband electron-hole continuum (EHC) similar to the situation in 2DEGs [63]. The carrier density dependence of the plasmon frequency in ML-MDS, $\omega_q \propto n^{1/2}$, turns out to be quite different compared to graphene where $\omega_q \propto n^{1/4}$ [62]. Since there is no electron-hole symmetry in ML-MDS, the plasmon energies in p- and n-doped samples clearly differ. Moreover, the breaking of spin degeneracy caused by the large intrinsic SOI leads to a beating of Friedel oscillations for sufficiently high carrier concentrations.

In Chap. 7 we proceed with an investigation of the plasmon spectrum in quasi 2D hole gases, exemplified on GaAs and InAs QWs grown in the [001] direction. In our analysis we explicitly account for SOIs of the Dresselhaus and Rashba type. It is shown that the plasmon dispersion exhibits a pronounced anisotropy being much larger in GaAs compared to InAs. In GaAs this leads to a suppression of plasmons due to Landau damping in some orientations, while others are undamped. Due to the large Rashba contribution in InAs, the lifetime of plasmons can be controlled by changing the magnitude of an electric field. This effect is potentially useful in a plasmon transistor as previously proposed for 2DEGs [64, 65].

The influence of a strong circularly and linearly polarized THz field on a monolayer of graphene is the subject of Chap. 8. As the field drives the sample out of equilibrium, distinct changes in the single-particle properties are expected. It turns out to be possible to induce a gap in the energy spectrum [66, 67] and to close an existing gap by using circularly polarized light. On the other hand, the spectrum becomes strongly anisotropic if the incident light is linearly polarized. We show that the time evolution of the spin polarization and the orbital dynamics of an initial wave packet can be modulated by varying the ratio of the intrinsic and Rashba SOC parameters. Assuming that the system acquires a quasistationary state, the optical conductivity of the irradiated sample is calculated. It is shown that the THz field induces additional steps in the conductivity as reported recently in Ref. [68]. The number of steps in turn depends on the field amplitude and orientation,

as well as on the SOC parameters.

A conclusion of the main results of this thesis, together with a brief outlook on possible extensions can be found in Chap. 9.

In appendices A and B we provide details on the analytical calculations of the free polarizability and transversal part of the current-current susceptibility of graphene.

Chapter 2.

2 Single-particle properties of graphene, monolayer MoS_2, and *p*-doped III-V semiconductors

In the present chapter we introduce the effective low-energy description of graphene, ML-MDS, and *p*-doped III-V semiconductors such as GaAs or InAs. The respective Hamiltonians form the starting point for the following chapters, where many-body effects in the dynamical charge and current susceptibilities are investigated.

We start with a tight-binding (TB) description of graphene in Sec. 2.1.1, where the basic steps to derive an effective Hamiltonian within a single-orbital model are summarized. In Sec. 2.1.2 this model is extended to include the effect of SOIs of the intrinsic and Rashba type within the Kane-Mele model (KMM). As SOIs in graphene are naturally very small, we discuss recent experimental progress and theoretical proposals to enlarge the energy scales of the SOC strengths.

Sec. 2.2 is devoted to ML-MDS, another honeycomb lattice made of sulfur and molybdenum atoms instead of carbon. By comparing the effective two-band Hamiltonian of ML-MDS with that of graphene, we point out formal similarities and quantitative differences. Based on recent results obtained from combined *ab initio* and TB studies, a short discussion of the validity of the two-band model is given.

Finally, in Sec. 2.3 we sketch the derivation of an appropriate model to explain the dynamics of holes in III-V semiconductors, including SOIs arising from bulk and structure inversion asymmetry. We describe how Luttinger's model needs to be extended in order to properly account for a spatial confinement in a quasi 2D QW.

2.1. Graphene

2.1.1. Neglecting spin-orbit interactions

In Fig. 2.1(a) we show the graphene lattice in real space [12, 14, 69]. The lattice can be decomposed into two triangular sublattices, where an atom in sublattice A (B) has three nearest-neighbor carbon atoms located in sublattice B (A). The distance between neighboring atoms is $a_{C-C} \approx 1.42$ Å [12, 14, 69]. The lattice vectors of length $a =$

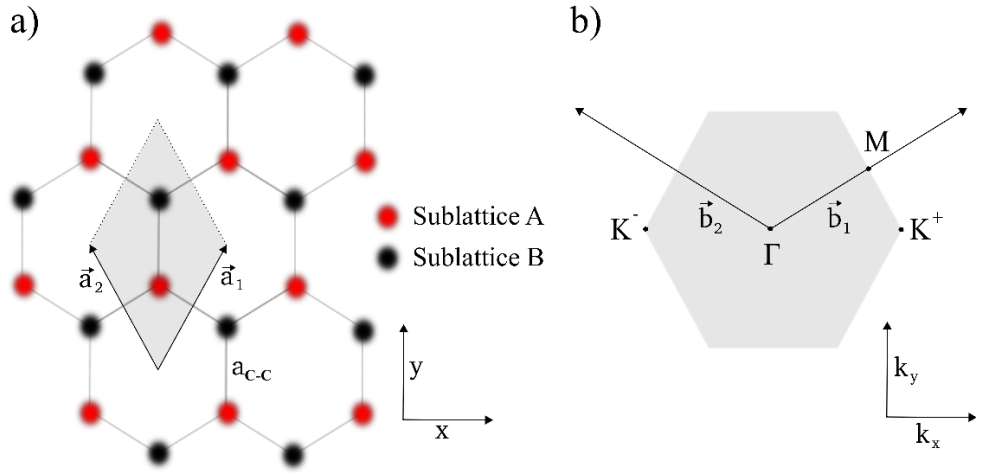

Figure 2.1.: (a) Real space lattice including unit cell (shaded region) and (b) first Brillouin zone of graphene.

$\sqrt{3}a_{C-C} \approx 2.46$ Å are chosen as

$$\boldsymbol{a}_1 = \frac{a}{2}\begin{pmatrix} 1 \\ \sqrt{3} \end{pmatrix} \quad \text{and} \quad \boldsymbol{a}_2 = \frac{a}{2}\begin{pmatrix} -1 \\ \sqrt{3} \end{pmatrix}. \tag{2.1}$$

Within this work all vectors have to be understood as 2D objects in the x-y plane, i.e., the plane where the charge carriers can freely move. Moreover, we set $\hbar = 1$ throughout the thesis. From

$$\boldsymbol{a}_i \cdot \boldsymbol{b}_j = 2\pi\delta_{ij}, \tag{2.2}$$

where δ_{ij} denotes the Kronecker delta, it follows that the reciprocal lattice in Fig. 2.1(b) is spanned by the vectors

$$\boldsymbol{b}_1 = \frac{2\pi}{\sqrt{3}a}\begin{pmatrix} \sqrt{3} \\ 1 \end{pmatrix} \quad \text{and} \quad \boldsymbol{b}_2 = \frac{2\pi}{\sqrt{3}a}\begin{pmatrix} -\sqrt{3} \\ 1 \end{pmatrix}. \tag{2.3}$$

Only two of the six corners of the Brillouin zone (BZ), e.g.,

$$\boldsymbol{K}^\tau = \frac{4\pi}{3a}\begin{pmatrix} \tau \\ 0 \end{pmatrix}, \qquad \text{with} \qquad \tau = \pm 1, \tag{2.4}$$

are independent as the others can be obtained by adding a multiple of the reciprocal lattice vectors $\boldsymbol{b}_1$ and $\boldsymbol{b}_2$ to $\boldsymbol{K}^\tau$. In graphene these special points are usually denoted as Dirac points or valleys.

The energy spectrum of graphene has been known since 1947, when Philip Wallace solved the TB model of the hexagonal carbon lattice in order to obtain information on the band structure of graphite [14]. Within the TB approximation, the solution of the time-independent Schrödinger equation in the presence of a spatially periodic lattice potential

$\mathcal{V}(\boldsymbol{r})$,

$$\left(\frac{\hat{\boldsymbol{p}}^2}{2m_0} + \mathcal{V}(\boldsymbol{r})\right) \Psi_{g,TB}(\boldsymbol{r},\boldsymbol{\kappa}) = E_{g,TB}(\boldsymbol{\kappa})\Psi_{g,TB}(\boldsymbol{r},\boldsymbol{\kappa}), \tag{2.5}$$

where m_0 is the bare electron mass, is written as a linear combination of atomic orbitals, centered around the position of the lattice atoms at

$$\boldsymbol{\mathcal{R}}_A^{n_1 n_2} = \left(\frac{1}{3} + n_1\right)\boldsymbol{a}_1 + \left(\frac{1}{3} + n_2\right)\boldsymbol{a}_2 \tag{2.6}$$

and

$$\boldsymbol{\mathcal{R}}_B^{n_1 n_2} = \left(\frac{2}{3} + n_1\right)\boldsymbol{a}_1 + \left(\frac{2}{3} + n_2\right)\boldsymbol{a}_2, \tag{2.7}$$

with $n_{1/2}$ being integers. Graphene is made of carbon atoms with an electronic configuration of

$$\text{C: [He]}2s^2 2p^2.$$

Three of the valence electrons hybridize in sp^2 orbitals, localizing the atoms at their lattice positions, while the remaining delocalized p_z orbital mainly determines the transport properties of graphene. As the unit cell defined by the lattice vectors $\boldsymbol{a}_{1/2}$ [shaded region in Fig. 2.1(a)] contains two carbon atoms, the solution of Eq. (2.5) is approximated by a superposition of atomic $2p_z$ wave functions $\xi_{2p_z}(\boldsymbol{r})$:

$$\Psi_{g,TB}(\boldsymbol{r},\boldsymbol{\kappa}) = \frac{1}{\sqrt{\mathcal{N}}} \sum_{\nu=A,B} C_\nu \, e^{i\boldsymbol{\kappa}\cdot\boldsymbol{\mathcal{R}}_\nu^{00}} \xi_{2p_z}(\boldsymbol{r} - \boldsymbol{\mathcal{R}}_\nu^{00}), \tag{2.8}$$

where $\mathcal{N}$ is the number of lattice sites. The eigensystem follows from the generalized eigenvalue problem [14, 69]

$$\hat{H}_{g,TB} \begin{pmatrix} C_A \\ C_B \end{pmatrix} = E_{g,TB}(\boldsymbol{\kappa}) \hat{S}_{g,TB} \begin{pmatrix} C_A \\ C_B \end{pmatrix}. \tag{2.9}$$

For the energies this leads to the secular equation

$$\det\left[\hat{H}_{g,TB} - E_{g,TB}(\boldsymbol{\kappa})\hat{S}_{g,TB}\right] = 0. \tag{2.10}$$

Restricting ourselves to nearest-neighbor hopping, the transfer matrix

$$\hat{H}_{g,TB} = \begin{pmatrix} \epsilon_{2p_z} & -t_0 f(\boldsymbol{\kappa}) \\ -t_0 f^*(\boldsymbol{\kappa}) & \epsilon_{2p_z} \end{pmatrix} \tag{2.11}$$

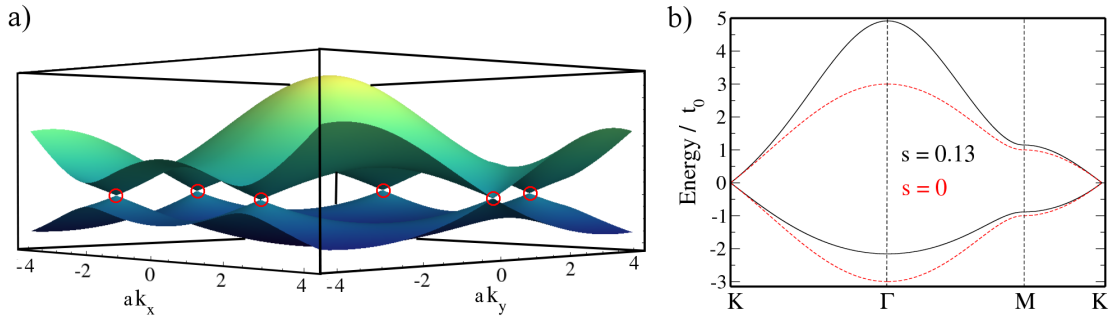

Figure 2.2.: Energy dispersion of graphene (a) within the full BZ and (b) along the high symmetry points.

and overlap integral matrix

$$\hat{S}_{g,TB} = \begin{pmatrix} 1 & sf(\boldsymbol{\kappa}) \\ sf^*(\boldsymbol{\kappa}) & 1 \end{pmatrix} \tag{2.12}$$

contain the on-site energy of the p_z orbitals ϵ_{2p_z}, the function

$$f(\boldsymbol{\kappa}) = 1 + e^{i\boldsymbol{\kappa}\cdot\boldsymbol{a}_1} + e^{i\boldsymbol{\kappa}\cdot\boldsymbol{a}_2}, \tag{2.13}$$

where geometric information of the lattice structure is included, and the nearest-neighbor hopping energy t_0 and overlap integral s. For details on the derivation of the matrix elements of $\hat{H}_{g,TB}$ and $\hat{S}_{g,TB}$ we refer to Refs. [12, 14, 69], where intermediate steps of the calculation can be found. Solving Eq. (2.10), we obtain for the energies

$$E_{g,TB,\pm}(\boldsymbol{\kappa}) = \frac{\epsilon_{2p_z} \pm t_0\,|f(\boldsymbol{\kappa})|}{1 \mp s\,|f(\boldsymbol{\kappa})|}. \tag{2.14}$$

The TB parameters can be determined by comparison with *ab initio* calculations or experimental data, which in turn gives values of $t_0 \approx 3$ eV and $s \approx 0.13$ [12, 69]. The band structure of graphene is shown in Figs. 2.2(a) within the full BZ and (b) along the high symmetry points. Right at the corners of the BZ [indicated by the red circles in Fig. 2.2(a)], the conduction and valence bands touch. For most experimentally relevant carrier densities, $n \lesssim 10^{13}$ cm^{-2}, the dispersion is properly described around the Dirac points and the above Hamiltonian can, up to linear order in momentum, be approximated by ($\boldsymbol{k} = \boldsymbol{K}^\tau + \boldsymbol{\kappa}$) [12]

$$\hat{H}^\tau_{g,0} = v_F \boldsymbol{k}\cdot\hat{\boldsymbol{\sigma}}_\tau + \epsilon_{2p_z}, \quad \text{with} \quad \tau = \pm 1. \tag{2.15}$$

Here, $\hat{\boldsymbol{\sigma}}_\tau = (\tau\hat{\sigma}_x, \hat{\sigma}_y)$ is the vector of Pauli matrices acting on pseudospin space and the Fermi velocity in graphene is defined as

$$v_F = \frac{\sqrt{3}at_0}{2} \approx 10^6 \text{ m/s}. \tag{2.16}$$

Neglecting in the following the overlap integral [which in fact leads only to small changes around the Dirac points; see Fig. 2.2(b)] and choosing the energy reference such that $\epsilon_{2p_z} = 0$, the isotropic dispersion obtained from Eqs. (2.10) and (2.15),[1]

$$E_{g,0,\pm}(k) = \pm v_F k, \tag{2.17}$$

with $k = |\boldsymbol{k}|$, is that of a particle with vanishing effective mass propagating with a constant group velocity v_F.

2.1.2. The influence of spin-orbit interactions

Up to now we did not consider the interplay between the spin degree of freedom and the orbital dynamics. For the inclusion of SOIs one needs to add [56, 70]

$$\hat{H}_{so} = \frac{1}{4m_0^2c^2}\left[\boldsymbol{\nabla}\mathcal{V}(\boldsymbol{r},z)\times\begin{pmatrix}\hat{\boldsymbol{p}}\\ \hat{p}_z\end{pmatrix}\right]\cdot\begin{pmatrix}\hat{\boldsymbol{s}}\\ \hat{s}_z\end{pmatrix} \tag{2.18}$$

to the Schrödinger equation in Eq. (2.5). Here, c denotes the speed of light and $\hat{s}_x, \hat{s}_y, \hat{s}_z$ the Pauli matrices in real spin space. The SOC term Eq. (2.18) can be deduced by taking the nonrelativistic limit of the Dirac Hamiltonian up to second order in the inverse of the rest energy m_0c^2 [56, 70].

In the seminal work of Kane and Mele [71] it has been shown that by treating $\hat{H}_{so}$ perturbatively with respect to $\hat{H}^{\tau}_{g,0}$ [72, 73], SOIs can be incorporated into the low-energy description of graphene by adding the intrinsic

$$\hat{H}^{\tau}_{g,I} = \tau\lambda_I\hat{\sigma}_z\hat{s}_z \tag{2.19}$$

and extrinsic (Rashba) contribution

$$\hat{H}^{\tau}_{g,R} = \lambda_R\left(\tau\hat{\sigma}_x\hat{s}_y - \hat{\sigma}_y\hat{s}_x\right) \tag{2.20}$$

to Eq. (2.15). The resulting Hamiltonian

$$\hat{H}^{\tau}_{g} = v_F\boldsymbol{k}\cdot\hat{\boldsymbol{\sigma}}_{\tau} + \tau\lambda_I\hat{\sigma}_z\hat{s}_z + \lambda_R\left(\tau\hat{\sigma}_x\hat{s}_y - \hat{\sigma}_y\hat{s}_x\right) \tag{2.21}$$

is known as the Kane-Mele model of topological insulators. While the intrinsic part is always present, the Rashba SOC arises if structure inversion symmetry becomes broken. This can be done experimentally by applying an external electric field perpendicular to the graphene plane, or by putting graphene on a substrate. The isotropic energies of the KMM,

$$E_{g,\alpha\beta}(k) = \alpha\,\lambda_R + \beta\,\sqrt{v_F^2k^2 + \left(\lambda_R - \alpha\lambda_I\right)^2}, \quad \text{with} \quad \alpha,\beta = \pm 1, \tag{2.22}$$

are shown in Fig. 2.3 for three different combinations of the SOC parameters: $\lambda_I = 2\lambda_R$, $\lambda_I = \lambda_R$, and $\lambda_I = \lambda_R/2$. For $\lambda_R \neq 0$ the spin degeneracy of the bands is lifted and the

[1] Notice that the index τ is missing in Eq. (2.17) as the energies are the same for both valleys.

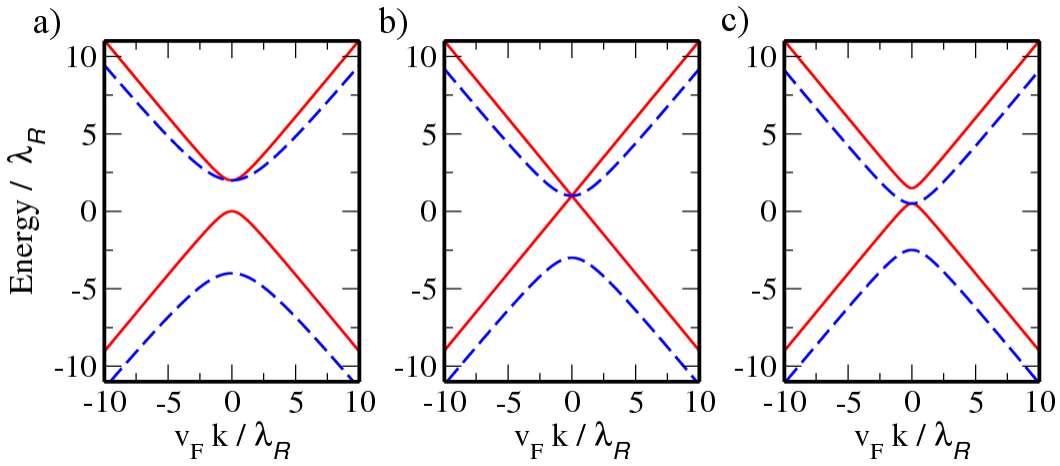

Figure 2.3.: Energy dispersion of graphene for various combinations of the SOC parameters: (a) $\lambda_I = 2\lambda_R$, (b) $\lambda_I = \lambda_R$, and (c) $\lambda_I = \lambda_R/2$. The solid red lines are for $E_{+\pm}$, the dashed blue lines for $E_{-\pm}$.

Fermi contour consists of two concentric circles with radii given by

$$k_{F\pm} = \sqrt{\mu\left(\mu \mp 2\lambda_R\right) \pm 2\lambda_R\lambda_I - \lambda_I^2}/v_F. \tag{2.23}$$

For a sufficiently large intrinsic coupling parameter, $\lambda_I > \lambda_R$, the system exhibits a band gap in the bulk. If the sample becomes spatially confined along one direction, gapless edge states occur and the system is in the quantum spin Hall phase [71]. In the other case of $\lambda_R > \lambda_I$, the valence and conduction bands always touch at the K points and the system behaves as an ordinary semimetal. At the point where $\lambda_R = \lambda_I$, two of the four bands become linear and a threefold degeneracy occurs at the Dirac points.

Let us now discuss the importance of SOIs in typical graphene samples. As graphene is composed of relatively light (carbon) atoms,[2] SOIs in graphene are expected to be small. After some controversy regarding the actual values of the intrinsic and Rashba spin-orbit coefficients, ranging from 1 μeV to 200 μeV for λ_I [71, 72, 74], it was eventually found that the values are close to $\lambda_I = 12$ μeV and $\lambda_R = 5$ μeV for an electric field of 1 V/nm [40, 75]. In order to obtain these numbers it turned out to be necessary to also include the d orbitals as they give the dominant contribution to λ_I (roughly 95%) and to consider σ-π mixing for the Rashba coefficient. Due to the small values of λ_R and λ_I, in the beginning the focus of graphene research was mainly set on spin-independent phenomena. However, recent experimental and theoretical works have impressively demonstrated that SOC effects might be relevant as the characteristic parameters can be enlarged significantly by changing the environment of the sample [41, 42, 43, 44, 45]. As an example, we mention Ref. [44], where it was predicted that the intrinsic contribution can be enlarged up to $\lambda_I \approx 10$ meV, i.e., by three orders of magnitude, if the system is doped with suitable adatoms such as thallium. Alternatively, putting graphene on a Ni(111) surface, as described in the experiment of

[2]The atomic spin-orbit splitting of the carbon $2p_z$ orbitals is about 8 meV [73].

Ref. [41], enhances the Rashba contribution to a remarkable value of $\lambda_R \approx 225$ meV.[3]

Finally, we want to point out a formal similarity between the KMM and the low-energy Hamiltonian of bilayer graphene. Restricting ourselves to nearest-neighbor and interlayer hopping, i.e., neglecting higher order terms such as trigonal warping, bilayer graphene can be described by two monolayer graphene Hamiltonians, coupled by the interlayer hopping $t_{IL} \approx 0.38$ eV [76]:

$$\hat{H}^{\tau}_{BLG} = \begin{pmatrix} \hat{H}^{\tau}_{g} & 0 & 0 \\ & t_{IL} & 0 \\ 0 & t_{IL} & \hat{H}^{\tau}_{g} \\ 0 & 0 & \end{pmatrix}. \tag{2.24}$$

The KMM in Eq. (2.21) with only Rashba SOC taken into account can now be mapped onto the bilayer Hamiltonian of Eq. (2.24), relating the interlayer constant to the Rashba coefficient via

$$\pm 2i\lambda_R \to t_{IL}. \tag{2.25}$$

While the energies of bilayer graphene equal that of Eq. (2.22) (with $\lambda_I = 0$),

$$E_{BLG,\alpha\beta}(k) = \frac{\alpha\, t_{IL}}{2} + \beta \sqrt{v_F^2 k^2 + \left(\frac{t_{IL}}{2}\right)^2}, \quad \text{with} \quad \alpha, \beta = \pm 1, \tag{2.26}$$

the eigenstates only differ by a unitary transformation. Therefore, some of our findings, such as the analytical solution of the free polarizability of graphene in the presence of a purely Rashba SOC discussed in Section 4, can also be applied to bilayer graphene.

2.2. Monolayer MoS_2

As mentioned in the introductory chapter, another promising 2D material that has attracted a lot of attention in the last years is ML-MDS. In the unit cell the molybdenum atom in ML-MDS is arranged in-between two sulfur layers; see Fig. 2.4(a). In top view [Fig. 2.4(b)], both the ML-MDS lattice and BZ show the same hexagonal structure as graphene. However, the electronic configuration of the constituents,

$$\mathrm{S} : [\mathrm{Ne}]3s^2 3p^4 \qquad \text{and} \qquad \mathrm{Mo} : [\mathrm{Kr}]4d^5 5s^1,$$

and the spatial arrangement of the atoms (compared to graphene the lattice is strongly buckled) make the derivation of an adequate TB model much more complicated than in graphene. Moreover, as ML-MDS lacks inversion symmetry and due to the influence of the d orbitals of molybdenum, SOIs are generally expected to be important. As described

[3] It should be emphasized that these samples can no longer be considered as *graphene*, but rather as *graphene-like* as the influence of the adatoms and charge transfer to the substrate cannot be neglected. For the discussion in the following chapters, however, the term *spin-orbit coupled graphene* will be used for all kinds of materials that can effectively be described by the KMM model of Eq. (2.21), independently of the physical origin of the large SOC contributions.

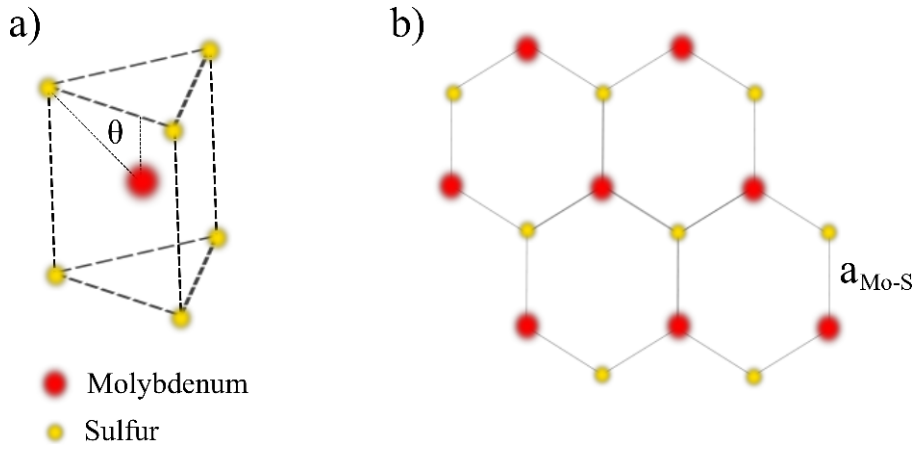

Figure 2.4.: (a) Unit cell and (b) top view of the ML-MDS lattice.

in Ref. [54], a possible starting point is to construct the basis orbitals of the TB model by linear combinations of the d_{z^2}, $d_{x^2-y^2}$, and d_{xy} orbitals of molybdenum, and the p_x and p_y orbitals of sulfur, where for each spin component[4] one ends up with a seven-dimensional TB Hamiltonian.

As in graphene, the valence (conduction) band maxima (minima) in ML-MDS appear at the corners of the BZ, where low-energy transport will be most important. Around the K points, the seven band TB Hamiltonian can further be reduced to an effective two-band model by means of Löwdin partitioning [54, 55]:

$$\begin{aligned}\hat{H}_m^{\tau s} =& \frac{\Delta}{2}\hat{\sigma}_z + \tau s\lambda_I \frac{1-\hat{\sigma}_z}{2} + t_0 a_0 \boldsymbol{k}\cdot\hat{\boldsymbol{\sigma}}_\tau \\ &+ \frac{k^2}{4m_0}\left(\alpha+\beta\hat{\sigma}_z\right) + t_1 a_0^2 \boldsymbol{k}\cdot\hat{\boldsymbol{\sigma}}_\tau^* \hat{\sigma}_x \boldsymbol{k}\cdot\hat{\boldsymbol{\sigma}}_\tau^*,\end{aligned} \tag{2.27}$$

where $\tau, s = \pm 1$ denote the valley and real spin components, respectively. The analytical solution of the energies obtained from Eq. (2.27),

$$\begin{aligned}E_{m,\pm}^{\tau s}(\boldsymbol{k}) =& \frac{\alpha}{4m_0}k^2 + \frac{s\tau\lambda_I}{2} \pm \Bigg\{\left(a_0^4 t_1^2 + \frac{\beta^2}{16m_0^2}\right)k^4 + \left(\frac{\Delta - s\tau\lambda_I}{2}\right)^2 \\ &+ k^2\left[a_0^2 t_0^2 + \frac{\beta\left(\Delta - s\tau\lambda_I\right)}{4m_0}\right] + 2\tau t_0 t_1 a_0^3 k^3 \cos\left(3\phi_k\right)\Bigg\}^{1/2},\end{aligned} \tag{2.28}$$

where $\tan\phi_k = k_y/k_x$ is the in-plane angle, is shown in Fig. 2.5 for both valley and spin polarizations. Table 2.1 summarizes the band parameters of ML-MDS according to Ref. [54]. Due to the large value of the staggered potential $\Delta = 1.9$ eV, a distinct energy gap of 1.82 eV separates the valence and conduction bands. As Eq. (2.28) is not

[4]Notice that, as for graphene, spin remains a good quantum number even in the presence of intrinsic SOIs. This changes if additionally the Rashba contribution is considered. However, in the following we neglect the Rashba term in ML-MDS due its small effect on the energy spectrum.

t_0	a_{Mo-S}	θ	$a_0 = a_{Mo-S}\cos\theta$	Δ	λ_I	α	β
1.68 eV	2.43 Å	40.7 °	1.87 Å	1.9 eV	80 meV	0.43	2.21

Table 2.1.: Band parameters of ML-MDS. a_{Mo-S} is the length of the Mo-S bond and $\theta = 40.7°$ the angle between the x-y plane and the Mo-S bond; see Fig. 2.4. Values taken from Ref. [54].

symmetric with respect to a sign change in λ_I, the intrinsic SOC furthermore lifts the spin degeneracy of the bands. While the valence band degeneracy is clearly lifted even at $k = 0$, the conduction bands remain degenerate at the K points, but differ slightly for larger momenta due to the different curvature of the bands; see Fig. 2.5. Because of time-reversal symmetry the corresponding shift in energy has to be opposite at the two valleys, where for $\tau = +1$ ($\tau = -1$) the $s = +1$ ($s = -1$) component is energetically higher. The trigonal warping term proportional to t_1 causes the spectrum to be anisotropic. However, as $t_1 = 0.1$ eV is small compared to the other energies, this anisotropy is weak and hence we plot only a single in-plane angle of $\phi_k = 0°$.

Having a closer look on the low-energy model of ML-MDS, we notice that the first line in Eq. (2.27) is essentially the Hamiltonian of gapped graphene (i.e., Eq. (2.21) with $\lambda_I \neq 0$ and $\lambda_R = 0$). Here, each contribution with valley τ and spin s is described by an effective mass term given by

$$\tilde{\lambda}_I^{\tau s} = \frac{\Delta}{2} - \frac{s\tau\lambda_I}{2} \tag{2.29}$$

and a shifted Fermi energy of

$$\tilde{\mu}^{\tau s} = \mu - \frac{s\tau\lambda_I}{2}. \tag{2.30}$$

In fact, in Ref. [53] the effective TB Hamiltonian of ML-MDS was found to be

$$\hat{H}^{\tau s}_{m,simp} = \frac{\Delta}{2}\hat{\sigma}_z + \tau s\lambda_I\frac{1-\hat{\sigma}_z}{2} + t_0 a_0 \boldsymbol{k}\cdot\hat{\boldsymbol{\sigma}}_\tau. \tag{2.31}$$

However, it was pointed out later that Eq. (2.31) is not sufficient to properly describe recent *ab initio* data [54, 55], where different electron and hole masses were reported. We should also mention that in Ref. [77] the band structures of ML-MDS and multilayer MoS_2 were investigated within the full BZ; the resulting Hamiltonian turned out to be a further generalization of Eq. (2.27). One of the findings of Ref. [77] and of previous works [55, 78, 79] was that additional band extremes close to the K point minima and maxima might be relevant for transport. These additional bands, at the Γ point for holes and between the K and Γ point for electrons, are not taken into account in Eq. (2.27). For the carrier densities used in Chap. 6, $n = 10^{12}$ cm^{-2} (comparable to the experiment in Ref. [80]) and $5 \cdot 10^{13}$ cm^{-2} (where both valence bands are filled in the p-doped case), we will neglect the influence of the higher bands since the additional extremes are expected to be important only for densities larger than 10^{14} cm^{-2} and the two-band model in Eq. (2.27) should give appropriate results [55, 79]. However, a detailed analysis of the effect of the full BZ on the charge response [81] is left open for future works.

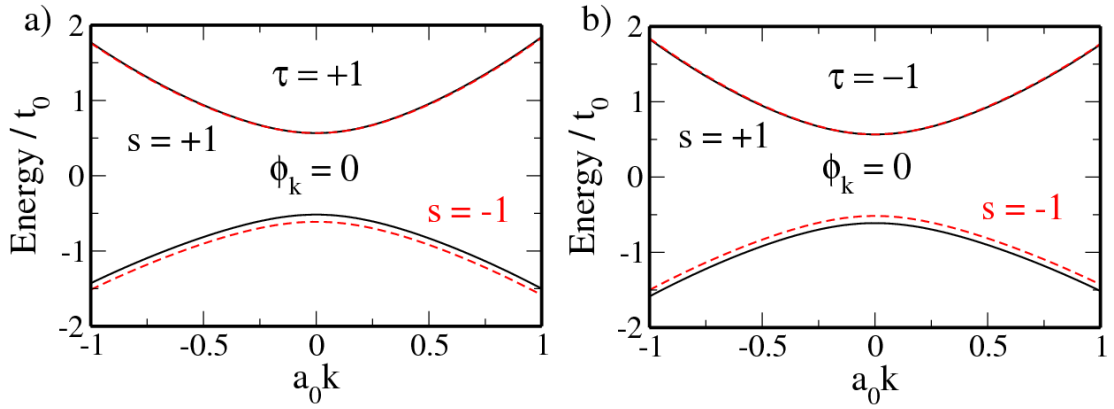

Figure 2.5.: Energy spectrum of ML-MDS around the K points for (a) $\tau = +1$ and (b) $\tau = -1$ for the real spin component $s = +1$ (solid black) and $s = -1$ (dashed red). The in-plane angle $\tan\phi_k = k_y/k_x$ was set to $\phi_k = 0°$.

Let us finally comment on two further things: First of all, even though the models of graphene Eq. (2.21) and ML-MDS Eqs. (2.27) and (2.31), respectively, share several formal similarities, large quantitative differences appear. While the band gap in graphene (of a few μeV) is naturally very small, the valence and conduction bands in ML-MDS are largely separated by 1.82 eV. Moreover, the intrinsic SOC term in ML-MDS is more than three orders of magnitude larger than that in graphene, resulting in a distinct spin splitting of the valence bands. Second, it is worth noticing that for an experimental realization of devices like transistors, the combination of various 2D materials can be used in order to tailor the band structure of a heterojunction according to our requirements. As an example, we mention Ref. [78], where *ab initio* calculations demonstrate the possibility to adjust the size of the band gap of a MoS_2-WS_2 bilayer compared to homogeneous compounds such as MoS_2-MoS_2 or WS_2-WS_2, and even to transform the latter from indirect to direct band gap semiconductors.

2.3. Luttinger's Hamiltonian for *p*-doped III-V semiconductors

Let us now turn to the single-particle description of holes in III-V semiconductors. In the following we restrict ourselves to GaAs and InAs as representatives, as both materials are commonly used in spintronic experiments [57]. Due to the relatively large Rashba SOC, InAs seems to be a promising candidate to manipulate the many-body properties of a QW by adjusting the SOC strength. In Chap. 7 we will discuss this point in view of the plasmon spectrum.

For an effective description of III-V semiconductors one could derive a suitable TB model similar to graphene or ML-MDS [82, 83]. However, for transport calculations (especially in view of an analytical treatment), it is often more convenient to describe the topmost valence bands by Luttinger's model [56, 83, 84]. Due to Bloch's theorem the analytical

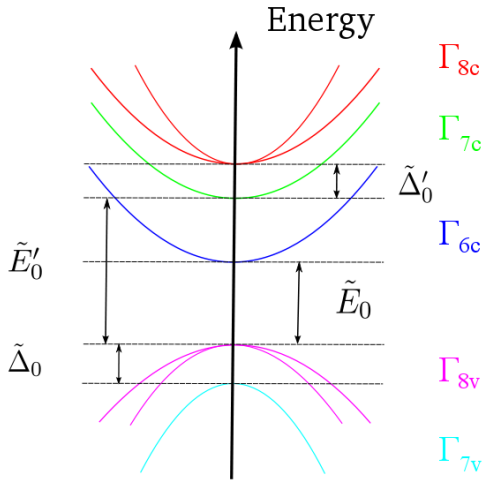

Figure 2.6.: Schematic plot of the band structure of III-V semiconductors such as GaAs or InAs for the eight lowest conduction and six highest valence bands.

solution of Schrödinger's equation with a spatially periodic potential is of the form[5]

$$\Psi_\nu(\boldsymbol{r}, z; \boldsymbol{k}, k_z) = e^{i(\boldsymbol{k}\cdot\boldsymbol{r}+k_z z)} u_\nu(\boldsymbol{r}, z; \boldsymbol{k}, k_z), \tag{2.32}$$

where ν is a set of quantum numbers and u_ν a lattice periodic wave function. As arsenic, gallium, and indium are relatively heavy atoms, the effect of SOIs, being proportional to the squared of the atomic number, has to be taken into account from the beginning. Combining the Bloch wave function in Eq. (2.32) with Eqs. (2.5) and (2.18), we obtain a differential equation for u_ν:

$$\left[\frac{\hat{\boldsymbol{p}}^2 + \hat{p}_z^2}{2m_0} + \mathcal{V}(\boldsymbol{r}, z) + \frac{\boldsymbol{k}^2 + k_z^2}{2m_0} + \frac{\boldsymbol{k}\cdot\hat{\boldsymbol{p}} + k_z\hat{p}_z}{m_0} + \frac{\left[\boldsymbol{\nabla}\mathcal{V}(\boldsymbol{r}, z) \times \begin{pmatrix}\hat{\boldsymbol{p}}\\ \hat{p}_z\end{pmatrix}\right] \cdot \begin{pmatrix}\hat{\boldsymbol{s}}\\ \hat{s}_z\end{pmatrix}}{4m_0^2c^2} \right.$$
$$\left. + \frac{\left[\boldsymbol{\nabla}\mathcal{V}(\boldsymbol{r}, z) \times \begin{pmatrix}\boldsymbol{k}\\ k_z\end{pmatrix}\right] \cdot \begin{pmatrix}\hat{\boldsymbol{s}}\\ \hat{s}_z\end{pmatrix}}{4m_0^2c^2} \right] u_\nu(\boldsymbol{r}, z; \boldsymbol{k}, k_z) = E_\nu(\boldsymbol{k}, k_z) u_\nu(\boldsymbol{r}, z; \boldsymbol{k}, k_z). \tag{2.33}$$

Usually, the crystal momentum $|\boldsymbol{k}|$ is small compared to the momentum of the holes $|\boldsymbol{p}|$ (the expectation value of the momentum operator $\hat{\boldsymbol{p}} = -i\boldsymbol{\nabla}$) and we can neglect the last term on the left-hand side [56]. As the conduction band minima and valence band maxima in GaAs and InAs appear at the Γ point, we express the lattice periodic wave function for

[5] Notice that when we discuss III-V semiconductors in this section and in Chap. 7, the wave vector $\boldsymbol{k}$ is measured with respect to the center of the BZ and not with respect to some K point.

finite wave vectors in terms of the Γ point solutions v_α [56, 83]:

$$u_\nu(\boldsymbol{r}, z; \boldsymbol{k}, k_z) = \sum_{\alpha'} c_{\nu\alpha'}(\boldsymbol{k}, k_z) v_{\alpha'}(\boldsymbol{r}, z). \tag{2.34}$$

Combining Eqs. (2.34) and (2.33) and projecting the result to v_α^*, the expansion coefficients $c_{\nu\alpha}$ and the corresponding energies E_ν follow from the eigenvalue problem

$$\sum_{\alpha'} \left[\left(E_{\alpha'}(0) + \frac{\boldsymbol{k}^2 + k_z^2}{2m_0} \right) \delta_{\alpha\alpha'} + \frac{1}{m_0} \begin{pmatrix} \boldsymbol{k} \\ k_z \end{pmatrix} \cdot \begin{pmatrix} \boldsymbol{P}_{\alpha\alpha'} \\ P_{z,\alpha\alpha'} \end{pmatrix} + \frac{1}{4m_0^2 c^2} \Sigma_{\alpha\alpha'} \right] c_{\nu\alpha'}(\boldsymbol{k}, k_z) = E_\nu(\boldsymbol{k}, k_z) c_{\nu\alpha}(\boldsymbol{k}, k_z). \tag{2.35}$$

Besides the usual kinetic part $(\boldsymbol{k}^2 + k_z^2)/2m_0$, Eq. (2.35) contains the band offsets $E_\alpha(0)$, and the off-diagonal momentum

$$\begin{pmatrix} \boldsymbol{P}_{\alpha\alpha'} \\ P_{z,\alpha\alpha'} \end{pmatrix} = \int d^3r \; v_\alpha^*(\boldsymbol{r}, z) \begin{pmatrix} \hat{\boldsymbol{p}} \\ \hat{p}_z \end{pmatrix} v_{\alpha'}(\boldsymbol{r}, z) \tag{2.36}$$

and SOC matrix elements

$$\Sigma_{\alpha\alpha'} = \int d^3r \; v_\alpha^*(\boldsymbol{r}, z) \left[\boldsymbol{\nabla} \mathcal{V}(\boldsymbol{r}, z) \times \begin{pmatrix} \hat{\boldsymbol{p}} \\ \hat{p}_z \end{pmatrix} \right] \cdot \begin{pmatrix} \hat{\boldsymbol{s}} \\ \hat{s}_z \end{pmatrix} v_{\alpha'}(\boldsymbol{r}, z). \tag{2.37}$$

By diagonalization of the matrix in Eq. (2.35), the energies and wave functions can be obtained for arbitrary wave vectors. In order to allow further analytical or numerical progress, it is necessary to simplify Eq. (2.35) by taking into account only a limited amount of bands exactly, while the others are treated perturbatively. Within the extended Kane model [56, 85, 86], we restrict ourselves to the eight lowest conduction [Γ_{7c} (two), Γ_{6c} (two), and Γ_{8c} (four)] and six highest valence bands [Γ_{7v} (two) and Γ_{8v} (four)]; see Fig. 2.6 for a schematic plot of the band structure. The corresponding Hamiltonian then reads [56]:

$$\hat{H}_{eKM} = \begin{pmatrix} \hat{H}_{8c8c} & \hat{H}_{8c7c} & \hat{H}_{8c6c} & \hat{H}_{8c8v} & \hat{H}_{8c7v} \\ \hat{H}_{7c8c} & \hat{H}_{7c7c} & \hat{H}_{7c6c} & \hat{H}_{7c8v} & \hat{H}_{7c7v} \\ \hat{H}_{6c8c} & \hat{H}_{6c7c} & \hat{H}_{6c6c} & \hat{H}_{6c8v} & \hat{H}_{6c7v} \\ \hat{H}_{8v8c} & \hat{H}_{8v7c} & \hat{H}_{8v6c} & \hat{H}_{8v8v} & \hat{H}_{8v7v} \\ \hat{H}_{7v8c} & \hat{H}_{7v7c} & \hat{H}_{7v6c} & \hat{H}_{7v8v} & \hat{H}_{7v7v} \end{pmatrix}. \tag{2.38}$$

Choosing the energy reference at the top of the valence band, in the p-doped case we can approximate the block-diagonal parts of the conduction bands by [85]

$$\hat{H}_{6c6c} = \tilde{E}_0 \begin{pmatrix} 1 & 0 \\ 0 & 1 \end{pmatrix} \quad , \quad \hat{H}_{7c7c} = \tilde{E}_0' \begin{pmatrix} 1 & 0 \\ 0 & 1 \end{pmatrix} \quad , \quad \hat{H}_{8c8c} = \left(\tilde{E}_0' + \tilde{\Delta}_0' \right) \begin{pmatrix} 1 & 0 & 0 & 0 \\ 0 & 1 & 0 & 0 \\ 0 & 0 & 1 & 0 \\ 0 & 0 & 0 & 1 \end{pmatrix}, \tag{2.39}$$

	γ_1	γ_2	γ_3	C_k (eVÅ)	b_{41}^{8v8v} (eVÅ^3)	r_{41}^{8v8v} (eÅ^2)	ϵ_r	E_0 (meV)
GaAs	6.85	2.10	2.90	-0.0034	-81.93	-14.62	12.5	6.4
InAs	20.40	8.30	9.10	-0.0112	-50.18	-159.9	14.6	19.3

Table 2.2.: Band structure and SOC parameters of GaAs and InAs. Values taken from Ref. [56]. ϵ_r is the background dielectric constant (taken from Ref. [87]) and $E_0 = \gamma_1\pi^2/2m_0d^2$ the size-quantization scale of a $d = 20$ nm thick QW (see Chap. 7).

and the valence bands by

$$\hat{H}_{8v8v} = -\frac{\boldsymbol{k}^2 + k_z^2}{2m_0}\begin{pmatrix}1&0&0&0\\0&1&0&0\\0&0&1&0\\0&0&0&1\end{pmatrix} \quad , \quad \hat{H}_{7v7v} = -\left(\frac{\boldsymbol{k}^2 + k_z^2}{2m_0} + \tilde{\Delta}_0\right)\begin{pmatrix}1&0\\0&1\end{pmatrix}. \tag{2.40}$$

The various energies ($\tilde{E}_0^{(\prime)}$ and $\tilde{\Delta}_0^{(\prime)}$) are defined in Fig. 2.6. If we now use Löwdin's method to decouple the p-like conduction bands Γ_{7c} and Γ_{8c}, and in a subsequent step do the same with the s-like Γ_{6c} bands, we end up with a 6×6 Hamiltonian for the heavy hole, light hole, and split-off bands. Neglecting furthermore the effect of the mixing matrix elements between Γ_{8v} and Γ_{7v}, which in turn is a reasonable approximation in GaAs and InAs [56], one finally arrives at an Hamiltonian of the form [85]:

$$\hat{H}_{VB} = \begin{pmatrix}\hat{H}_{L,0} & 0\\ 0 & \hat{H}_{sp-o}\end{pmatrix}. \tag{2.41}$$

Here, $\hat{H}_{sp-o}$ describes the split-off bands (Γ_{7v}) and $\hat{H}_{L,0}$ is Luttinger's Hamiltonian for the four topmost (Γ_{8v}) valence bands. The influence of the conduction bands is taken into account in $\hat{H}_{VB}$ up to order $1/\tilde{E}_0$ in the fundamental gap. After carrying out the elongate steps of the calculation, as can be partly found in Refs. [56, 83], Luttinger's model explicitly reads:

$$\begin{aligned}\hat{H}_{L,0} = &-\frac{1}{2m_0}\left[\left(\gamma_1 + \frac{5}{2}\gamma_2\right)\left(k_x^2 + k_y^2 + k_z^2\right) - 2\gamma_2\left(k_x\hat{J}_x + k_y\hat{J}_y + k_z\hat{J}_z\right)^2\right]\\ &+ \frac{\gamma_3 - \gamma_2}{m_0}\left[k_xk_z\left\{\hat{J}_x, \hat{J}_z\right\} + k_yk_z\left\{\hat{J}_y, \hat{J}_z\right\} + k_xk_y\left\{\hat{J}_x, \hat{J}_y\right\}\right].\end{aligned} \tag{2.42}$$

Here $\{.,.\}$ is the anticommutator. The values for the Kohn-Luttinger parameters γ_1, γ_2, and γ_3 in GaAs and InAs can be found in Table 2.2. The spin-3/2 matrices are defined as

$$\hat{J}_x = \frac{1}{2}\begin{pmatrix}0&\sqrt{3}&0&0\\\sqrt{3}&0&2&0\\0&2&0&\sqrt{3}\\0&0&\sqrt{3}&0\end{pmatrix} \quad , \quad \hat{J}_y = \frac{1}{2}\begin{pmatrix}0&-i\sqrt{3}&0&0\\i\sqrt{3}&0&-2i&0\\0&2i&0&-i\sqrt{3}\\0&0&i\sqrt{3}&0\end{pmatrix}, \tag{2.43}$$

and

$$\hat{J}_z = \frac{1}{2}\begin{pmatrix} 3 & 0 & 0 & 0 \\ 0 & 1 & 0 & 0 \\ 0 & 0 & -1 & 0 \\ 0 & 0 & 0 & -3 \end{pmatrix}. \tag{2.44}$$

Often $\hat{H}_{L,0}$ is simplified by equating

$$\gamma_2 = \gamma_3 = \bar{\gamma} \equiv \frac{2\gamma_2 + 3\gamma_3}{5}. \tag{2.45}$$

In this case the second line in Eq. (2.42) vanishes. The advantage of this (spherical) approximation is the relative simplicity of the energy spectrum. In three dimensions the subsequent twofold spin-degenerate bands then read

$$E^{sp}_{h/l}(\boldsymbol{k}, k_z) = -\frac{\boldsymbol{k}^2 + k_z^2}{2m_{h/l}}\,, \tag{2.46}$$

where

$$m_{h/l} = \frac{m_0}{\gamma_1 \mp 2\bar{\gamma}} \tag{2.47}$$

are the heavy and light hole masses. While the valence band energies in Eq. (2.46) resemble those of an ordinary electron gas, the corresponding eigenstates turn out to be clearly more complicated due to their nontrivial spin structure [88]. However, if the relative difference of γ_2 and γ_3 is large, the anisotropic terms might be important and can lead to interesting physics. In Chap. 7 we will discuss this point further in context of the plasmon spectrum.

Apart from Luttinger's Hamiltonian in Eq. (2.42), the extended Kane model features additional contributions in systems that lack a center of inversion. We distinguish between bulk inversion asymmetry, which is an intrinsic property and thus always present in zinc blende crystals, and structure inversion asymmetry, e.g., due to a suitably chosen electric field $(\boldsymbol{E}, E_z)$. In the former, Eq. (2.42) needs to be supplemented by the Dresselhaus term [89]

$$\begin{aligned}\hat{H}_D =& \frac{2C_k}{\sqrt{3}}\left[k_x\left\{\hat{J}_x, \hat{J}_y^2 - \hat{J}_z^2\right\} + k_y\left\{\hat{J}_y, \hat{J}_z^2 - \hat{J}_x^2\right\} + k_z\left\{\hat{J}_z, \hat{J}_x^2 - \hat{J}_y^2\right\}\right] \\ &+ b_{41}^{8v8v}\left[\left\{k_x, k_y^2 - k_z^2\right\}\hat{J}_x + \left\{k_y, k_z^2 - k_x^2\right\}\hat{J}_y + \left\{k_z, k_x^2 - k_y^2\right\}\hat{J}_z\right],\end{aligned} \tag{2.48}$$

while the latter leads to the Rashba contribution [90]

$$\hat{H}_R = r_{41}^{8v8v}\left[(k_y E_z - k_z E_y)\,\hat{J}_x + (k_z E_x - k_x E_z)\,\hat{J}_y + (k_x E_y - k_y E_x)\,\hat{J}_z\right]. \tag{2.49}$$

The SOC parameters C_k, b_{41}^{8v8v}, and r_{41}^{8v8v} are summarized in Table 2.2 for GaAs and InAs.[6]

So far we have introduced an analytical description of holes in bulk zinc blende materials. In the following we constrain the system along one direction, assuming a hard-wall confinement in the [001] direction. To this end we express the above Hamiltonians in Eqs. (2.42), (2.48), and (2.49) in the basis of the subband functions

$$\varphi_n(z) = \sqrt{\frac{2}{d}} \sin\left(\frac{n\pi z}{d}\right), \qquad n \in \mathbb{N}, \tag{2.50}$$

with d being the width of the QW. Accordingly, the numbers $(\boldsymbol{k}, k_z)$ need to be substituted by the corresponding momentum operators $(\hat{\boldsymbol{p}}, \hat{p}_z) = -i\boldsymbol{\nabla}$. By diagonalization of the new matrix that contains blocks of four-dimensional Hamiltonians, each given by the projection

$$\left\langle \varphi_n | \hat{H}_{L,0} + \hat{H}_D + \hat{H}_R | \varphi_m \right\rangle, \tag{2.51}$$

the subband energies and states can be found. For the expectation values of the momentum operator in growth direction this leads to

$$\left\langle \varphi_n \middle| \hat{p}_z \middle| \varphi_m \right\rangle = \frac{4imn}{d\,(m^2 - n^2)} \sum_{i=0}^{\infty} \delta_{|n-m|,2i+1} \tag{2.52}$$

and

$$\left\langle \varphi_n \middle| \hat{p}_z^2 \middle| \varphi_m \right\rangle = \frac{n^2\pi^2}{d^2} \delta_{n,m}, \tag{2.53}$$

while k_x and k_y remain good quantum numbers, i.e., the wave functions in x and y direction are plane waves. Often the off-diagonal contributions ($n \neq m$) in Eq. (2.51) are neglected. In this case the mode n is a good quantum number and $\varphi_n(z)$ is the exact eigenfunction in the z direction. However, this approximation is only justifiable if $\gamma_3 \ll \gamma_1$ [56], which is clearly not the case for GaAs and InAs; see Table 2.2. A detailed discussion of the band structure and the density of states (DOS) of GaAs and InAs QWs extended to the two lowest subbands will be given in Chap. 7.

[6] For the definition of b_{41}^{8v8v} and r_{41}^{8v8v} in terms of the energies $\tilde{E}_0^{(\prime)}$, $\tilde{\Delta}_0^{(\prime)}$ and matrix elements $P_{\alpha\alpha'}$ and $\Sigma_{\alpha\alpha'}$, see Chap. 6 of Ref. [56]. Roughly speaking, a larger fundamental gap $\tilde{E}_0$ leads to a weaker SOC b_{41}^{8v8v} and r_{41}^{8v8v}.

Chapter 3.

3 The dielectric function in Random Phase Approximation

In the preceding chapter we introduced the single-particle Hamiltonians of three different materials: graphene, ML-MDS, and III-V semiconductors. So far, only the Coulomb interaction between electrons and atomic cores has been considered, while the repulsive interaction among the electrons (or holes) is neglected. However, in many situations such as for the description of collective density excitations, which is one of the main topics in this thesis, the inclusion of electron-electron interactions is a subtle point, and the independent-particle picture needs to be extended to incorporate interaction effects. As this generally leads to an unsolvable many-body problem, we need to restrict ourselves to appropriate approximations. The most prominent is the RPA due to its mathematical simplicity, but at the same time capability to describe basic many-body effects in a solid-state system.

Starting with a brief summary of linear response theory in Sec. 3.1, we derive the general expression for the Kubo formula. Within linear response the external perturbation is assumed to be sufficiently weak such that the equilibrium single-particle properties are not modified and the system's reaction is determined only by the equilibrium states. As a particular application of Kubo's formula, we show how the influence of an electromagnetic potential on the particle density can be described by means of the charge and current susceptibilities. It is furthermore demonstrated that the connection between the charge and current responses in the linearized Dirac model requires special care due to the infinite number of valence band states.

The DF, as one of the central quantities to describe solids, is introduced in Sec. 3.2. Using the RPA to incorporate electron-electron interactions it is shown how the existence of collective charge excitations follows from the RPA-improved DF. We briefly comment on how to measure the energy loss function (ELF) as the dissipative part of the inverse of the DF in a high-resolution electron-energy-loss spectroscope (HREELS).

3.1. Theory of linear response

We consider an equilibrium system described by the Hamiltonian $\hat{H}_{eq}$ and ask for the expectation value of an arbitrary observable $\hat{A}$,

$$\left\langle \hat{A}(t) \right\rangle = \sum_{\alpha} P_{\alpha} \left\langle \psi_{\alpha}(t) | \hat{A} | \psi_{\alpha}(t) \right\rangle , \tag{3.1}$$

under the influence of a probe potential of the form

$$\hat{V}_{pr}(t) = \hat{B}\, F(t) \theta \left[t - t_0 \right] , \tag{3.2}$$

with $\hat{B}$ being an observable, $F(t)$ a scalar function of time, and $\theta\,[t]$ the Heaviside step function. As we assume the perturbation to be sufficiently weak, we make the subtle assumption that the probabilities P_{α} of being in the (equilibrium) state ψ_{α}, where α contains the quantum numbers of the problem, are not affected by the potential [91, 92]. Keeping only terms that are constant or linear in $V_{pr}(t)$, the time evolution of the states reads [91]:

$$|\psi_{\alpha}(t)\rangle \approx e^{-i\hat{H}_{eq}t} \left[\hat{1} - i \int_{-\infty}^{t} dt'\, V_{pr}(t') \right] |\psi_{\alpha}\rangle \, . \tag{3.3}$$

This leads to a rather compact expression for the expectation value in Eq. (3.1):

$$\left\langle \delta\hat{A}(t) \right\rangle \equiv \left\langle \hat{A}(t) \right\rangle - \left\langle \hat{A}(t_0) \right\rangle = -i \int_{t_0}^{t} dt' F(t') \left\langle \left[\hat{A}(t), \hat{B}(t') \right] \right\rangle_{eq} . \tag{3.4}$$

The time argument indicates that $\hat{A}(t)$ and $\hat{B}(t)$ are given in the Heisenberg picture. [. , .] denotes the commutator. As the subscript eq indicates, the great benefit of Eq. (3.4) is that the system's response to the perturbation is calculated with respect to the equilibrium model $\hat{H}_{eq}$ [91, 92]. After Fourier expanding

$$F(t) = \int_{-\infty}^{\infty} \frac{d\omega}{2\pi} F(\omega) e^{-i\omega t + 0t}, \tag{3.5}$$

Eq. (3.4) can further be cast in the form (see Refs. [91, 92] for further details)

$$\left\langle \delta\hat{A}(t) \right\rangle = \int_{-\infty}^{\infty} \frac{d\omega}{2\pi} \chi_{AB}(\omega) F(\omega) e^{-i\omega t}. \tag{3.6}$$

Here, we introduced the complex-valued generalized susceptibility

$$\begin{aligned} \chi_{AB}(\omega) &= -i \int_{0}^{\infty} dt' \left\langle \left[\hat{A}(t'), \hat{B} \right] \right\rangle_{eq} e^{i\omega t' - 0t'} \\ &= \sum_{\alpha,\alpha'} \frac{P_{\alpha} - P_{\alpha'}}{\omega - E_{\alpha'} + E_{\alpha} + i0} \left\langle \psi_{\alpha} | \hat{A} | \psi_{\alpha'} \right\rangle \left\langle \psi_{\alpha'} | \hat{B} | \psi_{\alpha} \right\rangle \end{aligned}$$

$$
\begin{aligned}
&= \mathcal{P} \sum_{\alpha,\alpha'} \frac{P_\alpha - P_{\alpha'}}{\omega - E_{\alpha'} + E_\alpha} \left\langle \psi_\alpha | \hat{A} | \psi_{\alpha'} \right\rangle \left\langle \psi_{\alpha'} | \hat{B} | \psi_\alpha \right\rangle \\
&\quad - i\pi \sum_{\alpha,\alpha'} \left[P_\alpha - P_{\alpha'} \right] \left\langle \psi_\alpha | \hat{A} | \psi_{\alpha'} \right\rangle \left\langle \psi_{\alpha'} | \hat{B} | \psi_\alpha \right\rangle \delta[\omega - E_{\alpha'} + E_\alpha] \\
&\equiv \mathrm{Re}\left\{ \chi_{AB}(\omega) \right\} + i\, \mathrm{Im}\left\{ \chi_{AB}(\omega) \right\}. \qquad (3.7)
\end{aligned}
$$

In the last step we have made use of the Dirac identity,

$$
\frac{1}{x \pm i0} = \mathcal{P}\frac{1}{x} \mp i\pi\delta[x], \qquad (3.8)
$$

to explicitly separate the real and imaginary part.[1] $\mathcal{P}$ denotes the Cauchy principal value and $\delta[x]$ the Dirac delta function. The real and imaginary parts are not independent of each other as one can be obtained from the other with the help of the Kramers-Kronig relations

$$
\mathrm{Re}\left\{ \chi_{AB}(\omega) \right\} = \frac{1}{\pi} \mathcal{P} \int_{-\infty}^{\infty} d\omega' \frac{\mathrm{Im}\left\{ \chi_{AB}(\omega') \right\}}{\omega' - \omega} \qquad (3.9)
$$

and

$$
\mathrm{Im}\left\{ \chi_{AB}(\omega) \right\} = -\frac{1}{\pi} \mathcal{P} \int_{-\infty}^{\infty} d\omega' \frac{\mathrm{Re}\left\{ \chi_{AB}(\omega') \right\}}{\omega' - \omega}. \qquad (3.10)
$$

Due to the delta function in Eq. (3.7), it is often easier to first solve for $\mathrm{Im}\left\{ \chi_{AB}(\omega) \right\}$ and in a subsequent step apply Eq. (3.9) to get the real part. In case an analytical solution of Eq. (3.7) is not possible, $\chi_{AB}(\omega)$ can be solved numerically by approximating the Dirac delta by a Gaussian function with a sufficiently small width ϵ:

$$
\delta_\epsilon[x] = \frac{1}{\sqrt{2\pi\epsilon}} e^{-\frac{x^2}{2\epsilon}}. \qquad (3.11)
$$

The remaining integration (e.g., over all possible momenta) can then be done easily by adding to all elements in an array the weighted contribution

$$
-\pi\delta_\epsilon[\omega_i - E_{\alpha'} + E_\alpha] \left[P_\alpha - P_{\alpha'} \right] \left\langle \psi_\alpha | \hat{A} | \psi_{\alpha'} \right\rangle \left\langle \psi_{\alpha'} | \hat{B} | \psi_\alpha \right\rangle. \qquad (3.12)
$$

From the imaginary part at given lattice points ω_i, the real part can now be deduced at $\tilde{\omega}_i = (\omega_{i+1} + \omega_i)/2$ by explicitly carrying out the principal value integration in Eq. (3.9) [93]:

$$
\mathrm{Re}\left\{ \chi_{AB}(\tilde{\omega}_i) \right\} = \frac{1}{2\pi} \sum_j \left[\mathrm{Im}\left\{ \chi_{AB}(\omega_{j+1}) \right\} + \mathrm{Im}\left\{ \chi_{AB}(\omega_j) \right\} \right] \ln \frac{\omega_{j+1}^2 - \tilde{\omega}_i^2}{\omega_j^2 - \tilde{\omega}_i^2}, \qquad (3.13)
$$

[1] Here and in the following we assume the matrix elements $\left\langle \psi_\alpha | \hat{A} | \psi_{\alpha'} \right\rangle \left\langle \psi_{\alpha'} | \hat{B} | \psi_\alpha \right\rangle$ to be real. Therefore, the contribution proportional to the delta function in Eq. (3.7) equals the imaginary part of χ_{AB} and the principal value expression the real part.

where the sum runs over all lattice points. Notice that because of the general relation for hermitian operators $\hat{A}$ and $\hat{B}$ [91],

$$\chi_{AB}(-\omega) = [\chi_{AB}(\omega)]^* , \tag{3.14}$$

it is sufficient to restrict the discussion in the subsequent chapters to positive frequencies.

In the following we will focus on the changes in the charge and current operators caused by an external scalar and vector potential, respectively. In the former case the perturbation is of the form [91]

$$\hat{V}_{pr}(t) = \frac{e}{\mathcal{V}} \int d^2r \, \Phi_{ext}(\boldsymbol{r}, t)\hat{\rho}(\boldsymbol{r}), \tag{3.15}$$

with $\mathcal{V}$ being the system's volume, e the elementary charge, and $\hat{\rho}$ the density operator. According to Eq. (3.6) the induced density of a homogeneous system

$$\langle \delta\hat{\rho}(\boldsymbol{r}, t)\rangle = e \int_{-\infty}^{\infty} \frac{d\omega}{2\pi} \int \frac{d^2q}{(2\pi)^2} \, \Phi_{ext}(\boldsymbol{q}, \omega)\chi_{\rho\rho}(\boldsymbol{q}, \omega)e^{i(\boldsymbol{q}\cdot\boldsymbol{r}-\omega t)} \tag{3.16}$$

is determined by the polarizability

$$\chi_{\rho\rho}(\boldsymbol{q}, \omega) = -\frac{i}{\mathcal{V}} \int_0^{\infty} dt' \, \langle [\hat{\rho}(\boldsymbol{q}, t'), \hat{\rho}(-\boldsymbol{q})]\rangle_{eq} \, e^{i\omega t' - 0t'}. \tag{3.17}$$

$\Phi_{ext}(\boldsymbol{q}, \omega)$ and $\hat{\rho}(\boldsymbol{q}, t)$ are the Fourier transforms of the respective quantities $\Phi_{ext}(\boldsymbol{r}, t)$ and $\hat{\rho}(\boldsymbol{r}, t)$. An example of Φ_{ext} could be the Coulomb potential of a static impurity: $\Phi_{ext}(\boldsymbol{r}) = Q/4\pi\epsilon_0\epsilon_r r$. Here, Q is the charge of the impurity, ϵ_0 the vacuum permittivity, and ϵ_r the background dielectric constant. In an analogous manner, the potential

$$\hat{V}_{pr}(t) = \frac{e}{\mathcal{V}} \int d^2r \boldsymbol{A}_{ext}(\boldsymbol{r}, t) \cdot \hat{\boldsymbol{j}}_p(\boldsymbol{r}) \tag{3.18}$$

leads to the induced current

$$\left\langle \delta\hat{\boldsymbol{j}}_{p,\mu}(\boldsymbol{r}, t)\right\rangle = e \sum_{\nu=x,y} \int_{-\infty}^{\infty} \frac{d\omega}{2\pi} \int \frac{d^2q}{(2\pi)^2} \, \boldsymbol{A}_{ext,\nu}(\boldsymbol{q}, \omega) \cdot \chi_{\boldsymbol{j}_{p,\mu}\boldsymbol{j}_{p,\nu}}(\boldsymbol{q}, \omega)e^{i(\boldsymbol{q}\cdot\boldsymbol{r}-\omega t)}, \tag{3.19}$$

with $\mu, \nu = x, y$ and

$$\chi_{\boldsymbol{j}_{p,\mu}\boldsymbol{j}_{p,\nu}}(\boldsymbol{q}, \omega) = -\frac{i}{\mathcal{V}} \int_0^{\infty} dt' \left\langle \left[\hat{\boldsymbol{j}}_{p,\mu}(\boldsymbol{q}, t'), \hat{\boldsymbol{j}}_{p,\nu}(-\boldsymbol{q})\right]\right\rangle_{eq} e^{i\omega t' - 0t'}. \tag{3.20}$$

Notice that the current operator in Eqs. (3.18)-(3.20) contains only the paramagnetic contribution. The diamagnetic part needs to be added to get the total current-current susceptibility. If the momentum-dependent part of the equilibrium Hamiltonian only contains linear terms, as is the case for the KMM of Eq. (2.21), the paramagnetic current coincides with the full current defined by the variation of the Hamiltonian with respect to

the vector potential [91],

$$\hat{\boldsymbol{j}} = \frac{\delta \hat{H}_{eq}[\hat{\boldsymbol{p}} + e\boldsymbol{A}_{ext}]}{e\,\delta \boldsymbol{A}_{ext}}, \tag{3.21}$$

otherwise an additional diamagnetic contribution appears.

In translationally invariant systems the current-current susceptibility $\chi_{\boldsymbol{j}_{p,\mu}\boldsymbol{j}_{p,\nu}}$ can be split up into a longitudinal and a transversal part [91],

$$\chi_{\boldsymbol{j}_{p,\mu}\boldsymbol{j}_{p,\nu}}(\boldsymbol{q},\omega) = \frac{\boldsymbol{q}_\mu \boldsymbol{q}_\nu}{q^2}\chi^L_{j_p j_p}(q,\omega) + \left(\delta_{\mu\nu} - \frac{\boldsymbol{q}_\mu \boldsymbol{q}_\nu}{q^2}\right)\chi^T_{j_p j_p}(q,\omega)\ , \tag{3.22}$$

where both contributions only depend on the absolute value of momentum $q = |\boldsymbol{q}|$. Because of gauge invariance, the charge response due to a scalar potential $\Phi_{ext}(\boldsymbol{q},\omega)$ is the same as for a suitably chosen longitudinal vector field

$$\boldsymbol{A}_{ext}(\boldsymbol{q},\omega) = \boldsymbol{q}\frac{\Phi_{ext}(\boldsymbol{q},\omega)}{e\omega}, \tag{3.23}$$

and therefore the polarizability should be connected to the current-current susceptibility somehow. While in an electron gas this leads to the rather simple relation [91]

$$\omega^2 \chi_{\rho\rho}(q,\omega) = q^2 \chi^L_{j_p j_p}(q,\omega) + q^2 \chi^D_{jj}, \tag{3.24}$$

with $\chi^D_{jj} = n/m_0$ being the diamagnetic part and n the carrier density, in the linearized Dirac model this relation does not hold and special care needs to be taken due to the infinite number of valence band states, which requires a cutoff in practical calculations. From the general relation [91]

$$\chi_{AB}(\omega) = \frac{1}{\omega}\left\{\left\langle\left[\hat{A},\hat{B}\right]\right\rangle_{eq} + \chi_{[A,H],B}(\omega)\right\} \tag{3.25}$$

and the commutator [94]

$$\left[\hat{\rho}(\boldsymbol{q}), \hat{H}_g\right] = v_F \boldsymbol{q}\cdot\boldsymbol{\sigma} = \boldsymbol{q}\cdot\boldsymbol{j}(\boldsymbol{q}) \tag{3.26}$$

in graphene,[2] we obtain

$$\begin{aligned}\chi_{\rho\rho}(\boldsymbol{q},\omega) &= \frac{1}{\mathcal{V}\omega}\left\langle[\hat{\rho}(\boldsymbol{q}),\hat{\rho}(-\boldsymbol{q})]\right\rangle_{eq} + \frac{1}{\omega}\sum_{\mu=x,y} q_\mu \chi_{\boldsymbol{j}_\mu\rho}(\boldsymbol{q},\omega) \\ &= \frac{1}{\mathcal{V}\omega}\left\langle[\hat{\rho}(\boldsymbol{q}),\hat{\rho}(-\boldsymbol{q})]\right\rangle_{eq} + \frac{1}{\mathcal{V}\omega^2}\left\langle[\boldsymbol{q}\cdot\boldsymbol{j}(\boldsymbol{q}),\hat{\rho}(-\boldsymbol{q})]\right\rangle_{eq} + \frac{1}{\omega^2}\sum_{\mu,\nu=x,y} q_\mu \chi_{\boldsymbol{j}_\mu\boldsymbol{j}_\nu}(\boldsymbol{q},\omega) q_\nu.\end{aligned} \tag{3.27}$$

[2] As $\hat{\boldsymbol{j}} = \hat{\boldsymbol{j}}_p$ in the linearized Dirac model of graphene, the index p is dropped for the rest of this thesis.

While the first term on the right-hand side vanishes [95], the second contribution, the so-called anomalous commutator, needs special attention. Its value (per spin and valley)

$$\frac{1}{\mathcal{V}} \langle [\boldsymbol{q} \cdot \boldsymbol{j}(\boldsymbol{q}), \hat{\rho}(-\boldsymbol{q})] \rangle_{eq} = \frac{q^2 D}{8\pi}, \tag{3.28}$$

where D is an energy cutoff, has been calculated in Ref. [94] for graphene including a sublattice-dependent constant mass term. For a translationally invariant system, i.e.,

$$\sum_{\mu,\nu=x,y} \boldsymbol{q}_\mu \chi_{\boldsymbol{j}_\mu \boldsymbol{j}_\nu}(\boldsymbol{q}, \omega) \boldsymbol{q}_\nu = q^2 \chi^L_{jj}, \tag{3.29}$$

we finally arrive at

$$\omega^2 \, \chi_{\rho\rho}(q, \omega) = q^2 \chi^L_{jj}(q, \omega) + \frac{1}{\mathcal{V}} \langle [\boldsymbol{q} \cdot \boldsymbol{j}(\boldsymbol{q}), \hat{\rho}(-\boldsymbol{q})] \rangle_{eq} \,, \tag{3.30}$$

where gauge invariance is explicitly broken. This can be seen by taking the static long-wavelength limit (see Sec. 5.3)

$$\lim_{q \to 0} \chi^L_{jj}(q, 0) = -\frac{D}{2\pi} \neq 0, \tag{3.31}$$

which is unphysical, as a longitudinal static vector potential cannot induce a current. As stated in Ref. [96], taking into account the full BZ leads to the cancellation of the commutator by a diamagnetic contribution of the form

$$\sum_{\mu,\nu=x,y} \boldsymbol{q}_\mu \chi^D_{\mu\nu} \boldsymbol{q}_\nu = -\frac{1}{\mathcal{V}} \langle [\boldsymbol{q} \cdot \boldsymbol{j}(\boldsymbol{q}), \hat{\rho}(-\boldsymbol{q})] \rangle_{eq} \,, \tag{3.32}$$

which is absent in the linearized model, such that the continuity equation is fulfilled again.

3.2. Dielectric function

Among the various transport quantities in solid state physics, the DF plays a central role. Not only does it provide information on optical experiments and transport characteristics, but also on fundamental excitations of the material, screening properties, and hence electron-phonon interactions.

The definition of the DF relates the density changes in a solid to the external density ρ_{ext} via

$$\delta\rho = \left[\frac{1}{\varepsilon} - 1 \right] \rho_{ext}. \tag{3.33}$$

As described in Refs. [91, 92], the DF is connected to the quantum mechanical Kubo product for the polarizability by

$$\varepsilon(\boldsymbol{q},\omega) = \frac{1}{1+V(q)\chi_{\rho\rho}(\boldsymbol{q},\omega)}. \tag{3.34}$$

Here, $V(q)$ is the Fourier transform of the Coulomb potential in two dimensions,

$$V(r) = \frac{e^2}{4\pi\epsilon_0\epsilon_r r}. \tag{3.35}$$

In truly 2D systems such as graphene or ML-MDS this leads to the rather simple form

$$V(q) = \frac{e^2}{2\epsilon_0\epsilon_r q}. \tag{3.36}$$

However, if the density profile in z direction deviates from a delta function, the analytical form of $V(q)$ is more complicated [91]. An example for this is discussed in Chap. 7 in the context of GaAs and InAs QWs.

Now that we know how to derive the DF from the Kubo polarizability, we need to specify what exactly is meant by equilibrium. In many situations the independent-particle picture is insufficient and interactions between electrons need to be included. In this case the expectation values in the Kubo formula require the usually unknown interacting ground state and therefore one needs to resort to reasonable approximations. The most prominent is the RPA,[3] where, using the language of Feynman diagrams, out of the infinite number of possible diagrams, only the most divergent are taken into account. From a rough estimate based on a power analysis of the denominators, it turns out that these are the contributions of the noninteracting system (denoted as $\chi^0_{\rho\rho}$) connected by the Coulomb propagator $V(q)$. For the RPA-improved polarizability this leads to a geometric series [91]

$$\chi^{RPA}_{\rho\rho}(\boldsymbol{q},\omega) = \chi^0_{\rho\rho}(\boldsymbol{q},\omega)\left[1+V(q)\chi^{RPA}_{\rho\rho}(\boldsymbol{q},\omega)\right], \tag{3.37}$$

which can easily be rewritten as

$$\chi^{RPA}_{\rho\rho}(\boldsymbol{q},\omega) = \frac{\chi^0_{\rho\rho}(\boldsymbol{q},\omega)}{1-V(q)\chi^0_{\rho\rho}(\boldsymbol{q},\omega)}. \tag{3.38}$$

The RPA DF in Eq. (3.34) then takes a rather simple form:

$$\varepsilon^{RPA}(\boldsymbol{q},\omega) = 1 - V(q)\chi^0_{\rho\rho}(\boldsymbol{q},\omega). \tag{3.39}$$

The great benefit of the RPA is twofold: First of all, in order to include interaction effects, one only needs to calculate the free polarizability which is, in our case, essentially a 2D integral in momentum space. Second, despite its mathematical simplicity, the RPA is a nonperturbative result in the sense that an infinite number of contributions are taken into account. In the subsequent chapters we will restrict ourselves to RPA, therefore the

[3] For a detailed derivation and discussion of the RPA we refer to Refs. [91, 92].

superscript will no longer be written and the notation $\varepsilon(\boldsymbol{q},\omega)$ has to be understood as $\varepsilon^{RPA}(\boldsymbol{q},\omega)$.

Referring to the definition of the DF in Eq. (3.33), we can see that zeros of the DF or, equivalently, poles in the RPA polarizability correspond to collective charge excitations known as plasmons, as even in the absence of an external field a finite potential is present in the system. In order to find the plasmon energies ω_q and damping rates γ_q at a given momentum transfer $\boldsymbol{q}$, we need to solve the complex-valued equation

$$\varepsilon(\boldsymbol{q},\omega_q - i\gamma_q) = 0. \tag{3.40}$$

For small damping rates,

$$\gamma_q \ll \omega_q, \tag{3.41}$$

Eq. (3.40) can further be simplified by

$$\operatorname{Re}\{\varepsilon(\boldsymbol{q},\omega_q)\} = 0 \tag{3.42}$$

and

$$\gamma_q = \left[\frac{\partial}{\partial\omega}\operatorname{Re}\{\varepsilon(\boldsymbol{q},\omega)\}\Big|_{\omega=\omega_q}\right]^{-1} \operatorname{Im}\{\varepsilon(\boldsymbol{q},\omega_q)\}. \tag{3.43}$$

However, if the plasmon energy is obtained from Eq. (3.42) it needs to be verified that the so-found solution also corresponds to a resonance in the ELF, a quantity which is available in scattering experiments. From the definition of the ELF,

$$-\operatorname{Im}\left\{\frac{1}{\varepsilon(\boldsymbol{q},\omega)}\right\} = \frac{\operatorname{Im}\{\varepsilon(\boldsymbol{q},\omega)\}}{[\operatorname{Re}\{\varepsilon(\boldsymbol{q},\omega)\}]^2 + [\operatorname{Im}\{\varepsilon(\boldsymbol{q},\omega)\}]^2}, \tag{3.44}$$

we notice that if both the real and imaginary part vanishes at a given energy (the plasmon energy), the ELF exhibits a delta peak:

$$-\operatorname{Im}\left\{\frac{1}{\varepsilon(\boldsymbol{q},\omega)}\right\} \overset{\omega\approx\omega_q}{=} \left[\frac{\partial}{\partial\omega}\operatorname{Re}\{\varepsilon(\boldsymbol{q},\omega)\}\Big|_{\omega=\omega_q}\right]^{-1} \delta[\omega-\omega_q]. \tag{3.45}$$

The prefactor is also denoted as the plasmon oscillator strength [91]. On the other hand, if the imaginary part is finite but small, the peak in the ELF will be broadened and the lifetime of the plasmon, being inversely proportional to the width of the peak, becomes finite. Notice that for the numerical evaluation of the ELF it is necessary to add an infinitesimal small contribution to the imaginary part of the DF in order to see a resonant peak and therefore we plot the function

$$-\operatorname{Im}\left\{\frac{1}{\varepsilon(\boldsymbol{q},\omega+i0)}\right\}. \tag{3.46}$$

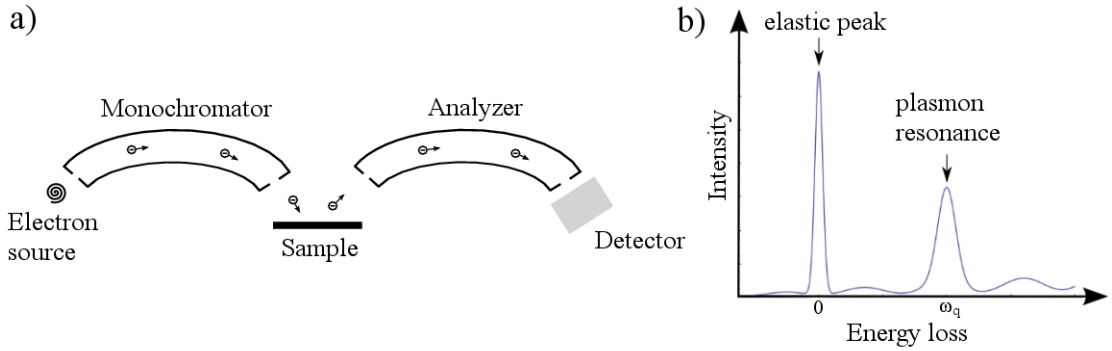

Figure 3.1.: (a) Sketch of a HREELS experiment. (b) Idealized intensity profile.

In the long-wavelength limit, $v_F q \ll \omega$, the free polarizability of an isotropic 2D system can be approximated via [97]

$$\chi^0_{\rho\rho}(q,\omega) \approx \frac{gq^2}{4\pi\omega^2} \sum_\nu k_{F\nu} \left| \frac{\partial E_\nu(k)}{\partial k} \right|_{k=k_{F\nu}}, \tag{3.47}$$

where g is a degeneracy factor of the problem (due to orbital and spin degeneracies), $k_{F\nu}$ the Fermi wave vector in band E_ν and the sum runs over all bands that contain the Fermi energy. According to Eq. (3.42) for the plasmon dispersion this immediately leads to

$$\omega^0_q \approx \sqrt{\frac{e^2}{8\pi\epsilon_0\epsilon_r} \sum_\nu k_{F\nu} \left| \frac{\partial E_\nu(k)}{\partial k} \right|_{k=k_{F\nu}}} \sqrt{q}, \tag{3.48}$$

with the universal $\sqrt{q}$-dependence of plasmons in 2D systems. As we will see in the following chapters, this relation is accurate for small wave vectors but fails to properly describe the energies close to the EHC.

Another type of excitations featured by the DF in RPA is the creation of real electron-hole pairs. If the imaginary part of the DF is nonzero, the absorption of energy leads to a finite quasiparticle lifetime. This dissipation mechanism is commonly known as Landau damping. However, due to conservation of energy Landau damping is possible only for specific combinations of momentum and frequency. The corresponding region in the q-ω plane where $\mathrm{Im}\{\varepsilon(\boldsymbol{q},\omega)\} \neq 0$ is fulfilled is called the electron-hole continuum. The EHC can generally be separated into an intra- and interband part. While in the former the initial and final states lie in the same band and hence transitions can only happen for finite momentum transfer, the latter also allows vertical transitions close to $q = 0$.

Let us finally comment on how to read out the excitation energies by means of HREELS [98]; see Fig. 3.1(a) for a schematic sketch. After electrons get excited in a tungsten filament, they pass through a monochromator. The monochromator decelerates the electrons and reduces the energy distribution of the particles in the beam. As the excitation energies of surfaces are usually close to each other, and in particular close to the elastic

scattering peak, a high resolution is required and small energy losses of a few meV should be detectable. Moreover, in order to make the electrons scatter on the surface rather than on the underlying substrate, their mean-free path needs to be comparable to the layer thickness. Typically, this can be achieved with particle energies of 10 eV - 20 eV. The small mean-free path, on the other hand, requires the whole setup to be in ultra-high vacuum. After the backscattered electrons pass through the analyzer, the intensity profile is finally recorded as a function of the energy loss; see Fig. 3.1(b). Besides a strong signal corresponding to the elastic process, peaks in the spectrum indicate the plasmonic excitation energies. In recent HREELS experiments on graphene [58, 59], the $\sqrt{q}$-behavior of the plasmon dispersion for small wave vectors could be confirmed experimentally, while for larger momenta the dispersion clearly deviates from Eq. (3.48) due to quantum mechanical many-body corrections, requiring the RPA treatment of the DF.

Chapter 4.

4 Dielectric function, plasmons, and screening of graphene in the presence of spin-orbit interactions

Parts of this chapter have been published in collaboration with Tobias Stauber and John Schliemann in Phys. Rev. B 86, 195424 (2012).

In this chapter we discuss the dielectric properties of graphene in the presence of SOIs of the intrinsic and Rashba type. After a short summary of the eigensystem of the KMM in Sec. 4.1, closed analytical expressions for the imaginary as well as for the real part of the DF for arbitrary frequency, wave vector, doping, and SOC parameters are presented in Sect. 4.2. Our findings generalize earlier results for graphene within the linear approximation [61, 62], including a sublattice-dependent mass term [99]. This is followed by a detailed discussion of the plasmon spectra and the ELFs for various combinations of the SOC parameters in Sec. 4.3, including the case of purely Rashba or purely intrinsic SOC, and the case of equally large Rashba and intrinsic SOIs. As we will see, the breaking of structure inversion symmetry leads to the existence of a new plasmonic mode with an energy much larger compared to the long-wavelength result. However, from the ELF one also sees that these high-energy solutions lie within the EHC where they become damped even for small momenta and hence cannot be considered as truly coherent modes. The static limit of the DF is used in Sec. 4.4 to numerically calculate the asymptotic behavior of the screened Coulomb potential of a charged impurity. The lifting of the spin-degeneracy for finite λ_R has a distinct effect on the potential as it induces a beating of Friedel oscillations in the RPA-improved Coulomb potential. We conclude this chapter in Sec. 4.5 with a summary of the main result and discuss the connection to other 2D materials.

4.1. The model

We describe graphene including SOIs of the intrinsic and Rashba type within the Dirac cone approximation using the KMM of Eq. (2.21):

$$\hat{H}_g^\tau = v_F \boldsymbol{k}\cdot\hat{\boldsymbol{\sigma}}_\tau + \tau\lambda_I\hat{\sigma}_z\hat{s}_z + \lambda_R\left(\tau\hat{\sigma}_x\hat{s}_y - \hat{\sigma}_y\hat{s}_x\right), \quad \text{with} \quad \tau = \pm 1.$$

Without loss of generality, we assume positive Rashba and intrinsic SOC constants. Since within this model the two independent K points are not coupled, i.e., intervalley processes are not allowed, we can limit the following discussion to the above Hamiltonian with $\tau = +1$, multiplying the final results by the valley index $g_v = 2$.

The eigenstates of $\hat{H}_g^+$ read

$$|\xi_{g,\pm\pm}(\boldsymbol{k})\rangle = \frac{1}{\sqrt{2}}\begin{pmatrix} \sin\left(\frac{\theta_\mp}{2}\right) \\ i\cos\left(\frac{\theta_\mp}{2}\right)e^{i\phi_k} \\ \pm\cos\left(\frac{\theta_\mp}{2}\right)e^{i\phi_k} \\ \pm i\sin\left(\frac{\theta_\mp}{2}\right)e^{2i\phi_k}\end{pmatrix} \tag{4.1}$$

and

$$|\xi_{g,\pm\mp}(\boldsymbol{k})\rangle = \frac{1}{\sqrt{2}}\begin{pmatrix} \cos\left(\frac{\theta_\mp}{2}\right) \\ -i\sin\left(\frac{\theta_\mp}{2}\right)e^{i\phi_k} \\ \mp\sin\left(\frac{\theta_\mp}{2}\right)e^{i\phi_k} \\ \pm i\cos\left(\frac{\theta_\mp}{2}\right)e^{2i\phi_k}\end{pmatrix}, \tag{4.2}$$

with

$$\sin\theta_\pm = \frac{v_F k}{\sqrt{v_F^2k^2 + \lambda_\pm^2}} \tag{4.3}$$

and hence

$$\sin\frac{\theta_\pm}{2} = \frac{1}{\sqrt{2}}\frac{\sqrt{\sqrt{v_F^2k^2+\lambda_\pm^2} - \lambda_\pm}}{\left(v_F^2k^2+\lambda_\pm^2\right)^{1/4}}. \tag{4.4}$$

The in-plane angle is $\tan\phi_k = k_y/k_x$ and

$$\lambda_\pm = \lambda_R \pm \lambda_I. \tag{4.5}$$

The isotropic energies of the KMM are known from Eq. (2.22):

$$E_{g,\alpha\beta}(k) = \alpha\lambda_R + \beta\sqrt{v_F^2k^2 + {\lambda_{-\alpha}}^2}, \quad \text{with} \quad \alpha,\beta = \pm 1.$$

In order to get the DF in RPA [see Eq. (3.39)],

$$\varepsilon(q,\omega) = 1 - \frac{e^2}{2\epsilon_0\epsilon_r q}\chi^0_{\rho\rho}(q,\omega),$$

we need to calculate the free polarizability given by the Kubo product [91]

$$\chi^0_{\rho\rho}(q,\omega) = g_v \sum_{\eta_1,\eta_2,\eta_3,\eta_4=\pm1} \int \frac{d^2k}{(2\pi)^2} \left| \left\langle \xi_{g,\eta_1\eta_2}(\boldsymbol{k}) \middle| \xi_{g,\eta_3\eta_4}(\boldsymbol{k}+\boldsymbol{q}) \right\rangle \right|^2 \times \\ \times \frac{f\left[E_{g,\eta_1\eta_2}(k)\right] - f\left[E_{g,\eta_3\eta_4}(|\boldsymbol{k}+\boldsymbol{q}|)\right]}{\omega - E_{g,\eta_3\eta_4}(|\boldsymbol{k}+\boldsymbol{q}|) + E_{g,\eta_1\eta_2}(k) + i0}, \tag{4.6}$$

which, due to the translational symmetry of the problem, does not depend on the in-plane angle $\tan\phi_q = q_y/q_x$. In the following we assume zero temperature ($T = 0$) in order to allow further analytical progress, reducing the Fermi function

$$f[E] = \left[1 + e^{\frac{E-\mu}{k_B T}}\right]^{-1} \overset{T\to 0}{=} \theta\left[\mu - E\right] \tag{4.7}$$

to a simple step function (with k_B being Boltzmann's constant).

4.2. Analytical results for the free polarizability

4.2.1. Zero doping

For zero doping[1] the valence bands are completely filled while the conduction bands are empty. Therefore, only transitions between bands E_{g,η_1-} and E_{g,η_3+} are possible and the polarizability in Eq. (4.6) can be decomposed as

$$\chi^{0,un}_{\rho\rho}(q,\omega) = \sum_{\eta_1,\eta_3=\pm1} \chi^{\eta_1- \to \eta_3+}(q,\omega). \tag{4.8}$$

Here, we introduced the notation $\chi^{\eta_1\eta_2\to\eta_3\eta_4}(q,\omega)$ describing transitions from the initial band $E_{g,\eta_1\eta_2}(k)$ to the final band $E_{g,\eta_3\eta_4}(|\boldsymbol{k}+\boldsymbol{q}|)$. For details on the calculation of the polarizability we refer to App. A, where major steps can be found. For the imaginary part we find

$$\mathrm{Im}\left\{\chi^{\mp-\to\mp+}(q,\omega)\right\} = \frac{g_v}{16 v_F^2}\theta\left[\omega^2 - v_F^2 q^2 - 4{\lambda_\pm}^2\right] \times \\ \times \left[\frac{3v_F^4 q^4 - 4v_F^2{\lambda_\pm}^2 q^2 - 5v_F^2 q^2\omega^2 + 2\omega^4}{\left(\omega^2 - v_F^2 q^2\right)^{3/2}} - \frac{\left|v_F^2 q^2 - \omega\left(\omega - 2\lambda_\pm\right)\right| + \left|v_F^2 q^2 - \omega\left(\omega + 2\lambda_\pm\right)\right|}{\omega}\right] \tag{4.9}$$

[1] Notice that zero doping does not necessarily mean $\mu = 0$ if both types of SOIs are present as the charge neutrality point is shifted away from zero.

and

$$\mathrm{Im}\left\{\chi^{\pm-\to\mp+}(q,\omega)\right\} = -\frac{g_v}{8v_F^2}\theta\left[\omega_\pm^2 - v_F^2q^2 - 4\gamma^2\right]\times$$
$$\times\left[\sqrt{\omega_\pm^2 - v_F^2q^2} - \frac{\left|v_F^2q^2 - \omega\left(\omega \pm 2\lambda_-\right)\right|}{2\omega} - \frac{\left|v_F^2q^2 - \omega\left(\omega \pm 2\lambda_+\right)\right|}{2\omega}\right]. \tag{4.10}$$

Here, we defined

$$\omega_\pm = \omega \pm 2\lambda_R \tag{4.11}$$

and

$$\gamma = \max\{\lambda_R, \lambda_I\}. \tag{4.12}$$

For equally large SOC parameters, $\lambda_R = \lambda_I$, the imaginary part is divergent at $\omega = v_Fq$, while for other combinations this singularity is smeared out. The divergent part of the polarizability in Eq. (4.9) is $\chi^{+-\to++}$ due to the linearity of the bands $E_{g,+\pm}$ in this case.

The real part can be obtained directly from the imaginary part via the Kramers-Kronig relation in Eq. (3.9). After carrying out the remaining integration in frequency space, where it is necessary to keep the principal value in the integral, we arrive at

$$\mathrm{Re}\left\{\chi^{\mp-\to\mp+}(q,\omega)\right\} = \frac{g_v}{8\pi v_F^2}\left[-2\lambda_\pm - \frac{2v_F^2\lambda_\pm q^2}{v_F^2q^2-\omega^2} + 2\lambda_\pm\ln\left|\frac{v_F^2q^2 - \omega^2 + 4\lambda_\pm^2}{\left(\sqrt{v_F^2q^2+\lambda_\pm^2}+\lambda_\pm\right)^2 - \omega^2}\right|\right.$$
$$+2\sqrt{v_F^2q^2+\lambda_\pm^2} + \left(5v_F^2q^2\omega^2 + 4v_F^2\lambda_\pm^2q^2 - 3v_F^4q^4 - 2w^4\right)\mathrm{Re}\left\{\frac{\arctan\left(\frac{\sqrt{v_F^2q^2-\omega^2}}{2\lambda_\pm}\right)}{\left(v_F^2q^2-\omega^2\right)^{3/2}}\right\}$$
$$\left.-\frac{\omega^2 - v_F^2q^2}{2\omega}\ln\frac{\sqrt{v_F^2q^2+\lambda_\pm^2}+\lambda_\pm+\omega}{\sqrt{v_F^2q^2+\lambda_\pm^2}+\lambda_\pm-\omega}\right] \tag{4.13}$$

and

$$\mathrm{Re}\left\{\chi^{\pm-\to\mp+}(q,\omega)\right\} = -\frac{g_v}{4\pi v_F^2}\left[2\left(\pm\lambda_R - \gamma \pm \lambda_R\ln 4\right) \mp 2\lambda_R\,\mathrm{arcsinh}\left(\frac{2\gamma}{v_Fq}\right)\right.$$
$$-\frac{1}{2}\mathrm{Re}\left\{\sqrt{v_F^2q^2-\omega_\pm^2}\arcsin\frac{\sqrt{v_F^2q^2-\omega_\pm^2}\left(\omega_\pm\sqrt{v_F^2q^2+4\gamma^2}+v_F^2q^2\right)+\gamma\omega_\pm\sqrt{v_F^2q^2-\omega_\pm^2}}{v_F^2q^2\left[\sqrt{v_Fq^2+4\gamma^2}+\omega_\pm\right]}\right\}$$
$$-\frac{1}{2}\mathrm{Re}\left\{\sqrt{v_F^2q^2-\omega_\mp^2}\arcsin\frac{\sqrt{v_F^2q^2-\omega_\mp^2}\left(\omega_\mp\sqrt{v_F^2q^2+4\gamma^2}-v_F^2q^2\right)+\gamma\omega_\mp\sqrt{v_F^2q^2-\omega_\mp^2}}{v_F^2q^2\left[\sqrt{v_Fq^2+4\gamma^2}+\omega_\mp\right]}\right\}$$
$$\left.+\theta\left[\pm\lambda_\pm\right]\mathcal{L}_{(\pm\lambda_\mp)}\left(\sqrt{v_F^2q^2+\lambda_\mp^2}\mp\lambda_\mp\right) - \frac{1}{2}\,\mathrm{sign}\left(\pm\lambda_\pm\right)\mathcal{L}_{(\pm\lambda_\mp)}\left(\sqrt{v_F^2q^2+4\gamma^2}\mp 2\lambda_R\right)\right.$$

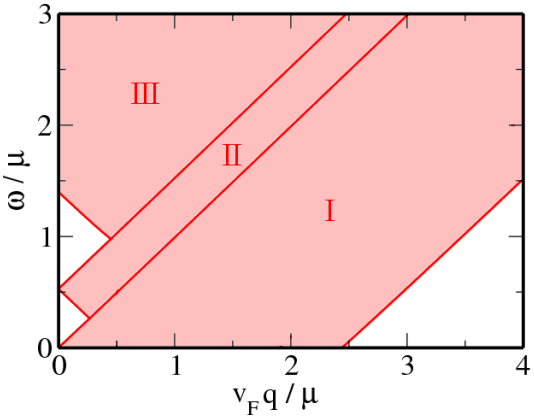

Figure 4.1.: EHC (dark area) for the particular choice of $\lambda_R = 2\lambda_I = 0.3\mu$. Analytical expressions for the boundaries of the distinct regions I, II, and III can be found in Sec. 4.2.2.

$$+\theta\left[\pm\lambda_{\mp}\right]\mathcal{L}_{(\pm\lambda_{\pm})}\left(\sqrt{v_F^2q^2+\lambda_{\pm}^2}\mp\lambda_{\pm}\right)-\frac{1}{2}\,\mathrm{sign}\left(\pm\lambda_{\mp}\right)\mathcal{L}_{(\pm\lambda_{\pm})}\left(\sqrt{v_F^2q^2+4\gamma^2}\mp 2\lambda_R\right)\Bigg]. \tag{4.14}$$

Here, we defined the function

$$\mathcal{L}_{\lambda_{\pm}}(x)=x+\lambda_{\pm}\ln\frac{x^2-\omega^2}{v_F^2q^2}-\frac{\omega^2-v_F^2q^2}{2\omega}\ln\left|\frac{x+\omega}{x-\omega}\right|. \tag{4.15}$$

4.2.2. Finite doping

We now continue with the case of a finite Fermi energy lying in the conduction band (the p-doped case is analogous). The free polarizability in the doped case can be expressed as

$$\chi^{0,do}_{\rho\rho}(q,\omega)=\chi^{0,un}_{\rho\rho}(q,\omega)+\delta\chi_{k_{F+}}(q,\omega)+\delta\chi_{k_{F-}}(q,\omega). \tag{4.16}$$

Besides the undoped part $\chi^{0,un}_{\rho\rho}$ given above, we have to add the two contributions

$$\delta\chi_{k_{F\pm}}(q,\omega)=\frac{g_v}{(2\pi)^2}\sum_{\alpha,\eta_3,\eta_4=\pm1}\int_0^{k_{F\pm}}dkk\int_0^{2\pi}d\phi_k\,\frac{\alpha\left|\left\langle\xi_{g,\pm+}(\boldsymbol{k})\middle|\xi_{g,\eta_3\eta_4}(\boldsymbol{k}+\boldsymbol{q})\right\rangle\right|^2}{\omega-\alpha\left[E_{g,\eta_3\eta_4}\left(|\boldsymbol{k}+\boldsymbol{q}|\right)-E_{g,\pm+}(k)\right]+i0}, \tag{4.17}$$

referring to transitions with initial states in band $E_{g,++}$ (upper sign) and $E_{g,-+}$ (lower sign), respectively. For the definition of the Fermi wave vector in graphene, $k_{F\pm}$, see Eq. (2.23). As the expressions for the doped real and imaginary part of the free polarizability are quite lengthy, we refer to App. A, where the results including major steps of the derivation can be found.

Similar to the undoped case, the polarizability of graphene is finite at $\omega = v_Fq$ for $\lambda_R \neq \lambda_I$ and divergent otherwise. However, in any case this divergence vanishes in the RPA-improved polarizability [61]. From the band dispersion as given in Eq. (2.22), we can determine the boundaries of the dissipative EHC [91]. In Fig. 4.1 the EHC is shown

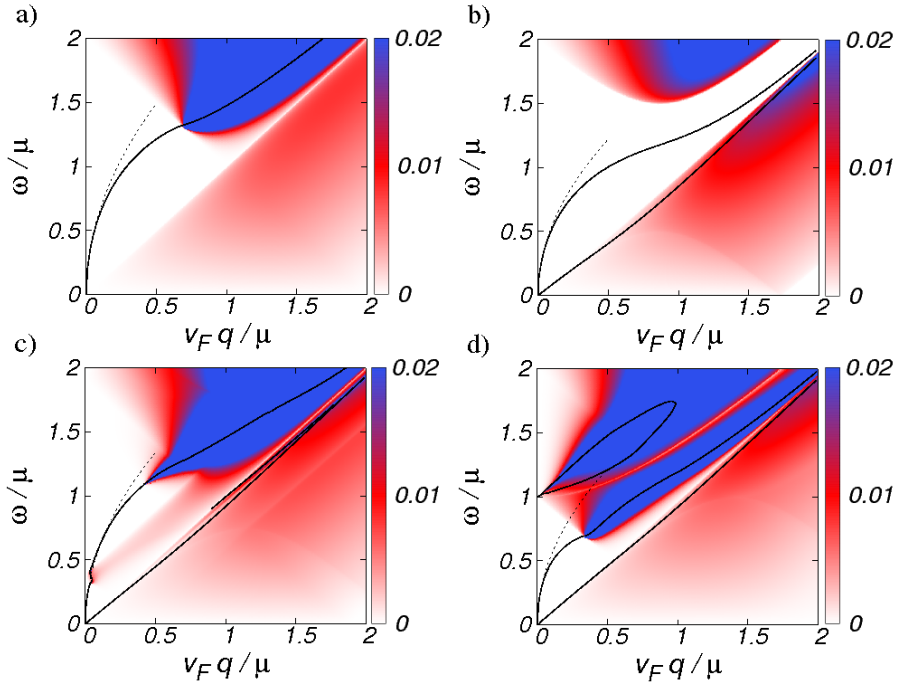

Figure 4.2.: Density plot of the ELF (normalized to $V(q)\mu/v_F^2$) for various combinations of the SOC parameters: (a) $(\lambda_R/\mu, \lambda_I/\mu) = (0,0)$, (b) $(0, 0.5)$, (c) $(0.25, 0.25)$, (d) $(0.5, 0)$. Solid lines correspond to the numerical solutions of Eq. (3.42), while dashed lines represent the long-wavelength result of Eq. (4.22).

for the particular choice of $\lambda_R = 2\lambda_I = 0.3\mu$. The lower and upper boundaries of the EHC region I are given by

$$\omega_{low}^{I} = \max\left\{0,\ \sqrt{v_F^2\left(k_{F-}-q\right)^2+\lambda_+^2} - \sqrt{v_F^2 k_{F-}^2+\lambda_+^2}\right\} \tag{4.18}$$

and

$$\omega_{up}^{I} = \max\left\{\sqrt{v_F^2\left(k_{F-}+q\right)^2+\lambda_+^2} - \sqrt{v_F^2 k_{F-}^2+\lambda_+^2},\right.$$
$$\left.\sqrt{v_F^2\left(k_{F+}+q\right)^2+\lambda_-^2} - \sqrt{v_F^2 k_{F+}^2+\lambda_-^2}\right\}, \tag{4.19}$$

respectively. Region I is due to intraband transitions from band $E_{g,\pm+}(k)$ to $E_{g,\pm+}(|\boldsymbol{k}+\boldsymbol{q}|)$. Region II accounts for interband transitions between conduction bands and is confined by

$$\omega_{up/low}^{II} = \sqrt{v_F^2\left(k_{F-}\pm q\right)^2+\lambda_-^2} - \sqrt{v_F^2 k_{F-}^2+\lambda_+^2} + 2\lambda_R. \tag{4.20}$$

For region III the lower limit reads

$$\omega_{low}^{III} = \min\left\{\sqrt{v_F^2\left(k_{F-}-q\right)^2+\lambda_+^2}+\sqrt{v_F^2k_{F-}^2+\lambda_-^2}-2\lambda_R,\right.$$
$$\left.\sqrt{v_F^2\left(k_{F+}-q\right)^2+\lambda_-^2}+\sqrt{v_F^2k_{F+}^2+\lambda_-^2}\right\}, \tag{4.21}$$

while there is no restriction to the upper boundary. This part is due to transitions between valence and conduction bands.

4.3. Collective charge excitations

In order to investigate the plasmon spectrum, we solve the approximate equation (3.42),

$$\mathrm{Re}\left\{\varepsilon(q,\omega_q)\right\}=0,$$

to find the roots of the DF. However, only if the damping rate γ_q is sufficiently small, $\gamma_q \ll \omega_q$, one can speak of collective density fluctuations. Therefore, we will also discuss the more general ELF,

$$-\,\mathrm{Im}\left\{\frac{1}{\varepsilon(q,\omega+i0)}\right\},$$

to check if the so-found (mathematical) solution also corresponds to an internal excitation of the system.

Similar to Refs. [99, 100] there are several zeros of Eq. (3.42) for nonzero SOC parameters. In Fig. 4.2 they are shown as solid lines together with a density plot of the ELF for freestanding graphene ($\epsilon_r = 1$). One of these solutions has an almost linear dispersion with a quasiparticle velocity close to the Fermi velocity. However, as can be seen from Figs. 4.3(a) and (b), this solution (at $\omega \approx 0.1\mu$ in both figures) does not lead to a resonance in the ELF and does thus not resemble a plasmonic mode. In the case where the gap in the energy spectrum is closed due to a large Rashba coupling strength, see Fig. 4.2(d), two additional zeros appear with a finite energy even at zero wave vector, similar to previous findings in bilayer graphene [100, 101]. However, these potential modes are damped by interband transitions as can be seen from the background color of the density plot in Fig. 4.2(d). Therefore, the corresponding peak in the ELF of Fig. 4.3(b) is broadened and the plasmon's lifetime is reduced such that the high-energy solutions cannot be considered as truly coherent modes.

We are thus left with the branch which is always present (i.e., even without SOIs) and which resembles the only genuine plasmonic mode. In the long-wavelength limit its dispersion ω_q^0 can be approximated by

$$\omega_q^0 = \mathcal{B}\sqrt{q}, \tag{4.22}$$

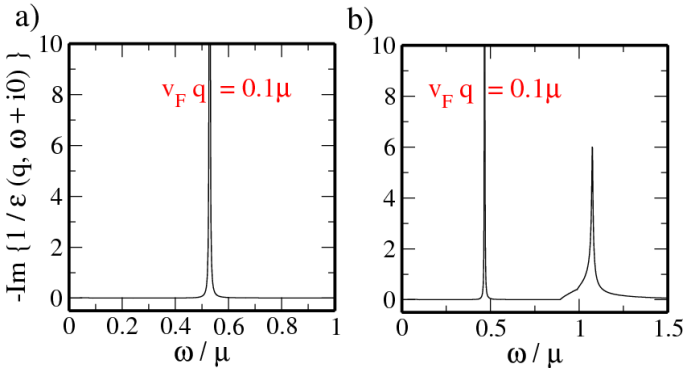

Figure 4.3.: ELF for fixed $v_F q = 0.1\mu$ with (a) $\lambda_R = 0$, $\lambda_I = 0.5\mu$ and (b) $\lambda_R = 0.5\mu$, $\lambda_I = 0$.

where the prefactor

$$\mathcal{B} = \sqrt{\frac{g_v e^2}{8\pi\epsilon_0\epsilon_r} \sum_{\nu=\pm1} \frac{v_F^2 k_{F\nu}^2}{\sqrt{v_F^2 k_{F\nu}^2 + \lambda_{-\nu}^2}}} \tag{4.23}$$

follows from Eq. (3.48). One can easily see that Eq. (4.22), shown as dashed lines in Fig. 4.2, coincides with the numerical solution ω_q for small momenta, whereas for larger momenta (and in particular close to the EHC) the exact result is redshifted compared to ω_q^0. If the intrinsic coupling is large enough, i.e., $\lambda_I \gtrsim 0.3\mu$ for freestanding graphene, ω_q remains in the region where Landau damping is absent even for large momenta [99]; see Fig. 4.2(b). Otherwise, the mode eventually enters the EHC due to interband transitions from the valence to the conduction band as can be seen in Figs. 4.2(a) and (d).

If now two conduction bands are occupied for $\lambda_R \neq 0$, which is the case in Figs. 4.2(c) and 4.4, the plasmon mode is disrupted at low momenta, $v_F q \approx 0.05\mu$, by a region with a finite imaginary part where the mode becomes damped. This additional Landau-damped region is due to interband transitions from the two conduction bands. The plasmon velocity formally diverges at the entering and exit point of this pseudo-gap. The crossing points can be approximated by looking at the intersection of this region with the analytic long-wavelength plasmon dispersion. For the special case of $\lambda_R = \lambda_I$, this leads to the critical wave vector

$$q_{cr}^{\pm} = \frac{\left[\mathcal{B} \pm \sqrt{\mathcal{B}^2 - 4v_F\left(v_F k_{F-} - \sqrt{v_F^2 k_{F-}^2 + 4\lambda_R^2} + 2\lambda_R\right)}\right]^2}{4v_F^2}, \tag{4.24}$$

and in particular to $v_F q_{cr}^- \approx 0.019\mu$ and $v_F q_{cr}^+ \approx 0.025\mu$ for $\lambda_{R/I} = 0.25\mu$, in accordance with Fig. 4.2(c). However, for a proper analysis the full ELF needs to be discussed. This is done in Fig. 4.5 for two different combinations of the SOC parameters, $\lambda_R = \lambda_I = 0.25\mu$ (top) and $\lambda_R = 0.25\mu$ and $\lambda_I = 0$ (bottom), explicitly showing how spectral weight is transferred from the lower to the upper mode as momentum is increased and explaining the step in the plasmon spectrum as shown in Fig. 4.4. Notice that the pseudo-gap in the plasmon spectrum always appears for $\lambda_R < 0.5\mu$, since then in any case two conduction bands are occupied, independently of the actual value of λ_I, but its width decreases for

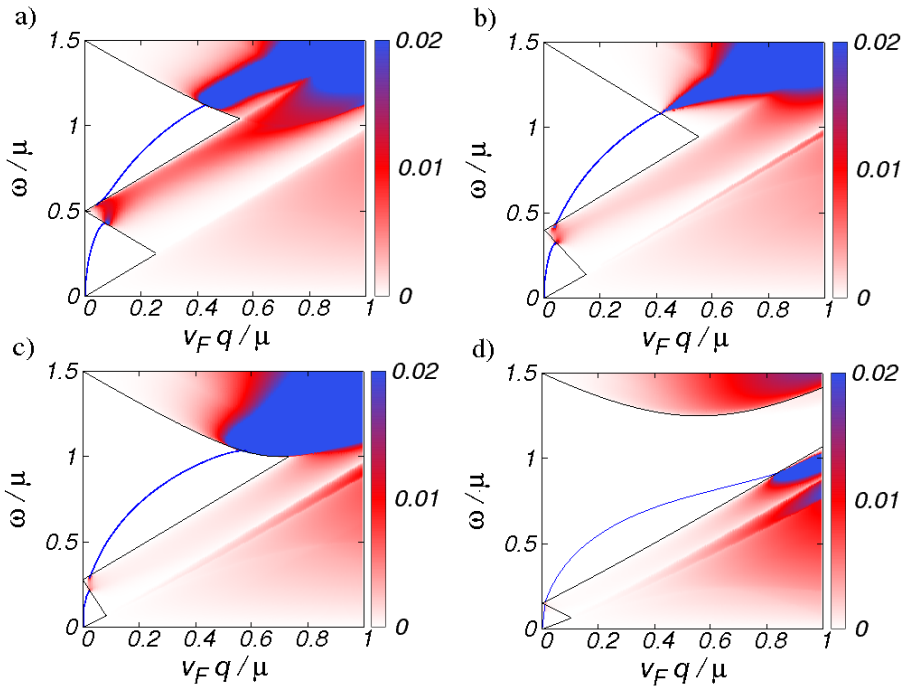

Figure 4.4.: Density plot of the ELF (normalized to $V(q)\mu/v_F^2$) for (a) $(\lambda_R/\mu, \lambda_I/\mu) = (0.25, 0)$, (b) $(0.25, 0.25)$, (c) $(0.25, 0.5)$, and (d) $(0.25, 0.75)$. The solid blue lines show the undamped plasmon modes. The black lines indicate the boundaries of the EHC; see Sec. 4.2.2.

increasing λ_I as the dissipative region due to interband transitions diminishes. In the opposite case of $\lambda_R > 0.5\mu$, depending on λ_I either one or two bands can be occupied: For zero intrinsic coupling the pseudo-gap is absent. For finite λ_I its width increases up to a maximum value at around $\lambda_I \approx \lambda_R$.

Let us close with a comment on plasmons in undoped graphene. A numerical inspection shows that the real part of the DF is always positive and the ELF does not exhibit a resonance. Therefore, within our model plasmons are absent at the charge neutrality point. However, recent theoretical works have shown that for neutral graphene, plasmons can exist if one takes into account the effect of circularly polarized light [102], effects beyond RPA [103], and in bilayer graphene by including trigonal warping [104].

4.4. Screening of impurities

In order to understand the transport characteristics of solids, it is of great importance to know how impurities in a sample become screened. The screened Coulomb potential of a static impurity with charge Q can be obtained directly from the definition of the DF [91]:

$$\Phi(r) = \frac{Q}{\epsilon_0} \int_0^\infty dq \, \frac{J_0(qr)}{\varepsilon(q,0)}. \tag{4.25}$$

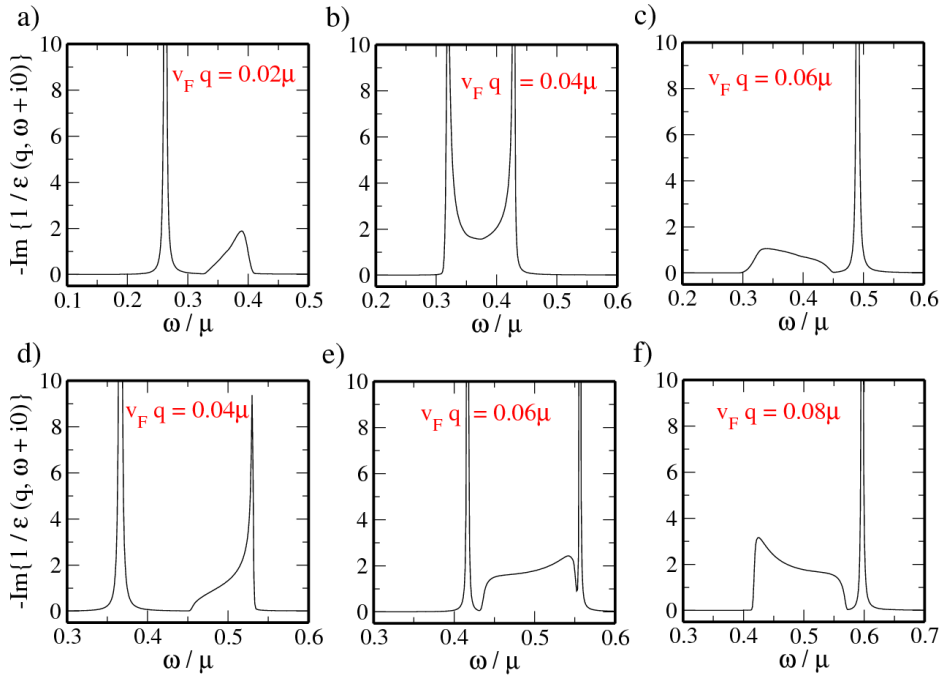

Figure 4.5.: Top: ELF for $\lambda_R = \lambda_I = 0.25\mu$ and various momenta. Bottom: The same for $\lambda_R = 0.25\mu$ and $\lambda_I = 0$.

Here, we have explicitly made use of the isotropy of the problem and introduced the Bessel function of the first kind

$$J_0(x) = \frac{1}{2\pi}\int_0^{2\pi} d\phi_k \, e^{ix\cos\phi_k}. \tag{4.26}$$

Combining Eq. (4.25) with the expressions for the DF in Sec. 4.2, the screened potential for the undoped system is calculated numerically. At the charge neutrality point $\Phi(r)$ is mainly determined by the long-wavelength behavior of the static correlator [100]. As can be seen from Fig. 4.6(a), the long-wavelength limit of the free polarizability, $\chi^{0,un}_{\rho\rho}(q \to 0, 0)$, is finite for $\lambda_R > \lambda_I$ and zero otherwise, while for large momenta the polarizability scales like $\chi(q, 0) \propto q^{-1}$ in all cases. Figure 4.7 demonstrates that for $\lambda_I \gtrsim \lambda_R$ the potential behaves as $\Phi(r) \propto r^{-1}$ at large distances away from the impurity, whereas in the opposite case, $\lambda_R > \lambda_I$, the asymptotic potential is of the form $\Phi(r) \propto r^{-3}$. The actual values of $\lambda_+ r/v_F$ at which the above asymptotics are appropriate approximations depend on the difference of λ_R and λ_I. As mentioned in Sec. 2.1.2, the two different parameter regimes belong to different phases separated by the quantum critical point at $\lambda_R = \lambda_I$.

The static density correlator for the doped system is much more complicated. Integrals of the form Eq. (4.25) are usually treated analytically by approximating the Bessel function by its asymptotic values. The subsequent Fourier integral can then be solved with the Lighthill theorem [105]. This theorem states that singularities in the derivatives of the DF give rise to a characteristic oscillating decay of the screened potential. Physically, these

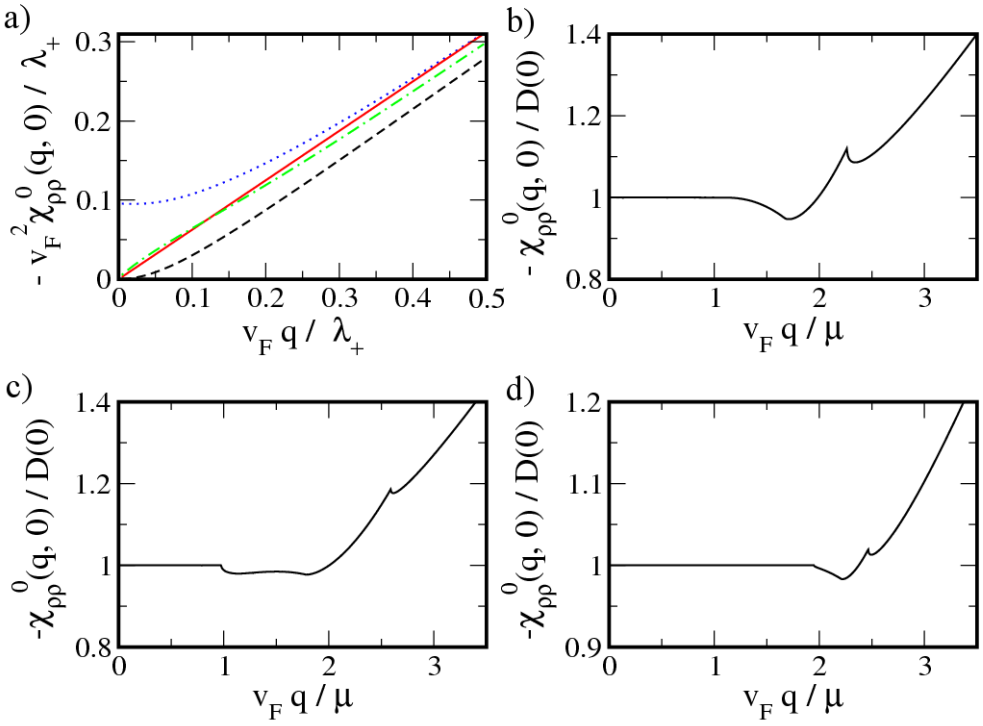

Figure 4.6.: Static polarizability of (a) undoped graphene with fixed λ_+: $\lambda_R = 2\lambda_I$ (dotted), $\lambda_R = \lambda_I$ (dotted-dashed), $\lambda_I = 2\lambda_R$ (dashed), $\lambda_R = \lambda_I = 0$ (straight), and doped graphene with (b) $\lambda_R = \lambda_I = 0.3\mu$, (c) $\lambda_R = 2\lambda_I = 0.3\mu$, and (d) $2\lambda_R = \lambda_I = 0.3\mu$ in units of $D(0) = g_v\mu/\pi v_F^2$.

Friedel oscillations are due to backscattering on the Fermi surface. We can thus make qualitative predictions for the potential $\Phi(r)$ at large distances away from the impurity, only from the analytical structure of the polarizability without carrying out the integration. In addition to that, Fig. 4.8 shows the exact numerical solution of Eq. (4.25). For nonzero SOC and $\lambda_R \neq \lambda_I$ the first derivative of the polarizability is singular at two different momenta; see Figs. 4.6(c) and (d). According to Lighthill's theorem the potential is expected to exhibit a superposition of two different kinds of oscillations where, at leading order, both contributions scale as $\Phi_\pm(r) \propto r^{-2}$. For predominant intrinsic SOIs the two oscillatory parts interfere constructively, finally yielding an additional spin-degeneracy factor of $g_s = 2$ and the solution can be well described by ($k_F \equiv k_{F\pm}$) [99]

$$\Phi(r) = -\frac{Q\lambda_I^2}{4\pi\epsilon_0\epsilon_r r_0 \mu^2} \frac{(2k_F)^2}{\left(2k_F + \frac{1}{r_0}\right)^2} \frac{\sin(2k_F r)}{(2k_F r)^2}, \tag{4.27}$$

where $r_0 = \pi\epsilon_0\epsilon_r v_F^2/e^2\mu$. For $\lambda_R = \lambda_I$ the first derivative of $\chi_0(q,0)$ is singular only at $q = 2k_{F-}$; see Fig. 4.6(b). Therefore, the dominant part of the screened potential again is of the order $(k_{F-}r)^{-2}$. However, an additional contribution which scales as $(k_{F+}r)^{-3}$ needs to be added. The numerical inspection of $\Phi(r)$ in Fig. 4.8 confirms the above predictions

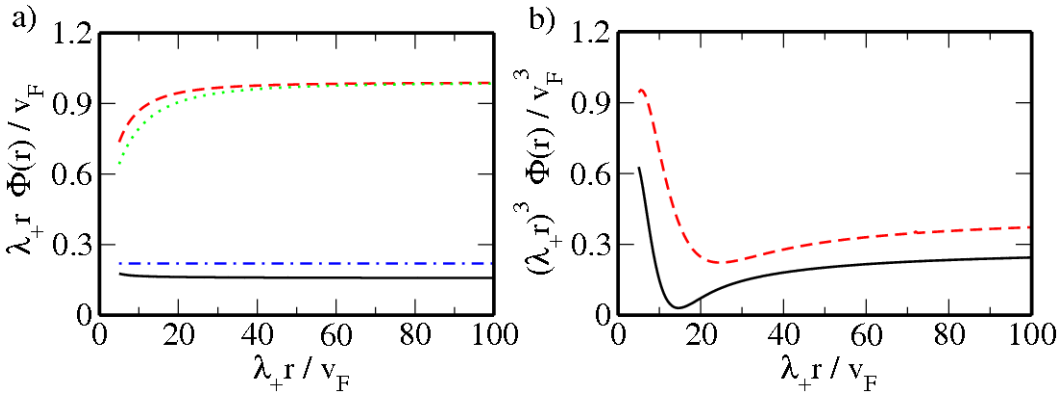

Figure 4.7.: Asymptotic screened potential (in units of $Q\lambda_+/\epsilon_0 v_F$) of undoped graphene for fixed λ_+ and different SOC parameters: (a) $\lambda_R = \lambda_I$ (solid line), $\lambda_I = 2\lambda_R$ (dashed), and $\lambda_R = 0$ (dotted). Also shown is the SOC-free case $\lambda_R = \lambda_I = 0$ (dotted-dashed). (b) $\lambda_I = 0$ (solid) and $\lambda_R = 2\lambda_I$ (dashed).

and in particular shows that the screened potential deviates significantly from the

$$\Phi(r) \propto \frac{\cos(2k_F r)}{(2k_F r)^3} \tag{4.28}$$

behavior of standard graphene within the Dirac cone approximation [61, 106]. Nevertheless, it should be emphasized that including the full TB dispersion can also lead to Friedel oscillations decaying like r^{-2} [107].

4.5. Summary

In summary, we have presented analytical and numerical results for the DF of graphene in the presence of SOIs of the intrinsic and Rashba type within the RPA for finite frequency, wave vector, and doping. Several limiting cases such as the case of predominant Rashba and intrinsic coupling, and the case of equally large SOIs were opposed.

We have demonstrated that SOIs in graphene can be used to manipulate the plasmon energies and damping rates. As examples we have mentioned the ability to turn off damping of plasmons for large momenta if λ_I is sufficiently large and, on the other hand, to introduce damping even for small momenta due to interband transitions between the various conduction bands for $\lambda_R \neq 0$. Both aspects might be useful to gain further control in possible plasmonic circuitries based on graphene. Moreover, when the spin-degeneracy of the bands gets lifted, the existence of a new plasmon mode with an energy much larger compared to the long-wavelength result is predicted. Unfortunately, this mode lies in the region with finite Landau damping which might cause difficulties to detect it experimentally.

In the last section of this chapter the static screening properties were discussed. It was shown that the relative magnitude of the SOC parameters determines the power-law

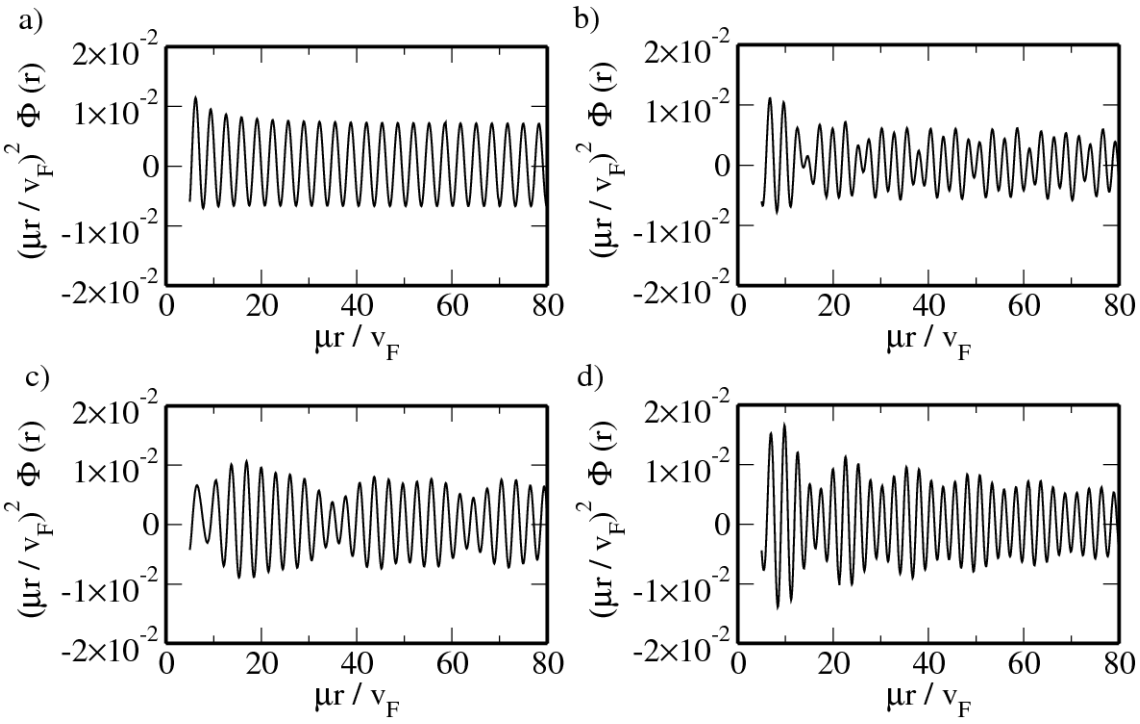

Figure 4.8.: Asymptotic screened potential (in units of $Q\mu/\epsilon_0 v_F$) of doped graphene for various SOC parameters: (a) $(\lambda_R/\mu, \lambda_I/\mu) = (0, 0.3)$, (b) $(0.3, 0.15)$, (c) $(0.15, 0.3)$, and (d) $(0.3, 0.3)$.

dependence of the screened potential of an undoped sample. While for $\lambda_R > \lambda_I$ the potential scales like $\Phi(r) \propto 1/r^3$, for $\lambda_I \geq \lambda_R$ a weaker screening of $\Phi(r) \propto 1/r$ was found. On the other hand, for a finite carrier density a beating of Friedel oscillations occurs if λ_R is nonzero due to the existence of two inequivalent Fermi wave vectors. For large $\lambda_I \gg \lambda_R$, this beating vanishes and the two contributions interfere constructively.

It should be emphasized that in order to see noticeable effects in the plasmon spectrum or screening behavior, the SOC constants need to be sufficiently large, i.e., of the order of the Fermi energy. However, although SOIs in pristine graphene are naturally very small, our results can also be applied to graphene lying on a substrate [41, 42] and, at least qualitatively, to other promising 2D hexagonal system such as silicene [46, 47] or ML-MDS [53, 54, 55]. A thorough analysis of the dielectric properties of the latter is the subject of Chap. 6.

Chapter 5.

5 Dynamical current-current susceptibility of gapped graphene

Parts of this chapter have been published in collaboration with John Schliemann in Phys. Rev. B 83, 235409 (2011).

In the previous chapter we have studied in detail the charge response of graphene including SOIs of the intrinsic and Rashba type. The aim of the present chapter is to generalize these results to the current-current susceptibility, where, for the moment, we will concentrate on the effect of a purely intrinsic SOC and neglect the Rashba contribution. As the intrinsic part leads to the opening of a band gap of magnitude $2\lambda_I$ and to a finite effective carrier mass, we will also refer to λ_I as a mass term and denote the corresponding model as gapped graphene.

The interest in the current-current susceptibility of gapped graphene is manifold:

(i) From the current-current susceptibility we can immediately obtain the conductivity from the simple relation [92]

$$\sigma_{\alpha\beta}(\boldsymbol{q},\omega) = i\,\frac{e^2\,\chi_{\boldsymbol{j}_\alpha\boldsymbol{j}_\beta}(\boldsymbol{q},\omega)}{\omega}, \quad \text{with} \quad \alpha,\beta = x,y, \tag{5.1}$$

a quantity which can be measured in transport experiments.

(ii) The static limit of $\chi_{\boldsymbol{j}_\alpha\boldsymbol{j}_\beta}$ allows to extract information on the orbital and Pauli part of the magnetic susceptibility [91], i.e., the screening of an applied magnetic field. While the former is due to the orbital motion of the charge carriers, the latter arises from the real spin degree of freedom.

(iii) It is interesting to compare the nonrelativistic limit of gapped graphene, i.e., the limit of a band gap parameter comparable to the chemical potential, to the situation in a 2DEG.

After a short summary of the formalism in Sec. 5.1, closed analytical expressions for the longitudinal and transversal parts of the current-current susceptibility are given in

Sec. 5.2. Taking the static limit of the current response, we determine the orbital and Pauli magnetization of gapped graphene. As described in Sec. 5.3, compared to gapless graphene the orbital magnetic susceptibility (OMS) at zero doping is smeared out on an energy scale given by the inverse of the band gap parameter. In contrast, for finite doping the OMS vanishes for arbitrary values of λ_I. In Sec. 5.4 the effect of an increasing mass term corresponding to the nonrelativistic limit of gapped graphene is discussed. The peculiar band structure of graphene leads to a pseudospin Zeeman term [60], formally equivalent to the ordinary Zeeman contribution, and hence to a special form of the OMS. A summary of the main results can be found in Sec. 5.5.

5.1. The model

The effective Hamiltonian of graphene near the corners of the BZ including a finite mass term is

$$\hat{H}_g^{\tau s} = v_F \boldsymbol{k} \cdot \hat{\boldsymbol{\sigma}}_\tau + s\tau\lambda_I \hat{\sigma}_z. \tag{5.2}$$

Concentrating on one valley ($\tau = +1$) and a single real spin component ($s = +1$), the eigensystem of the KMM simplifies to

$$E_{g,\pm}(k) = \pm\sqrt{v_F^2 k^2 + \lambda_I^2}, \tag{5.3}$$

and

$$|\xi_{g,\pm}(\boldsymbol{k})\rangle = \frac{1}{\sqrt{2}\left(v_F^2 k^2 + \lambda_I^2\right)^{1/4}} \begin{pmatrix} \sqrt{\sqrt{v_F^2 k^2 + \lambda_I^2} \pm \lambda_I} \\ \pm\sqrt{\sqrt{v_F^2 k^2 + \lambda_I^2} \mp \lambda_I}\, e^{i\phi_k} \end{pmatrix}, \tag{5.4}$$

where $\tan\phi_k = k_y/k_x$ is the in-plane angle. The current operator of gapped graphene,

$$\hat{\boldsymbol{j}} = \frac{\delta \hat{H}_g^{++}[\boldsymbol{k} + e\boldsymbol{A}]}{e\,\delta \boldsymbol{A}} = v_F \hat{\boldsymbol{\sigma}}, \tag{5.5}$$

equals the pseudospin operator up to a constant prefactor of v_F. Therefore, we can express the current-current susceptibility of the noninteracting system by

$$\chi^0_{\boldsymbol{j}_\alpha \boldsymbol{j}_\beta}(\boldsymbol{q}, \omega) = g_v g_s v_F^2 \sum_{\sigma_1,\sigma_2=\pm 1} \int \frac{d^2k}{(2\pi)^2} \frac{f[E_{g,\sigma_1}(k)] - f[E_{g,\sigma_2}(|\boldsymbol{k}+\boldsymbol{q}|)]}{\omega - E_{\sigma_2}(|\boldsymbol{k}+\boldsymbol{q}|) + E_{\sigma_1}(k) + i0} \times \\ \times \langle \xi_{g,\sigma_1}(\boldsymbol{k})|\, \hat{\boldsymbol{\sigma}}_\alpha\, |\xi_{g,\sigma_2}(\boldsymbol{k}+\boldsymbol{q})\rangle \langle \xi_{g,\sigma_2}(\boldsymbol{k}+\boldsymbol{q})|\, \hat{\boldsymbol{\sigma}}_\beta\, |\xi_{g,\sigma_1}(\boldsymbol{k})\rangle, \tag{5.6}$$

with $\alpha, \beta = x, y$. As before, $f[E]$ is the Fermi distribution function, in our case a step function as we assume zero temperature, and $g_v = g_s = 2$ count orbital and spin degeneracies. From Eq. (3.22) we know that the current-current susceptibility of graphene can be split up into a longitudinal and transversal part, where both can be obtained independently of each other. Because of Eq. (3.30) the longitudinal part directly follows from the

polarizability obtained in Chap. 4 for the special case of $\lambda_R = 0$, while the transversal part needs to be derived from the integral expression in Eq. (5.6). In the following we restrict our discussions, without loss of generality, to positive Fermi energies μ and mass term λ_I. The current operator is chosen to point along the x direction, i.e., the longitudinal part follows from the special choice of $\boldsymbol{q} = q\boldsymbol{e}_x$ and the transversal part from $\boldsymbol{q} = q\boldsymbol{e}_y$, with $\boldsymbol{e}_x$ ($\boldsymbol{e}_y$) being the unit vector in x (y) direction.

5.2. Analytical results for the current-current susceptibility

The current-current susceptibility can be solved in terms of closed analytical expressions. For details on the calculation we refer to App. B, where basic steps can be found. As in the previous chapter we distinguish between undoped and doped graphene. While the former corresponds to the case of zero carrier concentration, i.e., the Fermi energy lies between the two bands ($|\lambda_I| > |\mu|$), in the latter the Fermi energy lies either in the conduction or in the valence band.

5.2.1. Zero doping

In the undoped case, only transitions from the valence to the conduction band contribute to Eq. (5.6). The result for the imaginary part is

$$\mathrm{Im}\left\{\chi_{jj}^{0,L/T,un}(q,\omega)\right\} = -\frac{g_v g_s \omega}{16}\sqrt{1-\left(\frac{v_F q}{\omega}\right)^2}^{\mp 1}\left(1+\frac{4\lambda_I^2}{\omega^2 - v_F^2 q^2}\right)\theta\left[\omega^2 - v_F^2 q^2 - 4\lambda_I^2\right]. \tag{5.7}$$

The upper (lower) sign stands for the longitudinal (transversal) component. For the real part we obtain

$$\mathrm{Re}\left\{\chi_{jj}^{0,L,un}(q,\omega)\right\} = -\frac{g_v g_s D}{8\pi} - \frac{g_v g_s \omega^2}{4\pi}\left\{\frac{\lambda_I}{v_F^2 q^2 - \omega^2} + \frac{v_F^2 q^2 - \omega^2 - 4\lambda_I^2}{4\left|v_F^2 q^2 - \omega^2\right|^{3/2}}\times\right.$$
$$\left.\times\left[\theta\left[v_F q - \omega\right]\arccos\left(\frac{v_F^2 q^2 - \omega^2 - 4\lambda_I^2}{\omega^2 - v_F^2 q^2 - 4\lambda_I^2}\right) - \theta\left[\omega - v_F q\right]\ln\frac{\left(2\lambda_I + \sqrt{\omega^2 - v_F^2 q^2}\right)^2}{\left|\omega^2 - v_F^2 q^2 - 4\lambda_I^2\right|}\right]\right\} \tag{5.8}$$

and

$$\mathrm{Re}\left\{\chi_{jj}^{0,T,un}(q,\omega)\right\} = -\frac{g_v g_s\left(D - 2\lambda_I\right)}{8\pi} - \frac{g_v g_s\left(4\lambda_I^2 - v_F^2 q^2 + \omega^2\right)}{16\pi\sqrt{\left|v_F^2 q^2 - \omega^2\right|}}\times$$
$$\times\left[\theta\left[v_F q - \omega\right]\arccos\left(\frac{v_F^2 q^2 - \omega^2 - 4\lambda_I^2}{\omega^2 - v_F^2 q^2 - 4\lambda_I^2}\right) - \theta\left[\omega - v_F q\right]\ln\frac{\left(2\lambda_I + \sqrt{\omega^2 - v_F^2 q^2}\right)^2}{\left|\omega^2 - v_F^2 q^2 - 4\lambda_I^2\right|}\right], \tag{5.9}$$

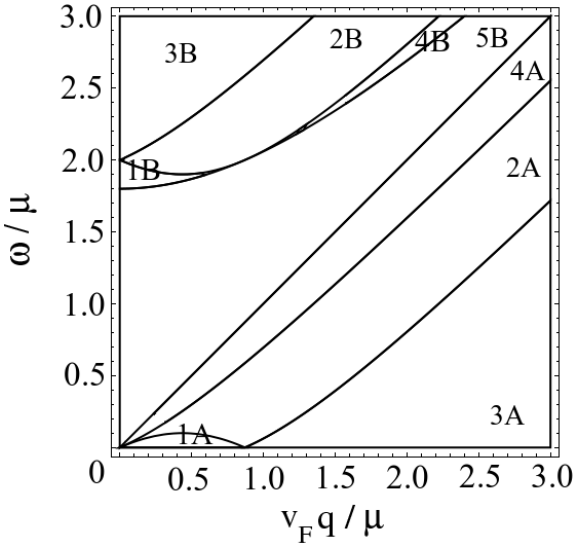

Figure 5.1.: The different regions related to the imaginary and real parts of the current-current susceptibility for the special case of $\lambda_I = 0.9\mu$. See Table 5.1 for the definitions of 1A-5B.

with D being the energy cutoff introduced in Sec. 3.1.

5.2.2. Finite doping

We have two contributions for the doped case:

$$\chi_{jj}^{0,L/T,do}(q,\omega) = \chi_{jj}^{0,L/T,un}(q,\omega) + \delta\chi_{jj}^{0,L/T,do}(q,\omega)\,. \tag{5.10}$$

The first one is the undoped part where only interband transitions contribute (see above), while the second takes into account intraband transitions. In App. B the explicit expression for the latter can be found. Adding up both contributions we end up with the final results:

$$\mathrm{Im}\left\{\chi_{jj}^{0,L/T,do}(q,\omega)\right\} = -\frac{g_v g_s \omega}{16\pi}\sqrt{\left|1-\left(\frac{v_F q}{\omega}\right)^2\right|}^{\mp 1} \times \begin{cases} G_>^{\mp}\left(\frac{2\mu+\omega}{v_F q}\right) - G_>^{\mp}\left(\frac{2\mu-\omega}{v_F q}\right) & \text{1A} \\ 0 & \text{1B} \\ G_>^{\mp}\left(\frac{2\mu+\omega}{v_F q}\right) & \text{2A} \\ \mp G_<^{\mp}\left(\frac{2\mu-\omega}{v_F q}\right) & \text{2B} \\ 0 & \text{3A} \\ \pi\left(1+\frac{4\lambda_I^2}{\omega^2-v_F^2 q^2}\right) & \text{3B} \\ 0 & \text{4A} \\ \pi\left(1+\frac{4\lambda_I^2}{\omega^2-v_F^2 q^2}\right) & \text{4B} \\ 0 & \text{5B} \end{cases} \tag{5.11}$$

and

$$\mathrm{Re}\left\{\chi_{jj}^{0,L/T,do}(q,\omega)\right\} = -\frac{g_v g_s D}{8\pi} \mp \frac{g_v g_s \mu \omega^2}{2\pi v_F^2 q^2}$$
$$\pm \frac{g_v g_s \omega}{16\pi}\sqrt{\left|1-\left(\frac{v_F q}{\omega}\right)^2\right|}^{\mp 1} \times \begin{cases} 0 & \text{1A} \\ G_>^{\mp}\left(\frac{2\mu+\omega}{v_F q}\right) - G_>^{\mp}\left(\frac{2\mu-\omega}{v_F q}\right) & \text{1B} \\ \pm G_<^{\mp}\left(\frac{2\mu-\omega}{v_F q}\right) & \text{2A} \\ G_>^{\mp}\left(\frac{2\mu+\omega}{v_F q}\right) & \text{2B} \\ \pm G_<^{\mp}\left(\frac{2\mu-\omega}{v_F q}\right) \pm G_<^{\mp}\left(\frac{2\mu+\omega}{v_F q}\right) & \text{3A} \\ G_>^{\mp}\left(\frac{2\mu+\omega}{v_F q}\right) - G_>^{\mp}\left(\frac{-2\mu+\omega}{v_F q}\right) & \text{3B} \\ \pm G_<^{\mp}\left(\frac{2\mu-\omega}{v_F q}\right) \mp G_<^{\mp}\left(\frac{2\mu+\omega}{v_F q}\right) & \text{4A} \\ G_>^{\mp}\left(\frac{2\mu+\omega}{v_F q}\right) + G_>^{\mp}\left(\frac{-2\mu+\omega}{v_F q}\right) & \text{4B} \\ G_0^{\mp}\left(\frac{2\mu+\omega}{v_F q}\right) - G_0^{\mp}\left(\frac{2\mu-\omega}{v_F q}\right) & \text{5B} \end{cases} . \tag{5.12}$$

Here, we defined the functions [99]

$$G_<^{\pm} = x\sqrt{x_0^2 - x^2} \pm \left(2 - x_0^2\right) \arccos\left(\frac{x}{x_0}\right), \tag{5.13a}$$

$$G_>^{\pm} = x\sqrt{x^2 - x_0^2} \pm \left(2 - x_0^2\right) \operatorname{arccosh}\left(\frac{x}{x_0}\right), \tag{5.13b}$$

$$G_0^{\pm} = x\sqrt{x^2 - x_0^2} \pm \left(2 - x_0^2\right) \operatorname{arcsinh}\left(\frac{x}{|x_0|}\right), \tag{5.13c}$$

with

$$x_0 = \sqrt{1 + \frac{4\lambda_I^2}{v_F^2 q^2 - \omega^2}}. \tag{5.14}$$

The regions (1A)-(5B) are defined in Table 5.1; see also Ref. [99]. Figure 5.1 illustrates the structure of the regions for the specific choice $\lambda_I = 0.9\mu$.

5.3. Static limit and magnetic susceptibility

In the static limit the purely real transversal susceptibilities are given by

$$\chi_{jj}^{0,T,un}(q,0) = -\frac{g_v g_s D}{8\pi} + \frac{g_v g_s \lambda_I}{4\pi} + \frac{g_v g_s v_F q}{8\pi}\left(1 - \frac{4\lambda_I^2}{v_F^2 q^2}\right) \arccos\left(\frac{2\lambda_I}{\sqrt{4\lambda_I^2 + v_F^2 q^2}}\right) \tag{5.15}$$

1A:	$\omega < \mu - \sqrt{v_F^2(q-k_F)^2+\lambda_I^2}$
1B:	$q < 2k_F \wedge \sqrt{v_F^2q^2+4\lambda_I^2} < \omega < \mu + \sqrt{v_F^2(q-k_F)^2+\lambda_I^2}$
2A:	$\pm\mu \mp \sqrt{v_F^2(q-k_F)^2+\lambda_I^2} < \omega < -\mu + \sqrt{v_F^2(q+k_F)^2+\lambda_I^2}$
2B:	$\mu + \sqrt{v_F^2(q-k_F)^2+\lambda_I^2} < \omega < \mu + \sqrt{v_F^2(q+k_F)^2+\lambda_I^2}$
3A:	$\omega < -\mu + \sqrt{v_F^2(q-k_F)^2+\lambda_I^2}$
3B:	$\omega > \mu + \sqrt{v_F^2(q+k_F)^2+\lambda_I^2}$
4A:	$-\mu + \sqrt{v_F^2(q+k_F)^2+\lambda_I^2} < \omega < v_Fq$
4B:	$q > 2k_F \ \wedge \ \sqrt{v_F^2q^2+4\lambda_I^2} < \omega < \mu + \sqrt{v_F^2(q-k_F)^2+\lambda_I^2}$
5B:	$v_Fq < \omega < \sqrt{v_F^2q^2+4\lambda_I^2}$

Table 5.1.: Definition of the different regions in the q-ω plane related to the imaginary and real parts of the current-current susceptibility.

and

$$\chi_{jj}^{0,T,do}(q,0) = -\frac{g_v g_s D}{8\pi} + \frac{g_v g_s v_F q}{8\pi}\left[\frac{2\mu}{v_F q}\sqrt{1-\left(\frac{2k_F}{q}\right)^2} + \left(1-\left(\frac{2\lambda_I}{v_F q}\right)^2\right)\arccos\left(\frac{2\mu}{\sqrt{v_F^2q^2+4\lambda_I^2}}\right)\right]\theta\left[q-2k_F\right], \tag{5.16}$$

respectively, while the longitudinal parts vanish, except for the constant cutoff-dependent term in front. The Fermi wave vector in Eq. (5.16) is $k_F = \sqrt{\mu^2-\lambda_I^2}/v_F$.

Figure 5.2 shows the renormalized function

$$\tilde{\chi}(q,0) = -\frac{e^2}{q^2}\left(\chi_{jj}^{0,T}(q,0) + \frac{g_v g_s D}{8\pi}\right) \tag{5.17}$$

for different values of $\Lambda_I = \lambda_I/\mu$. From its long-wavelength limit one can read off the OMS via [91]

$$\tilde{\chi}_{orb} = \lim_{q\to 0}\tilde{\chi}(q,0). \tag{5.18}$$

For the undoped part the OMS

$$\tilde{\chi}_{orb}^{un} = -\frac{g_v g_s e^2 v_F^2}{12\pi\lambda_I} \tag{5.19}$$

is finite and diamagnetic. Compared to the gapless case, the OMS is smeared out on an energy scale of $1/\lambda_I$. This broadening of $\tilde{\chi}_{orb}$ also occurs in the presence of disorder [108], as well as for finite temperature [109]. From Fig. 5.2 one can see that $\tilde{\chi}^{do}(q,0) = 0$ for

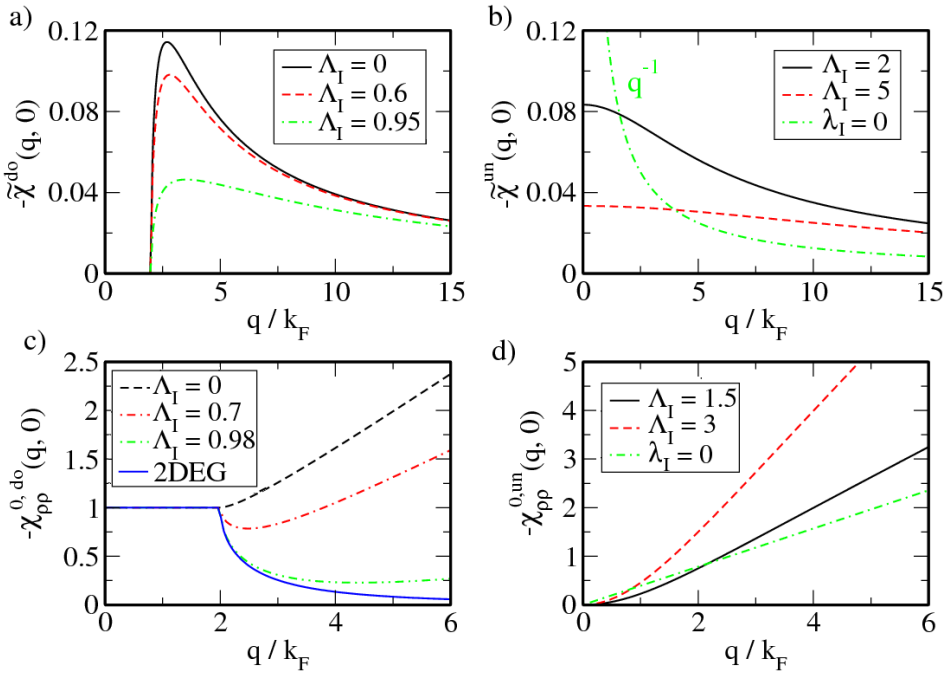

Figure 5.2.: Top: Static current-current susceptibility for (a) doped and (b) undoped graphene for different ratios $\Lambda_I = \lambda_I/\mu$ in units of $g_v g_s e^2\mu/2\pi k_F^2$. Bottom: Static polarizability for (c) doped and (d) undoped graphene in units of $g_v g_s \mu/2\pi v_F^2$.

$q < 2k_F$ and thus

$$\tilde{\chi}^{do}_{orb} = 0, \tag{5.20}$$

which is the same as for gapless graphene. The same result,

$$\tilde{\chi}_{orb} = -\frac{g_v g_s e^2 v_F^2}{12\pi\lambda_I}\,\theta\left[\lambda_I - \mu\right], \tag{5.21}$$

was obtained earlier by energy considerations [60, 110]. In the limit $\lambda_I = 0$ the OMS reduces to a delta function [96, 109, 111]:

$$\tilde{\chi}_{orb} = -\frac{g_v g_s e^2 v_F^2}{6\pi}\delta\left(\mu\right). \tag{5.22}$$

The expressions for the magnetic susceptibility given above are only valid for the noninteracting system. A simple way to include many-body effects is via the RPA [91]. From the OMS in RPA [111],

$$\tilde{\chi}^{RPA}_{orb} = \lim_{q\to 0}\frac{\tilde{\chi}(q,0)}{1+\frac{q}{2\epsilon_0\epsilon_r v_F^2}\tilde{\chi}(q,0)} = -\frac{g_v g_s e^2 v_F^2}{12\pi\lambda_I}\theta\left[\lambda_I - \mu\right], \tag{5.23}$$

one can see that screening effects do not change the orbital part of the magnetic susceptibility of gapped graphene. However, the situation changes if one includes interaction effects in first-order perturbation theory beyond RPA, leading to paramagnetic behavior in doped graphene sheets [112].

The Pauli part of the magnetic susceptibility follows from the limit

$$\tilde{\chi}_P = -\mu_B^2 \lim_{q\to 0} \chi_{s_z s_z}(q,0), \tag{5.24}$$

where $\mu_B = e/2m_0$ is the Bohr magneton. The spin susceptibility $\chi_{s_z s_z}(q,0)$ of a noninteracting system equals the free polarizability [91]. Combining Eqs. (5.8) and (5.12) with Eq. (3.30), the static polarizabilities read [99]

$$\chi_{\rho\rho}^{0,un}(q,0) = -\frac{g_v g_s \lambda_I}{4\pi v_F^2} + \frac{g_v g_s \left[4\lambda_I^2 - v_F^2 q^2\right]}{8\pi v_F^3 q} \arccos\left(\frac{2\lambda_I}{\sqrt{4\lambda_I^2 + v_F^2 q^2}}\right) \tag{5.25}$$

and

$$\chi_{\rho\rho}^{0,do}(q,0) = -\frac{g_v g_s \mu}{2\pi v_F^2} \left\{ 1 - \frac{1}{2} \left[\sqrt{1 - \left(\frac{2k_F}{q}\right)^2} - \frac{v_F^2 q^2 - 4\lambda_I^2}{2 v_F q \mu} \arccos\left(\frac{2\mu}{\sqrt{v_F^2 q^2 + 4\lambda_I^2}}\right) \right] \theta\left[q - 2k_F\right] \right\}. \tag{5.26}$$

Figures 5.2(c) and (d) show the static polarizability for different ratios of Λ_I. The case $\Lambda_I \to 1$ corresponds to the nonrelativistic limit of graphene and will be discussed in the next section. From the long-wavelength limit one can easily see that the Pauli part of the magnetic susceptibility vanishes in the undoped case, reflecting the vanishing DOS at the charge neutrality point, while the doped part is finite:

$$\tilde{\chi}_P = \frac{g_v g_s e^2 \mu}{8\pi m_0^2 v_F^2} \theta\left[\mu - \lambda_I\right]. \tag{5.27}$$

5.4. Nonrelativistic limit of gapped graphene

The static transversal part of the current-current susceptibility for the 2DEG [91],

$$\chi_{jj}^{0,T,2DEG}(q,0) = \frac{g_v g_s q^2}{24\pi m_0} \left[1 - \left(1 - \frac{4k_F^2}{q^2}\right)^{3/2} \theta\left[q - 2k_F\right] \right], \tag{5.28}$$

leads to the OMS

$$\tilde{\chi}_{orb}^{2DEG} = -\frac{g_v g_s e^2}{24\pi m_0}. \tag{5.29}$$

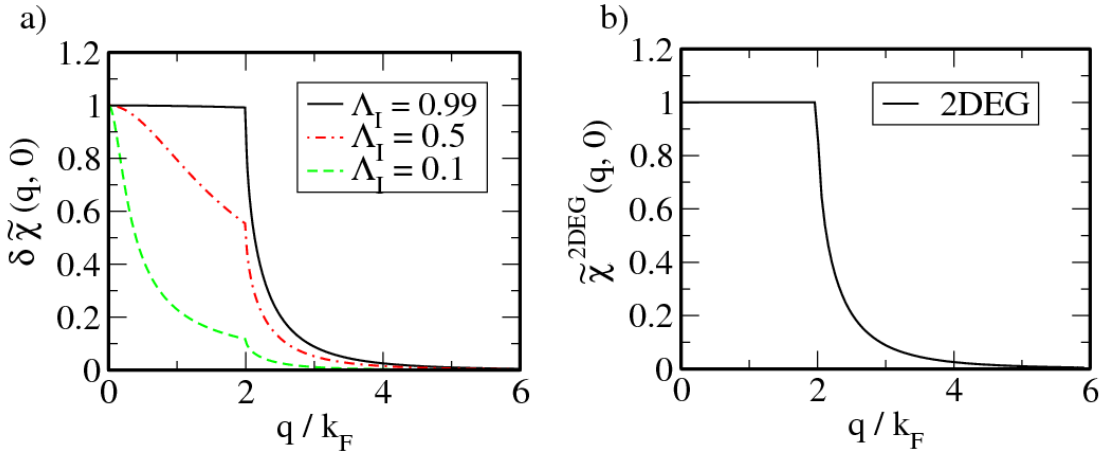

Figure 5.3.: (a) Intraband part of the transversal current-current susceptibility of graphene for different ratios $\Lambda_I = \lambda_I/\mu$ in units of $g_v g_s e^2 v_F^2/12\pi\lambda_I$. (b) Sum of orbital and Pauli contribution in an 2DEG in units of $g_v g_s e^2/12\pi m_0$.

From the static polarizability [63, 91],

$$\chi_{\rho\rho}^{0,2DEG}(q,0) = -\frac{g_v g_s m_0}{2\pi}\left[1 - \sqrt{1-\left(\frac{2k_F}{q}\right)^2}\,\theta\left[q-2k_F\right]\right], \tag{5.30}$$

we obtain the Pauli contribution to the magnetic susceptibility:

$$\tilde{\chi}_P^{2DEG} = \mu_B^2\,\frac{g_v g_s m_0}{2\pi} = \frac{g_v g_s e^2}{8\pi m_0}. \tag{5.31}$$

In Fig. 5.3(b) we show the momentum-dependent function

$$\begin{aligned}\tilde{\chi}^{2DEG}(q,0) &= -\mu_B^2\,\chi_{\rho\rho}^{0,2DEG}(q,0) - \frac{e^2\,\chi_{jj}^{0,T,2DEG}(q,0)}{q^2} \\ &= \frac{g_v g_s e^2}{12\pi m_0}\left[1 - \frac{3}{2}\theta\left[q-2k_F\right]\left\{\sqrt{1-\left(\frac{2k_F}{q}\right)^2} - \frac{1}{3}\left(1-\left(\frac{2k_F}{q}\right)^2\right)^{3/2}\right\}\right],\end{aligned} \tag{5.32}$$

whose long-wavelength limit determines the total magnetic susceptibility of the 2DEG:

$$\tilde{\chi}_{tot}^{2DEG} = \lim_{q\to 0}\tilde{\chi}^{2DEG}(q,0) = \frac{g_v g_s e^2}{12\pi m_0}. \tag{5.33}$$

Expanding now the Hamiltonian of gapped graphene in Eq. (5.2) in the limit

$$v_F\left|\boldsymbol{k} + e\boldsymbol{A}\right| \ll \lambda_I, \tag{5.34}$$

and eliminating the lower spinor component, one finds for the conduction band for a single

spin component [60]

$$\hat{H}_A^\tau = \frac{v_F^2 \left(\boldsymbol{k} + e\boldsymbol{A}\right)^2}{2\lambda_I} - \frac{\tau}{2}\mathcal{G}^* \mu_B B, \tag{5.35}$$

where

$$\mathcal{G}^* = 2\frac{m_0 v_F^2}{\lambda_I} \tag{5.36}$$

is the effective Landé factor and B the magnetic field associated with the vector potential. Equation (5.35) is nothing but the well-known Hamiltonian of the 2DEG, including a Zeeman term whose sign depends on the valley index. This Zeeman term, however, arises due to the peculiar band structure of graphene in contrast to the ordinary Zeeman term caused by the real spin. Therefore, the second part of Eq. (5.35) is also denoted as the pseudospin Zeeman term [60]. As shown in Fig. 5.3(a), for a large mass term ($\Lambda_I \to 1$) the current-current susceptibility associated with $\hat{H}_A$,

$$\delta\tilde{\chi}(q,0) = -\frac{e^2}{q^2}\left[\chi_{jj}^{0,T,do}(q,0) - \chi_{jj}^{0,T,un}(q,0)\right], \tag{5.37}$$

approaches the value of the 2DEG in Eq. (5.32). The corresponding OMS is then given by the paramagnetic term

$$\delta\tilde{\chi}_{orb} = \lim_{q\to 0}\delta\tilde{\chi}(q,0) = \frac{g_v g_s e^2 v_F^2}{12\pi\lambda_I}. \tag{5.38}$$

This means that the OMS of gapped graphene (neglecting the valence band states) reproduces the total susceptibility of a 2DEG, i.e., the sum of the orbital and Pauli part, if we associate $\lambda_I = m_0 v_F^2$. In addition to that, Eq. (5.27) describes the Pauli part due to the real spin. In the nonrelativistic limit,

$$\mu \approx \lambda_I + \frac{v_F^2 k_F^2}{2\lambda_I}, \tag{5.39}$$

Eq. (5.27) simplifies to

$$\tilde{\chi}_P \approx \frac{g_v g_s e^2 \lambda_I}{8\pi m_0^2 v_F^2}, \tag{5.40}$$

in accordance with the corresponding result for the 2DEG.

5.5. Summary

We have provided closed analytical expressions for the current-current susceptibility of graphene for arbitrary frequencies, wave vectors, and doping, including a mass term whose sign depends on the sublattice degree of freedom. Such a mass term has been shown to arise due to intrinsic SOIs [71] and the effect of a suitable substrate material [113].

From the static limit of the transversal and longitudinal parts we could determine the orbital and Pauli magnetic susceptibility of gapped graphene. While the orbital part was shown to vanish for nonzero doping independently of a band gap, right at the charge neutrality point the OMS is smeared out on an energy scale given by the inverse of λ_I. In contrast, the Pauli contribution was found to be finite and in particular positive in the doped case, and vanishes for zero chemical potential.

In Sec. 5.4 we have studied the nonrelativistic limit of gapped graphene. The Hamiltonian of graphene for a sufficiently large mass term is equivalent to that of a 2DEG; but with one particularity, namely the existence of a pseudospin Zeeman term [60]. Let us point out that the nonrelativistic limit of graphene is interesting not only because of academic questions, but rather has a meaning in the context of other honeycomb structures such as ML-MDS. According to Eq. (2.31) and Ref. [53], in first approximation the magnetic susceptibility of ML-MDS immediately follows from Eqs. (5.21) and (5.27):

$$\tilde{\chi}^m_{orb} = -\frac{4e^2a_0^2t_0^2\Delta}{3\pi\left[\Delta^2-\lambda_I^2\right]}\,\theta\left[\frac{\Delta}{2}-\mu\right] \tag{5.41}$$

and

$$\tilde{\chi}^m_{P} = \frac{e^2\mu}{2\pi m_0^2a_0^2t_0^2}\theta\left[\mu-\frac{\Delta}{2}\right]. \tag{5.42}$$

A detailed discussion of the charge response of ML-MDS including the effects of the different electron and hole masses and trigonal warping is given in the next chapter.

Chapter 6.

6 Plasmons and screening in a monolayer of MoS_2

Parts of this chapter have been published in collaboration with Tobias Stauber and John Schliemann in Phys. Rev. B 88, 035135 (2013).

Having studied in great detail the charge and current responses of graphene, we will now conduct a thorough investigation of the plasmon dispersion and the screening properties of ML-MDS, a related material. As mentioned previously in Sec. 2.2, the main quantitative differences in the energy spectra of ML-MDS and graphene are the remarkable band gap (of 1.82 eV) and the large intrinsic SOC (about 80 meV) in the former.

From the effective low-energy Hamiltonian of ML-MDS derived in Ref. [53] [see also Eq. (2.31)], we could immediately express the free polarizability and the current-current susceptibility of ML-MDS using the analytical results presented in Chaps. 4 and 5. However, as pointed out in Refs. [54, 55] the model of Ref. [53] is insufficient to properly account for the different electron and hole masses and needs to be extended according to Eq. (2.27). We restrict ourselves for the rest of the chapter to the case of a finite charge carrier density, as in usual experiments doping is always present, and the most interesting physics (such as the existence of collective charge excitations and Friedel oscillations) is expected to appear only for finite doping. As the energies and eigenstates of ML-MDS are quite complicated, analytical progress seems to be difficult and the DF is solved by numerical methods.

Section 6.1 begins with the discussion of the DOS of ML-MDS. This is followed in Sec. 6.2 by a detailed analysis of the plasmon spectrum for two different carrier concentrations, $n = 10^{12}$ cm^{-2} (used in the experiment of Ref. [80]) and $5 \cdot 10^{13}$ cm^{-2} (where both valence bands are filled in the p-doped case). While in graphene damping of plasmons is caused by interband transitions [61, 62], due to the large direct band gap in ML-MDS collective charge excitations enter the intraband EHC similarly to the situation in a 2DEG [63]. Since there is no electron-hole symmetry in ML-MDS, the plasmon energies in p- and n-doped samples clearly differ. In Sec. 6.3 we calculate the screened Coulomb potential of a static charged impurity. It turns out that the lifting of the spin degeneracy caused by the large intrinsic SOC leads to a distinct beating of Friedel oscillations for sufficiently

high carrier concentrations, for holes as well as for electrons. The chapter ends with a brief summary of the results in Sec. 6.4.

6.1. The model

We describe a monolayer of MoS_2 around the corners of the BZ by the effective two-band model of Eq. (2.27) for both spin ($s = \pm 1$) and valley ($\tau = \pm 1$) components [54, 55]:

$$\begin{aligned}\hat{H}_m^{\tau s} = &\frac{\Delta}{2}\hat{\sigma}_z + \tau s \lambda_I \frac{1-\hat{\sigma}_z}{2} + t_0 a_0 \boldsymbol{k}\cdot\hat{\boldsymbol{\sigma}}_\tau \\ &+ \frac{k^2}{4m_0}\left(\alpha + \beta\hat{\sigma}_z\right) + t_1 a_0^2 \boldsymbol{k}\cdot\hat{\boldsymbol{\sigma}}_\tau^* \hat{\sigma}_x \boldsymbol{k}\cdot\hat{\boldsymbol{\sigma}}_\tau^*.\end{aligned}$$

The TB parameters in $\hat{H}_m^{\tau s}$ are summarized in Table 2.1. From the analytical solution of the energies in Eq. (2.28),

$$\begin{aligned}E_{m,\pm}^{\tau s}(\boldsymbol{k}) = &\frac{\alpha}{4m_0}k^2 + \frac{s\tau\lambda_I}{2} \pm \Bigg\{\left(a_0^4 t_1^2 + \frac{\beta^2}{16 m_0^2}\right)k^4 + \left(\frac{\Delta - s\tau\lambda_I}{2}\right)^2 \\ &+ k^2\left[a_0^2 t_0^2 + \frac{\beta\left(\Delta - s\tau\lambda_I\right)}{4m_0}\right] + 2\tau t_0 t_1 a_0^3 k^3 \cos\left(3\phi_k\right)\Bigg\}^{1/2},\end{aligned}$$

with $\tan\phi_k = k_y/k_x$, we obtain the DOS in ML-MDS given by

$$D(E) = \sum_{s,\tau,\sigma=\pm 1}\int \frac{d^2k}{(2\pi)^2}\,\delta\left[E - E_{m,\sigma}^{\tau s}(\boldsymbol{k})\right]. \tag{6.1}$$

The sum in Eq. (6.1) runs over both valleys (τ), spins (s), and pseudospins (σ). In Fig. 6.1 the DOS is shown for electron and hole doping. While in the former both conduction bands are always filled for $\mu > \Delta/2$, in the latter either one,

$$-\frac{\Delta}{2} - \lambda_I < \mu < -\frac{\Delta}{2} + \lambda_I, \tag{6.2}$$

or two,

$$\mu < -\frac{\Delta}{2} - \lambda_I, \tag{6.3}$$

valence bands might be occupied.

In order to investigate the plasmon spectrum and the screening behavior, we need to calculate the DF in RPA [cf. Eq. (3.39)]:

$$\varepsilon(\boldsymbol{q},\omega) = 1 - \frac{e^2}{2\epsilon_0\epsilon_r q}\chi^0_{\rho\rho}(\boldsymbol{q},\omega).$$

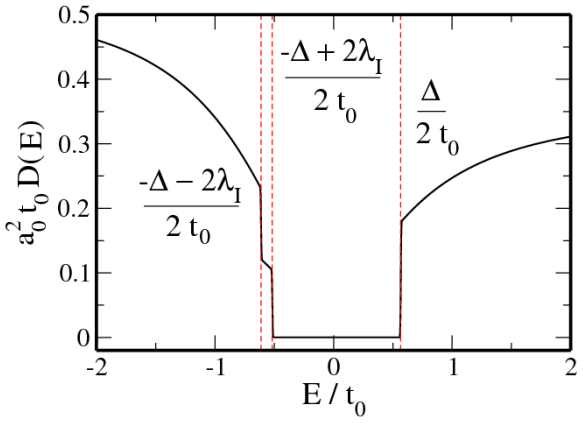

Figure 6.1.: DOS of ML-MDS. The dashed vertical lines show the upper (lower) boundaries of the valence (conduction) bands.

The background dielectric constant is chosen as $\epsilon_r = 5$ (comparable to the values in Refs. [114, 115]). As in the previous chapters, the free polarizability is a 2D integral in momentum space:

$$\chi^0_{\rho\rho}(\boldsymbol{q},\omega) = \sum_{s,\tau,\sigma,\sigma'=\pm1} \int \frac{d^2k}{(2\pi)^2} \left| \left\langle \xi^{\tau s}_{m,\sigma}(\boldsymbol{k}) \middle| \xi^{\tau s}_{m,\sigma'}(\boldsymbol{k}+\boldsymbol{q}) \right\rangle \right|^2 \times \\ \times \frac{f[E^{\tau s}_{m,\sigma}(\boldsymbol{k})] - f[E^{\tau s}_{m,\sigma'}(\boldsymbol{k}+\boldsymbol{q})]}{\omega - E^{\tau s}_{m,\sigma'}(\boldsymbol{k}+\boldsymbol{q}) + E^{\tau s}_{m,\sigma}(\boldsymbol{k}) + i0}, \tag{6.4}$$

where $\left|\xi^{\tau s}_{m,\sigma}(\boldsymbol{k})\right\rangle$ and $E^{\tau s}_{m,\sigma}(\boldsymbol{k})$ are the ML-MDS eigenstates and energies.[1] Notice that only one sum over s and τ, respectively, appears in Eq. (6.4) as spin and valley changing transitions are forbidden within our model. Assuming zero temperature for the rest of the chapter, the Fermi function $f[E]$ reduces to a simple step function.

If we neglect the contributions quadratic in momentum, i.e., setting $\alpha = \beta = t_1 = 0$ [corresponding to the model of Ref. [53] and Eq. (2.31)], the analytical solution for the isotropic free polarizability in Eq. (6.4) directly follows from

$$\chi^0_{\rho\rho}(q,\omega) = \sum_{s,\tau=\pm1} \chi^{0,s\tau}_{\rho\rho}(q,\omega), \tag{6.5}$$

where $\chi^{0,s\tau}_{\rho\rho}$ stands for the polarizability of gapped graphene given in Chaps. 4 and 5, with an effective spin- and valley-dependent mass term of

$$\tilde{\lambda}^{\tau s}_I = \frac{\Delta}{2} - \frac{s\tau\lambda_I}{2} \tag{6.6}$$

[1] While the (rather complicated) ML-MDS energies can be found in Eq. (2.28) in terms of a closed analytical expression, we do not present the analytical solution for the eigenvectors as the longish expressions are not very illuminating. For the calculation of the DF in the following, we will use the numerical solution for the eigensystem, obtained after diagonalization of $\hat{H}^{\tau s}_m$.

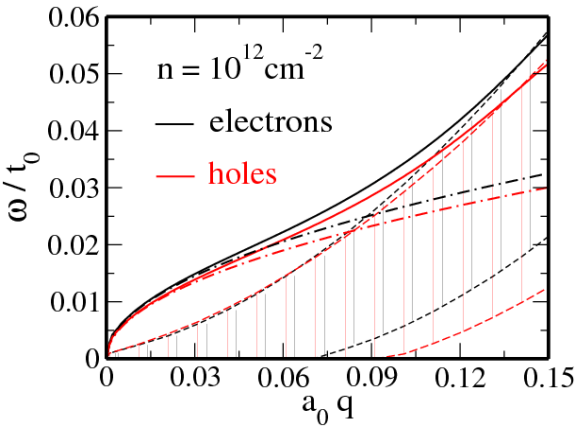

Figure 6.2.: The solid lines show the plasmon spectrum for an electron (black) and hole (red) concentration of $n = 10^{12}$ cm^{-2}. The dashed lines show the boundaries of the EHC. The dotted-dashed lines are the long-wavelength results of Eq. (6.8). The in-plane angle was set to $\phi_q = 0°$.

and a shifted Fermi energy

$$\tilde{\mu}^{\tau s} = \mu - \frac{s\tau\lambda_I}{2}. \tag{6.7}$$

However, in the following we do not neglect these terms as they were shown to be important even for low energies [54, 55], but rather solve $\varepsilon(\boldsymbol{q},\omega)$ within the extended model of Eq. (2.27). This is done numerically by first calculating the imaginary part of the polarizability as described in Sec. 3.1. Afterwards, the result is integrated with the help of the Kramers-Kronig relation in Eq. (3.9) to obtain the real part.

6.2. Collective charge excitations

Neglecting the trigonal warping term for the moment ($t_1 = 0$), we can readily derive an analytical formula for the plasmon dispersion from the general long-wavelength expression in Eq. (3.48) together with the solution for the energies in Eq. (2.28):

$$\omega^0_{q\pm} = \sqrt{\frac{e^2}{8\pi\epsilon_0\epsilon_r}\sum_{\tau,s=\pm1} k_{F\tau\cdot s}\left|\frac{\partial E^{\tau s}_{m,\pm}}{\partial k}\right|_{k=k_{F\tau\cdot s}}}\sqrt{q}. \tag{6.8}$$

The Fermi wave vector in ML-MDS is

$$k_{F\pm} = \frac{\sqrt{8}m_0a_0t_0}{\sqrt{\beta^2-\alpha^2}}\mathrm{Re}\left[\left\{-1-\frac{2\alpha\mu+\beta\Delta\mp(\alpha+\beta)\lambda_I}{4m_0a_0^2t_0^2}\right.\right.$$
$$\left.\left.+\left[\left(\beta^2-\alpha^2\right)\frac{(2\mu-\Delta)(2\mu+\Delta\mp2\lambda_I)}{16m_0^2a_0^4t_0^4}+\left(1+\frac{2\alpha\mu+\beta\Delta\mp(\alpha+\beta)\lambda_I}{4m_0a_0^2t_0^2}\right)^2\right]^{1/2}\right\}^{1/2}\right]. \tag{6.9}$$

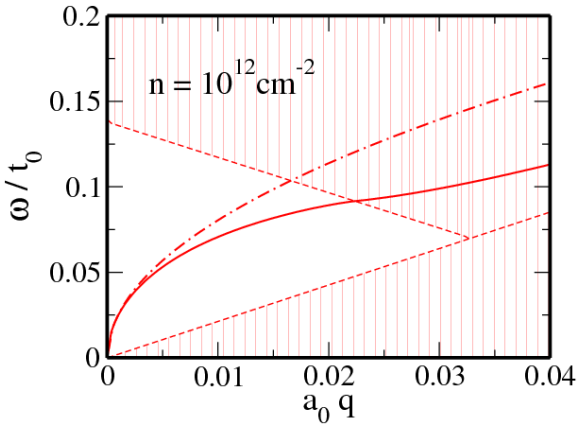

Figure 6.3.: Plasmon dispersion (solid line) and boundaries of the EHC (dashed) for graphene with $n = 10^{12}$ cm^{-2}. The dotted-dashed line shows the long-wavelength result $\omega_q^0 = \sqrt{e^2\mu q/2\pi\epsilon_0}$.

The upper (lower) sign in Eqs. (6.8) and (6.9) stands for the n-doped (p-doped) case. Due to the electron-hole symmetry in graphene, plasmons in n- and p-doped samples at a given carrier concentration show the same dynamics.[2] This is obviously no longer true in ML-MDS as the structure of the valence bands is quite different compared to the conduction bands; see Fig. 6.1.

In Fig. 6.2 the plasmon dispersion and the intraband part of the EHC are shown at a given carrier concentration of

$$n = \sum_{\nu=\pm 1} \frac{(k_{F\nu})^2}{2\pi} = 10^{12}\ \text{cm}^{-2} \tag{6.10}$$

for electron (black) and hole (red) doping. The in-plane angle orientation was set to $\phi_q = 0°$, where $\tan\phi_q = q_y/q_x$. The dotted-dashed lines show the long-wavelength result of Eq. (6.8), which turns out to be in good agreement with the numerical solution for $a_0 q \lesssim 0.05$. The plasmon dispersions and the EHC for n and p doping clearly differ, where ω_q is energetically higher in the former.

Due to the large value of the band gap, the interband part of the EHC in ML-MDS is energetically very high and, subsequently, the plasmon dispersion enters the intraband EHC. This is quite different compared to graphene, where due to the singularity of the free polarizability at $\omega = v_F q$ (with $v_F = 10^6$ m/s being the Fermi velocity in graphene), damping can only be caused by interband transitions [61]. Comparing Fig. 6.2 with the corresponding result obtained for suspended graphene in Fig. 6.3 (which is essentially Fig. 4.2(a) with rescaled axes), we can immediately see that the mode in graphene becomes damped at much smaller wave vectors $a_0 q \approx 0.02$ compared to ML-MDS, where damping appears not before $a_0 q \approx 0.15$. The ELF of graphene for such large momenta does not exhibit a resonant peak and thus the plasmon is already overdamped. However, the plasmon energies in graphene are clearly larger compared to ML-MDS: e.g., $\omega_q \approx 0.09 t_0$ in the former, while $\omega_q \approx 0.01 t_0$ in the latter; both at fixed $a_0 q = 0.02$. It is interesting to

[2] When we compare ML-MDS to graphene in this chapter, we use the natural values for the SOC parameters in graphene: $\lambda_I = 12$ μeV and $\lambda_R = 5$ μeV. Therefore, SOIs in graphene can be neglected for the moment.

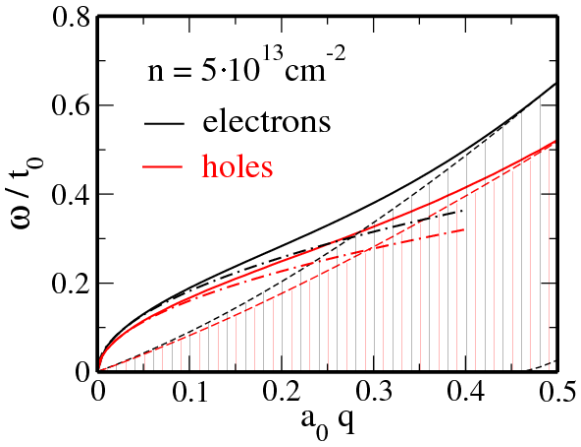

Figure 6.4.: The solid lines show the plasmon spectrum for an electron (black) and hole (red) concentration of $n = 5 \cdot 10^{13}$ cm^{-2}. The dashed lines show the boundaries of the EHC. The dotted-dashed lines are the long-wavelength results of Eq. (6.8). The in-plane angle was set to $\phi_q = 0°$.

note that while the long-wavelength plasmon energy in graphene [61],

$$\omega_q^0 = \sqrt{\frac{e^2 \mu q}{2\pi\epsilon_0}}, \tag{6.11}$$

see dotted-dashed line in Fig. 6.3, overestimates the exact solution, the approximate result of Eq. (6.8) is energetically below the numerical value.

The difference in the plasmon energies for n and p doping becomes enhanced for larger densities as the difference in the electron and hole masses becomes more important; see Fig. 6.4 for $n = 5 \cdot 10^{13}$ cm^{-2}. A detailed analysis of the dependence of the plasmon energies ω_q^2 on the carrier concentrations obtained for fixed momentum $a_0 q = 0.05$ and angle $\phi_q = 0°$ is shown in Fig. 6.5, clearly indicating that the asymmetry in the plasmon spectrum increases for larger densities.

From Fig. 6.5 one can furthermore see that the plasmon energy in ML-MDS is of the form

$$\omega_q \propto n^{1/2}, \tag{6.12}$$

as in a 2DEG [63]. This can be understood from the long-wavelength behavior of the plasmon frequency: Neglecting for simplicity terms quadratic in momentum in the Hamiltonian of Eq. (2.27) (which does not change the qualitative behavior),

$$\omega_q^0 = \sqrt{\frac{e^2 q}{2\pi\epsilon_0\epsilon_r}} \sqrt{\frac{(2\mu - \Delta)\left[\mu\left(\Delta + 2\mu\right) - \lambda_I^2\right]}{4\mu^2 - \lambda_I^2}}, \tag{6.13}$$

for realistic concentrations of $n = 10^{13}$ cm^{-2} the ratio $\Delta/2\mu \approx 0.97$ is close to unity and thus we can approximate Eq. (6.13) by ($\lambda_I \ll \Delta, \mu$)

$$\omega_q^0 \approx \sqrt{\frac{e^2 q}{2\pi\epsilon_0\epsilon_r}} \sqrt{\mu\left[1 - \frac{\Delta^2}{\Delta^2 + 4\pi t_0^2 a_0^2 n}\right]} \approx \sqrt{\frac{2e^2 q \mu t_0^2 a_0^2}{\epsilon_0\epsilon_r \Delta^2}} \sqrt{n}. \tag{6.14}$$

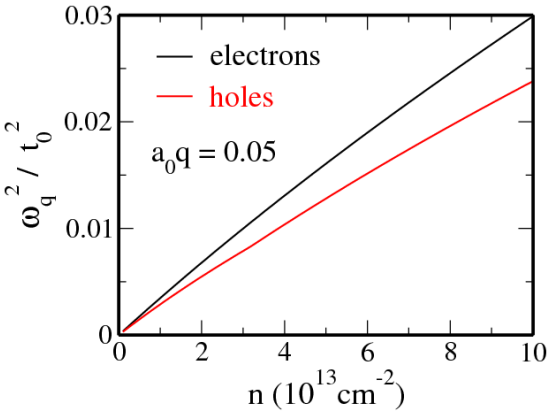

Figure 6.5.: Density dependence of the plasmon energy ω_q^2 for electron (black) and hole (red) doping. In both cases the spectrum clearly scales as $\omega_q \propto \sqrt{n}$. Parameters: $a_0 q = 0.05$, $\phi_q = 0°$.

Therefore, ML-MDS can be considered as a kind of a nonrelativistic limit of gapped graphene. In contrast, due to the ultrarelativistic nature of the charge carriers in graphene, the density dependence of the plasmon frequency

$$\omega_q^0 = \sqrt{\frac{e^2 \mu q}{2\pi\epsilon_0}} \tag{6.15}$$

scales as $\omega_q \propto n^{1/4}$ [62].

Let us finally comment on the importance of the terms in Eq. (2.27) that are quadratic in momentum. Due to the smallness of the trigonal warping contribution t_1, the plasmon spectrum turns out to be virtually isotropic and the angle dependence of ω_q is negligible. Comparing, for example, the ELF for $\phi_q = 0°$ and $\phi_q = 60°$ at a given momentum $a_0 q = 0.2$, we notice only a very small relative difference of a few percent in the plasmon energies even for large concentrations of $n = 5 \cdot 10^{13}$ cm^{-2}. However, our calculations also show that the other contributions proportional to α and β cannot be neglected. The energies ω_q obtained from the extended model in Eq. (2.27) turn out to be clearly enlarged with respect to the simplified model in Eq. (2.31), even for small momenta. For example, for $a_0 q = 0.05$ and an electron doping of $n = 10^{13}$ cm^{-2} the energy in the latter is $\omega_q \approx 0.04 t_0$, while $\omega_q \approx 0.06 t_0$ in the former. For even larger densities of $n = 5 \cdot 10^{13}$ cm^{-2}, we obtain $\omega_q \approx 0.09 t_0$ in the simplified model and $\omega_q \approx 0.13 t_0$ for the full model. Therefore, we conclude that the inclusion of the terms that are responsible for the different electron and hole masses is necessary to obtain quantitatively correct values for the plasmon energies.

6.3. Screening of impurities

Assuming the DF to be isotropic, i.e., neglecting the trigonal warping term, the RPA-improved Coulomb potential of a static impurity can be obtained from [91]

$$\Phi(r) = \frac{Q}{\epsilon_0 \epsilon_r} \int_0^\infty dq \, \frac{J_0(qr)}{\varepsilon(q,0)}. \tag{6.16}$$

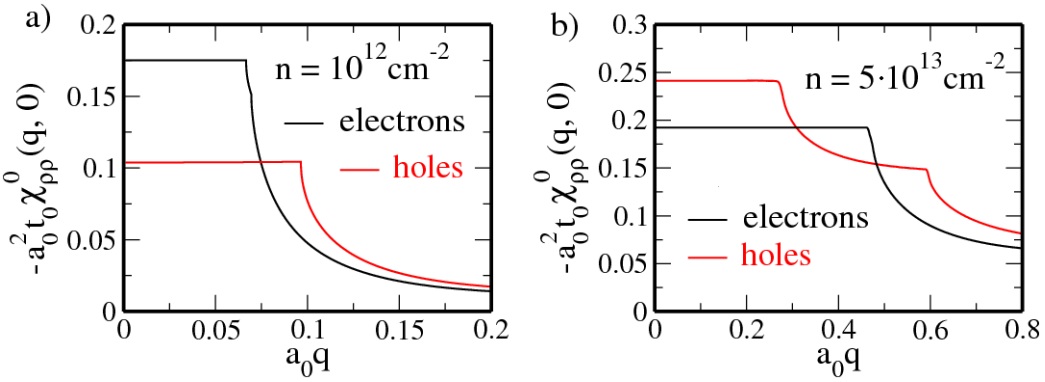

Figure 6.6.: Static polarizability for (a) $n = 10^{12}$ cm^{-2} and (b) $n = 5 \cdot 10^{13}$ cm^{-2} for electron (black) and hole (red) doping.

As in the Sec. 4.4, $J_0(x)$ is the Bessel function of the first kind and Q the charge of the impurity. From the Lighthill theorem [105] we know that the asymptotic behavior of $\Phi(r)$ is determined by the nonanalytical points of the DF. In the static polarizability cusps are expected to appear right at $q = 2k_{F\pm}$ indicating such singular points. While due to the absence of backscattering on the Fermi surface in doped graphene only the second derivative of the static DF diverges at $q = 2k_F$ [61, 106], see also black line in Fig. 5.2(c), already the first derivative does in an electron gas [63]. As a result, the power law dependence of the potential in graphene, $\Phi(r) \propto r^{-3}$, is quite different compared to $\Phi(r) \propto r^{-2}$ in a 2DEG. Nevertheless, in both cases the screened Coulomb potential exhibits characteristic sinusoidal Friedel oscillations due to the existence of a sharp Fermi surface.

In Fig. 6.6 we show the static polarizability of ML-MDS for two different charge carrier concentrations: $n = 10^{12}$ cm^{-2} and $n = 5 \cdot 10^{13}$ cm^{-2}. While in the former case

$$-\chi^{0,e}_{\rho\rho}(q \to 0, 0) > -\chi^{0,h}_{\rho\rho}(q \to 0, 0), \tag{6.17}$$

the opposite is true in the latter which can be understood from the DOS in Fig. 6.1. For hole densities of $n = 10^{12}$ cm^{-2} only one valence band is occupied. Therefore, only one Fermi wave vector is finite and the static polarizability is singular at $q = 2k_{F+}$; see red line in Fig. 6.6(a). In the other case of electron doping both conduction bands are filled and the Fermi contour consists of two concentric circles with different radii, where the relative difference between k_{F+} and k_{F-}, of about 5%, is only small. As a result, the screened potentials in Figs. 6.7(a) and (b) behave as

$$\Phi(r) \propto \frac{\sin(2k_{F+}r)}{(2k_{F+}r)^2} \tag{6.18}$$

for hole doping, while for the electronic case $\Phi(r)$ deviates slightly from this behavior due to an additional contribution proportional to $\sin(2k_{F-}r)/(2k_{F-}r)^2$.

The case of $n = 5 \cdot 10^{13}$cm^{-2} is more interesting as also in the p-doped case both valence

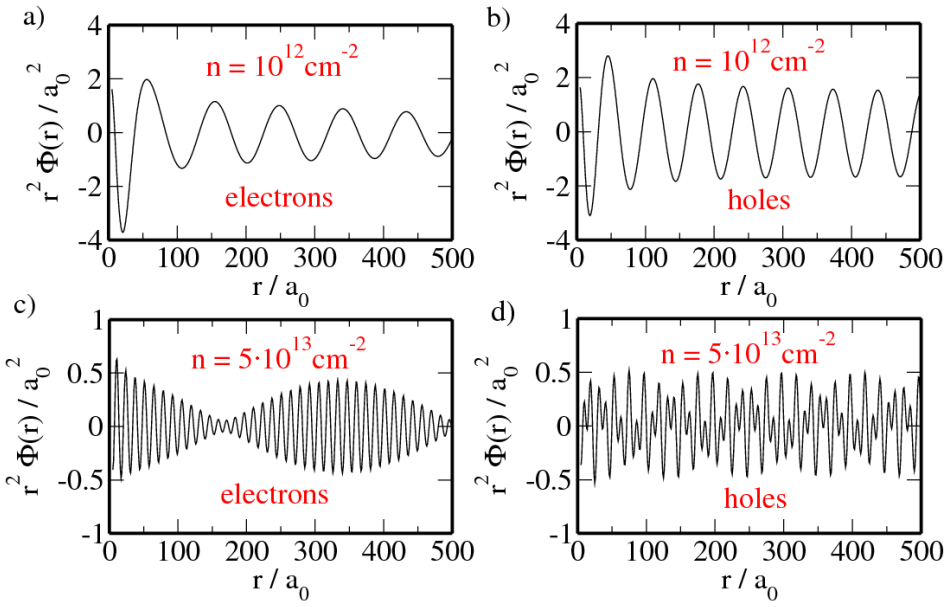

Figure 6.7.: Numerically calculated screened potential (in units of $Q/a_0\epsilon_0\epsilon_r$) for electron [(a) and (c)] and hole doping [(b) and (d)] for two different carrier concentrations $n = 10^{12}$ cm^{-2} and $n = 5 \cdot 10^{13}$ cm^{-2}, respectively.

bands are occupied and the corresponding wave vectors k_{F+} and k_{F-} differ significantly due to the large value of the SOC parameter; see red line in Fig. 6.6(b). The numerically calculated potentials $\Phi(r)$, as shown in Figs. 6.7(c) and (d), clearly show a superposition of two oscillatory contributions, whose periods are given by $1/2k_{F+}$ and $1/2k_{F-}$, respectively. This beating behavior is similarly to that of graphene if Rashba SOIs are taken into account. However, the important difference is that the intrinsic SOC parameter in ML-MDS of about 80 meV is naturally large compared to $\lambda_R = 5$ μeV (for 1 V/nm) in graphene and does not need to be enlarged by deliberate manipulation of the sample [41, 42] in order to see noticeable effects.

6.4. Summary

In conclusion, we have investigated the dynamical DF in a monolayer of MoS_2. As we have demonstrated, collective charge excitations in ML-MDS behave similarly to those in 2DEGs and clearly distinguish from graphene. The density dependence of the plasmon energies was shown to be of the form $\omega_q \propto n^{1/2}$, while $\omega_q \propto n^{1/4}$ in the carbon-based honeycomb lattice. Damping of plasmons in ML-MDS at large momenta is caused by the intraband transitions and not by interband processes. This leads to the existence of a resonance in the ELF of ML-MDS for momenta where the mode in graphene lies already in the EHC. Due to the pronounced electron-hole asymmetry in ML-MDS, a distinct difference in the plasmon dispersions of n- and p-doped samples is predicted. This difference was shown to increase for larger carrier concentrations as the difference in the electron

and hole masses becomes more important.

Based on the form of the static polarizability, one can expect the screened Coulomb potential to show a beating of Friedel oscillations for sufficiently large carrier concentrations due to the different curvature of the conduction and valence bands with opposite spin orientations. The numerical inspection of $\Phi(r)$ confirms the above prediction, where the period of this beating turns out to be roughly two orders of magnitude larger than the lattice constant.

Finally, it is important to note that these results might not only be relevant for ML-MDS, but also for other group-VI dichalcogenides. In Ref. [53], for example, it has been reported that the intrinsic SOC parameter could further be increased up to values of 215 meV if the molybdenum atoms are substituted by tungsten, which in turn would enhance the effects predicted in this chapter.

Chapter 7.

Plasmons in spin-orbit coupled two-dimensional hole gas systems

Parts of this chapter have been published in collaboration with Tobias Dollinger, Paul Wenk, Klaus Richter, and John Schliemann in Phys. Rev. B 87, 085321 (2013).

While the focus in the previous chapters was set on graphene and ML-MDS as representatives of a new class of truly 2D solids, we now turn to quasi 2D III-V semiconductors. In these bulk inversion asymmetric materials, SOC of the Dresselhaus type is always present. If the structure inversion symmetry is broken as well, e.g., by applying a suitable confinement potential, the Rashba SOC additionally appears. As has been shown in earlier works on 2DEGs, the interplay between both types of SOIs can lead to interesting physics [116] and particularly might be useful in view of plasmonics [64, 65].

Comparable studies in p-doped samples, however, turn out to be significantly more complicated due to the more complex nature of the charge carriers in the valence bands. Various authors discussed the dielectric properties of hole gases in three dimensions. In Ref. [117], for example, it has been demonstrated that plasmons in bulk p-doped GaAs behave quite differently compared to their electronic counterpart as their energies always lie in the EHC and hence plasmons are Landau damped even at long wavelengths. Moreover, in Ref. [88] the dynamical polarizability of Luttinger's model in three dimensions within the spherical approximation has been solved in terms of closed analytical expressions, predicting a distinct beating of Friedel oscillations in hole gases. Going from three to two dimensions increases the complexity of the problem further due to the appearance of a variety of subbands and makes analytical progress for realistic models very difficult, hence requiring a proper numerical treatment.

The aim of the present chapter is to discuss the plasmon spectrum of 2D hole gases, exemplified on GaAs and InAs QWs described within Luttinger's model extended to the two lowest subbands. Although this is interesting on its own, we explicitly take into account SOIs of the Dresselhaus and Rashba type which has, up to our best knowledge, not been done yet. Due to the nontrivial structure of the wave function in growth direction, the DF of a quasi 2D system comprises a form factor that contains information on the confinement potential as explained in Sec. 7.1. After the discussion of the lowest subbands

and the DOS of GaAs and InAs in Sec. 7.2, their plasmon dispersions are presented in Sec. 7.3. The energies of the collective charge excitations show a pronounced anisotropy for GaAs- and InAs-based systems being clearly stronger in the former. In GaAs this leads to a suppression of plasmons due to Landau damping in some orientations. We show that because of the large Rashba contribution in InAs, the lifetime of plasmons can be controlled by changing the electric field. This effect is potentially useful in a plasmon transistor [64, 65]. Finally, in Sec. 7.4 we conclude with a brief summary of the results.

7.1. The model

We describe GaAs and InAs by Luttinger's model [84] introduced in Chap. 2.3, including SOIs of the Dresselhaus type up to the third order in momentum (which indeed is the lowest order to describe the effect due to bulk inversion asymmetry) [89], and the Rashba contribution [90]:

$$\hat{H}_L = -\left[\hat{H}_{L,0} + \hat{H}_D + \hat{H}_R\right]. \tag{7.1}$$

Notice that the sign of $\hat{H}_L$ is inverted with respect to $\hat{H}_{L,0}$, $\hat{H}_D$, and $\hat{H}_R$ such that all valence band energies are positive in the following. To model a QW we assume a hard-wall confinement in the [001] direction. The eigensystem then follows from the infinite-dimensional matrix

$$\hat{H}_{QW} = \begin{pmatrix} \left\langle \varphi_1 | \hat{H}_L | \varphi_1 \right\rangle & \left\langle \varphi_1 | \hat{H}_L | \varphi_2 \right\rangle & \dots \\ \left\langle \varphi_2 | \hat{H}_L | \varphi_1 \right\rangle & \left\langle \varphi_2 | \hat{H}_L | \varphi_2 \right\rangle & \dots \\ \dots & \dots & \dots \end{pmatrix}, \tag{7.2}$$

where

$$\varphi_n(z) = \sqrt{\frac{2}{d}} \sin\left(\frac{n\pi z}{d}\right), \quad \text{with} \quad n \in \mathbb{N}, \tag{7.3}$$

are the subband functions and d the width of the QW.

In contrast to graphene or ML-MDS, the spatial dependence of the eigenstates in the growth direction of a QW is not delta-like but rather sinusoidal. Accordingly, the Fourier transform of the Coulomb potential

$$V(r) = \frac{e^2}{4\pi\epsilon_0\epsilon_r r}$$

is not

$$V(q) = \frac{e^2}{2\epsilon_0\epsilon_r q},$$

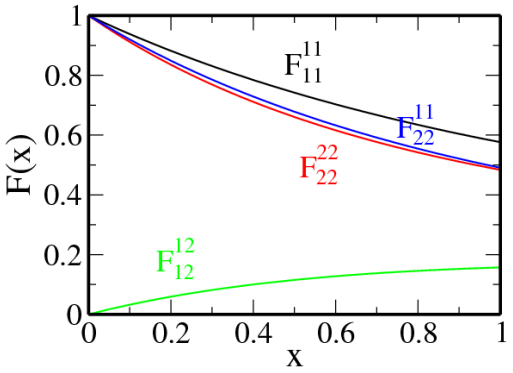

Figure 7.1.: Independent finite form factors $F^{n_1 n_3}_{n_2 n_4}$ as defined in Eqs. (7.5) and (7.6).

but contains a nontrivial function known as form factor.[1] While the DF in RPA keeps the well-known structure [see Eq. (3.39)]

$$\varepsilon(\boldsymbol{q},\omega) = 1 - \frac{e^2}{2\epsilon_0\epsilon_r q}\,\chi^0_{\rho\rho}(\boldsymbol{q},\omega),$$

the free polarizability becomes slightly more complicated:

$$\chi^0_{\rho\rho}(\boldsymbol{q},\omega) = \sum_{\lambda_1,\lambda_2}\int \frac{d^2k}{(2\pi)^2}\frac{f\left[E_{\lambda_1}(\boldsymbol{k})\right] - f\left[E_{\lambda_2}(\boldsymbol{k}+\boldsymbol{q})\right]}{\omega - E_{\lambda_2}\left(\boldsymbol{k}+\boldsymbol{q}\right) + E_{\lambda_1}\left(\boldsymbol{k}\right) + i0}\times$$
$$\times\left(\sum_{\substack{n_1,n_2,\\ n_3,n_4}}\left\langle \xi^{n_1}_{\lambda_1}\left(\boldsymbol{k}\right)\middle|\xi^{n_3}_{\lambda_2}\left(\boldsymbol{k}+\boldsymbol{q}\right)\right\rangle\left\langle \xi^{n_2}_{\lambda_2}\left(\boldsymbol{k}+\boldsymbol{q}\right)\middle|\xi^{n_4}_{\lambda_1}\left(\boldsymbol{k}\right)\right\rangle F^{n_1 n_3}_{n_2 n_4}(q)\right). \tag{7.4}$$

The above equation (7.4) contains a summation over all band indices λ_i and modes n_i ($i = 1,..,4$). E_{λ_i} are the subband energies and $|\xi^{n_i}_{\lambda_i}\rangle$ the n_i-th spinor components of the eigenstates in x-y direction. The momentum-dependent form factor $F^{n_1 n_3}_{n_2 n_4}(q)$ is defined as [91, 118]

$$F^{n_1 n_3}_{n_2 n_4}(q) = \int_0^d dz \int_0^d dz' \varphi^*_{n_1}(z)\varphi^*_{n_2}(z')\varphi_{n_3}(z)\varphi_{n_4}(z')e^{-|z-z'|q}. \tag{7.5}$$

Combining the above subband function in Eq. (7.3) with Eq. (7.5), the analytical solution of $F^{n_1 n_3}_{n_2 n_4}(q)$ reads [119, 120]:

$$F^{n_1 n_3}_{n_2 n_4}(x) = \frac{16 n_1 n_2 n_3 n_4 x^2\left\{\left[(-1)^{n_1+n_3} + (-1)^{n_2+n_4}\right]e^{-x} - (-1)^{n_1+n_2+n_3+n_4} - 1\right\}}{\pi^4\left[(n_2-n_4)^2 + \frac{x^2}{\pi^2}\right]\left[(n_2+n_4)^2 + \frac{x^2}{\pi^2}\right]\left[(n_1-n_3)^2 + \frac{x^2}{\pi^2}\right]\left[(n_1+n_3)^2 + \frac{x^2}{\pi^2}\right]}$$
$$+ \frac{x}{(n_2-n_4)^2\pi^2 + x^2}\left[\delta_{n_1-n_2,n_3-n_4} + \delta_{n_1+n_2,n_3+n_4} - \delta_{n_1-n_2,-n_3-n_4} - \delta_{n_1-n_2,-n_3+n_4}\right]$$
$$+ \frac{x}{(n_2+n_4)^2\pi^2 + x^2}\left[\delta_{n_1-n_2,-n_3+n_4} - \delta_{n_1+n_2,n_3-n_4} - \delta_{n_1-n_2,n_3+n_4}\right]. \tag{7.6}$$

[1] See App. 1 in Ref. [91] for further details on the form factor.

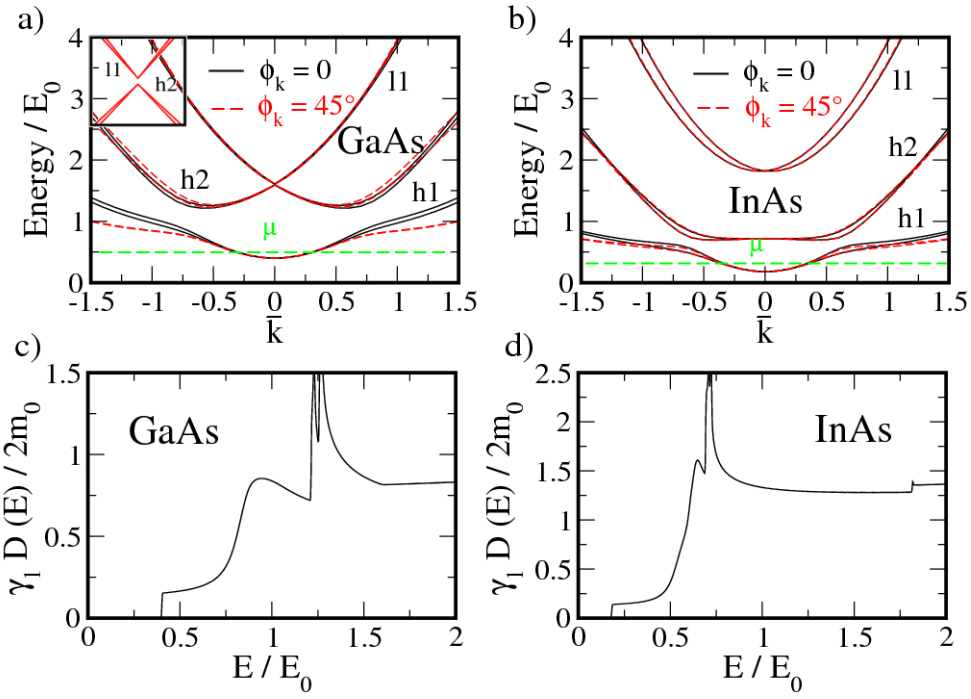

Figure 7.2.: Top: Energy spectrum of (a) GaAs and (b) InAs for two different orientations $\phi_k = 0°$ (solid black line) and $\phi_k = 45°$ (dashed red). The dashed green line indicates the position of the Fermi energy corresponding to a carrier density of $n = 5 \cdot 10^{10}$ cm^{-2}. The inset in (a) shows the energies E_{h2} and E_{l1} around the Γ point. Bottom: DOS of (c) GaAs and (d) InAs. In all cases, the electric field is set to $E_z = 1.5 \cdot 10^7$ V/m.

Due to symmetry of Eq. (7.5), one can immediately see that for the two lowest subbands out of the sixteen form factors $F^{n_1 n_3}_{n_2 n_4}(q)$ only six independent remain: e.g., F^{11}_{11}, F^{22}_{22}, F^{12}_{12}, F^{11}_{22}, F^{11}_{12}, and F^{12}_{22}. As the form factor is zero if $n_1 + n_2 + n_3 + n_4$ is odd [120], the latter two vanish. The remaining four finite contributions are shown in Fig. 7.1.

Note that as Luttinger's Hamiltonian is generally anisotropic, the DF will be a function of the magnitude of the momentum transfer q and the polar angle $\tan\phi_q = q_y/q_x$. As in the previous sections, we assume zero temperature such that the Fermi function reduces to a step function again.

7.2. Subband dispersion and density of states

Before we start with the discussion of the DF, we have a closer look on the energy spectrum and the DOS,

$$D(E) = \sum_\lambda \int \frac{d^2k}{(2\pi)^2}\, \delta\left[E - E_\lambda(\boldsymbol{k})\right], \tag{7.7}$$

of GaAs and InAs QWs with a thickness of $d = 20$ nm, an electric field of order 10^7 V/m, and a hole concentration of $n = 5 \cdot 10^{10}$ cm^{-2} [121]. We consider the two lowest subbands and neglect higher ones, as well as electronic and split-off bands. Our numerical inspection shows that the dominant contributions in the DF arise from the intraband and interband transitions with final states in the ground state light and heavy hole and in the first excited heavy hole bands. Already the inclusion of the first excited light hole states does not lead to significant changes in the plasmon spectrum. Therefore, the influence of energetically higher subbands or the electronic and split-off bands will be even smaller.

For convenience, we express all energies in terms of the size-quantization scale

$$E_0 = \frac{\gamma_1 \pi^2}{2 m_0 d^2}, \tag{7.8}$$

and use the notation that all wave vectors with a *bar* symbol have to be understood as dimensionless quantities measured in units of π/d; e.g., $\bar{q} = qd/\pi$. In Table 2.2 the band parameters of GaAs and InAs, together with the background dielectric constants ϵ_r and energies E_0 can be found.

7.2.1. GaAs

In Fig. 7.2(a) the six lowest bands of GaAs are shown for an electric field of $E_z = 1.5 \cdot 10^7$ V/m. The solid black (dashed red) curve shows an in-plane momentum angle orientation of $\phi_k = 0°$ (45°), where $\tan \phi_k = k_y/k_x$.

Neglecting the off-diagonal contributions in Eq. (7.2), the heavy and light hole energies of the n-th subband right at the Γ point can be approximated by [56]

$$E_{h/l,n}(0) = n^2 \left(1 \mp 2\frac{\gamma_2}{\gamma_1}\right) E_0. \tag{7.9}$$

While the lowest bands at $E_{h1}(0) = 0.38\, E_0$ are well separated from the others, the four next states, E_{h2} and E_{l1}, are very close to each other, though they do not touch which can be seen from the inset in Fig. 7.2(a). Therefore, in GaAs it is not sufficient to restrict ourselves to the ground state energies (E_{h1} and E_{l1}), but one also needs to take into account the first excited subbands E_{h2} [122].

We can see that the anisotropy of the heavy hole bands is clearly larger than that of the light holes. The Dresselhaus contribution leads to a spin-splitting of the bands. As the Rashba part in GaAs is virtually negligible for realistic fields [56], only minor changes occur in the spectrum once an electric field is turned on.

The DOS obtained from Eq. (7.7) is shown in Fig. 7.2(c). Due to quantization in the z direction, the DOS is zero for energies smaller than $E_{h1}(0)$. As the energy spectrum shows singular points at $E_{vH} \approx 1.25\, E_0$, see Fig. 7.2(a), we observe two nearby Van Hove singularities around E_{vH}. Without SOIs spin degeneracy is recovered and both singularities merge. Finally, for large enough energies, $E > 2\, E_0$, the DOS remains roughly constant as in a 2DEG.

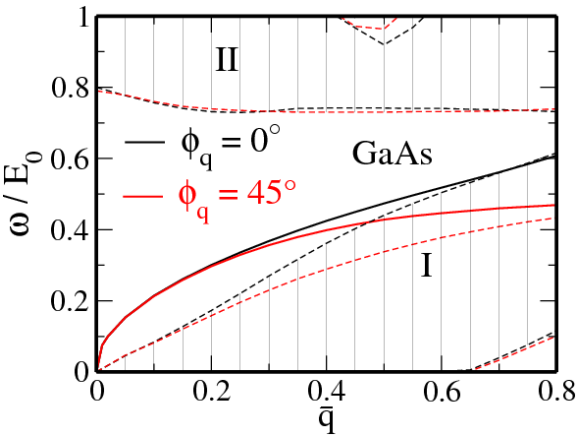

Figure 7.3.: The solid lines show the plasmon dispersion of GaAs for an angle orientation of $\phi_q = 0°$ (black) and $\phi_q = 45°$ (red). The dashed lines display the boundaries of the EHC for $\phi_q = 0°$ (black) and $\phi_q = 45°$ (red). The electric field is set to $E_z = 0$ and the hole density to $n = 5 \cdot 10^{10}$ cm^{-2}.

7.2.2. InAs

The numerically calculated energy spectrum of InAs, including a finite electric field of $E_z = 1.5 \cdot 10^7$ V/m, is shown in Fig. 7.2(b). Compared to GaAs the anisotropy in the spectrum of InAs is much weaker. As the anisotropic terms are proportional to $\gamma_2 - \gamma_3$ [see Eq. (2.42)], the reason for this is clearly the smaller relative difference of γ_2 and γ_3, roughly being 10 percent in InAs while in GaAs it is about 30 percent; see Table 2.2. Unlike GaAs the Rashba contribution now dominates over the Dresselhaus part and the spin-splitting of the bands is mainly caused by the former.

Another important difference between GaAs and InAs is that the Γ point energies of the first excited heavy hole states, $E_{h2} = 0.74\,E_0$, are much smaller than that of the ground state light hole bands at $E_{l1} = 1.81\,E_0$. Therefore, for the calculation of the DF the $n = 2$ subbands cannot be neglected as interband transitions with a final state in E_{h2} occur for smaller energy transfer than those ending in E_{l1}.

The DOS of InAs shows features similar to those of GaAs; see Fig. 7.2(d). That is, the DOS is zero for energies $E < E_{h1} = 0.17\,E_0$ and steps at E_{h1}, E_{h2}, and E_{l1} describe the sudden occupation of the valence bands. Furthermore, singular points in the derivative of the energy dispersion at $E \approx 0.70\,E_0$ and $E \approx E_{l1}$ give rise to characteristic spin-split Van Hove singularities.

7.3. Collective charge excitations

We now continue with the discussion of the collective charge excitations. As in the preceding chapters, in order to get the plasmon energies we search for the roots of Eq. (3.42),

$$\mathrm{Re}\,\{\varepsilon(\boldsymbol{q}, \omega_q)\} = 0,$$

and in a subsequent step verify that the ELF exhibits a resonance at that point.

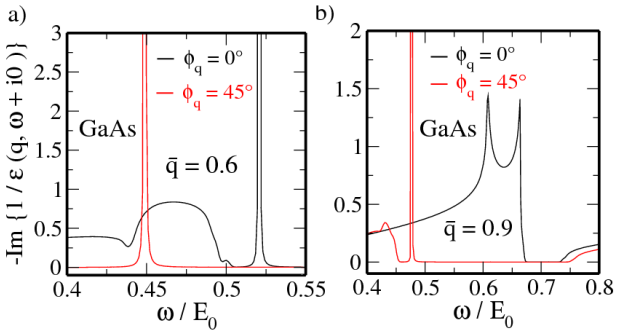

Figure 7.4.: ELF of GaAs for two different angle orientations, $\phi_q = 0°$ (black) and $\phi_q = 45°$ (red), and momenta (a) $\bar{q} = 0.6$ and (b) $\bar{q} = 0.9$. The electric field is set to $E_z = 0$ and the charge carrier concentration to $n = 5 \cdot 10^{10}$ cm^{-2}.

7.3.1. GaAs

In Fig. 7.3 we show the plasmon dispersion of a GaAs QW for two different in-plane angles $\phi_q = 0°$ (solid black line) and $\phi_q = 45°$ (solid red). As mentioned above, the hole density is set to $n = 5 \cdot 10^{10}$ cm^{-2} (corresponding to $\mu = 0.5\, E_0$); i.e., only the two lowest bands are occupied. The black and red dashed lines indicate the boundaries of the EHC in the respective orientation in order to see when plasmons acquire a finite lifetime. Region I is thereby caused by intraband transitions between the lowest lying valence bands (E_{h1}), while the interband continuum II is due to transitions with final bands E_{h2} and E_{l1}, respectively.

As can be seen from Fig. 7.3, the lower part of the EHC (region I) and the plasmon spectrum turn out to be clearly anisotropic. Moreover, the $\phi_q = 0°$ mode becomes damped at smaller wave vectors compared to the $\phi_q = 45°$ solution. To see this, the ELF is plotted in Fig. 7.4. For $\bar{q} = 0.6$, in both cases distinct peaks occur in the ELF indicating truly coherent modes. For larger wave vector, $\bar{q} = 0.9$ in Fig. 7.4(b), the peak is smeared out in the $\phi_q = 0°$ direction, i.e., the mode is damped, while for $\phi_q = 45°$ it remains delta-like.

In Fig. 7.5 the angle dependence of the plasmon energy and imaginary part of the DF are shown for fixed $\bar{q} = 0.8$. The energy (solid line) is redshifted for larger angles, up to a minimal value at $\phi_q = 45°$. The relative difference between the $\phi_q = 0°$ and $\phi_q = 45°$ energies is roughly 30 percent and thus of order of the difference of the hole gas parameters γ_2 and γ_3. The dashed line in the plot shows the imaginary part of the DF, which in turn

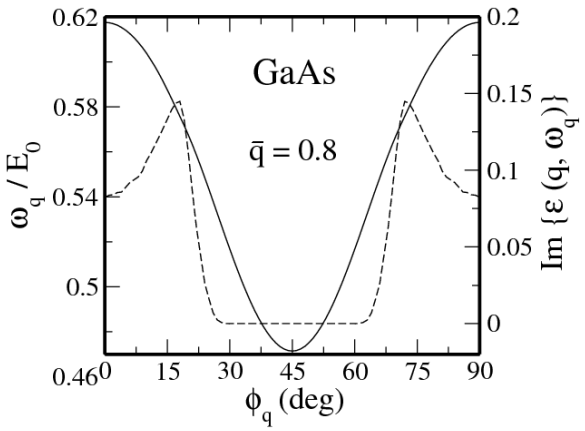

Figure 7.5.: Angle dependence of the plasmon energy (solid line) and imaginary part of the DF (dashed line) for GaAs with fixed $\bar{q} = 0.8$. The electric field is set to $E_z = 0$ and the charge carrier concentration to $n = 5 \cdot 10^{10}$cm^{-2}.

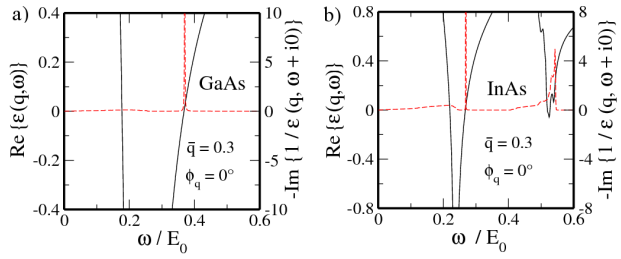

Figure 7.6.: (a) Real part of the DF (solid black) and ELF (dashed red) of GaAs. (b) The same for InAs. Parameters: $\bar{q} = 0.3$, $\phi_q = 0°$, $E_z = 0$, and $n = 5 \cdot 10^{10}$ cm^{-2}.

is related to the quasiparticle lifetime. For $\phi_q \leq 29°$ the damping rate is finite with a maximal value around $\phi_q = 18°$. For $30° \leq \phi_q \leq 45°$ the imaginary part vanishes and the peak in the ELF becomes sharp.

It should also be emphasized that for a given momentum, Eq. (3.42) yields an additional solution with smaller energy. However, this solution does not fulfill the original condition of Eq. (3.40) as the imaginary part of the DF at that point is not negligible. In Fig. 7.6(a) the real part of the DF (solid black) and the ELF (dashed red) are exemplarily shown for fixed $\bar{q} = 0.3$. From the latter we can see that only one resonance occurs and hence the additionally found solution is physically irrelevant.

7.3.2. InAs

So far we have seen that plasmons in GaAs-based 2D hole systems show a pronounced anisotropy as manifested in the plasmon spectrum and damping rate. Unfortunately, as the Rashba contribution in GaAs is virtually negligible, there is no direct control of this feature, e.g., by turning on/off the anisotropy dynamically by varying an electric field. However, this control is necessary for possible applications such as a plasmon filter or a plasmon transistor [64, 65]. On the other hand, as we know that in InAs the Rashba parameter and its influence on the energy spectrum is large, we expect SOC to give the possibility to modulate the plasmon spectrum somehow. In principle, one might also use materials with an even larger Rashba coupling such as InSb. However, the reason we focus on the former is twofold: First of all, in experiments InAs is more popular than InSb and, secondly, the four-band Luttinger Hamiltonian used in this chapter is not sufficient to describe InSb where the more advanced Kane model including electronic conduction bands and split-off bands needs to be used [86].

In Fig. 7.7 the plasmon energy and the EHC of InAs without an electric field are shown for $\phi_q = 0°$ (solid black) and $\phi_q = 45°$ (solid red). As before, the carrier concentration is $n = 5 \cdot 10^{10}$ cm^{-2}, corresponding to $\mu = 0.3\, E_0$. Region I marks transitions with initial and final states in E_{h1}, while in region II the final state is E_{h2}. Not shown in the plot is the interband continuum with final states in E_{l1} and E_{l2}, respectively. The anisotropy in the plasmon spectrum is less pronounced than in GaAs and the EHC is only weakly direction-dependent, where the main anisotropy arises in the intraband part. Contrary to GaAs, the two plasmon modes enter the continuum at almost equally large momenta $\bar{q} \approx 0.45$.

Up to now, spin-splitting of the energy bands is only caused by the Dresselhaus term. The effect of an increasing electric field, pointing along the growth direction, is demon-

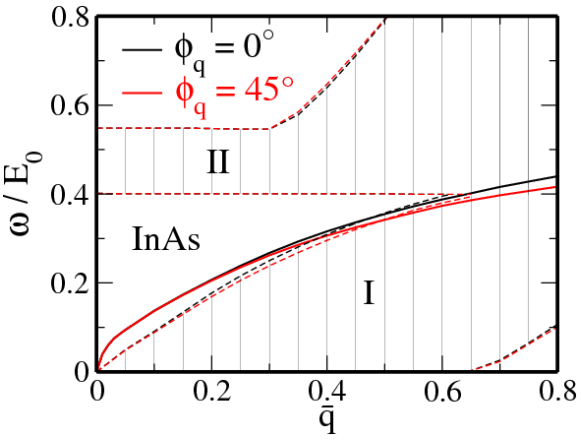

Figure 7.7.: The solid lines show the plasmon dispersion of InAs for an angle orientation of $\phi_q = 0°$ (black) and $\phi_q = 45°$ (red). The dashed lines display the boundaries of the EHC for $\phi_q = 0°$ (black) and $\phi_q = 45°$ (red). The electric field is set to $E_z = 0$ and the hole density to $n = 5 \cdot 10^{10}$ cm^{-2}.

strated in Fig. 7.8 for fixed momentum $\bar{q} = 0.3$ and two different directions $\phi_q = 0°$ and $\phi_q = 45°$. The delta-like peak in the case without applied electric field becomes broadened for large enough E_z, because both the intra- and interband continua expand due to the enhanced spin-splitting. If the interband EHC is sufficiently broad, it finally contains the point of the resonant energy ω_q. The detailed field dependence of the plasmon energy and lifetime is shown in Fig. 7.9. The energy (solid line) is blueshifted once the electric field is enlarged whereas the difference between the $E_z = 0$ and $E_z = 3.0 \cdot 10^7$ V/m result is about 15 percent.

More important than the position of the peak is its width, which in turn is related to the imaginary part of the DF (dashed lines). For $\phi_q = 0°$ the mode remains undamped if $E_z \lesssim 1.0 \cdot 10^7$ V/m. For larger fields the quasiparticles acquire a finite lifetime as $\mathrm{Im}\{\varepsilon(\boldsymbol{q}, \omega_q)\}$ is nonzero. Qualitatively the same features can be seen for $\phi_q = 45°$. However, the important point is that the critical field at which the mode enters the EHC, $E_z \approx 1.9 \cdot 10^7$ V/m, is now much larger. This in turn yields two possible applications: First, in a plasmon transistor excitations in the source can be detected in the drain, depending on their lifetime and thus on the strength of the applied electric field [64]. Second, changing the electric field in the range of $1.0 \cdot 10^7$ V/m $< E_z < 1.9 \cdot 10^7$ V/m allows for plasmon filtering since particular directions are damped while others are not [65].

Finally, we want to remark that as in GaAs, additional solutions of the approximate equation (3.42) can be found in InAs. However, as can be seen in Fig. 7.6(b), only one of

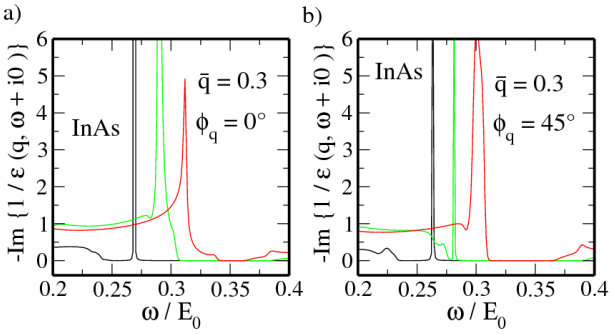

Figure 7.8.: ELF of InAs for fixed $\bar{q} = 0.3$ and various electric fields $E_z = 0$ (black), $1.8 \cdot 10^7$ V/m (green) and $2.8 \cdot 10^7$ V/m (red) for two different angle orientations (a) $\phi_q = 0°$ and (b) 45°. The hole density is set to $n = 5 \cdot 10^{10}$cm^{-2}.

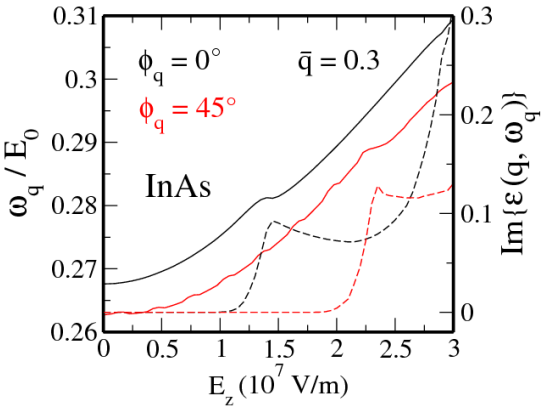

Figure 7.9.: Electric field dependence of the plasmon energy ω_q (solid lines) and lifetime being proportional to the imaginary part of the DF (dashed line) for two different angle orientations $\phi_q = 0°$ (black) and $\phi_q = 45°$ (red). Parameters: $n = 5 \cdot 10^{10}$ cm^{-2} and $\bar{q} = 0.3$.

these solutions corresponds to a genuine plasmonic mode with a characteristic resonance in the ELF.

7.4. Summary

In summary, we have investigated the DF of GaAs and InAs QWs within the four-band Luttinger Hamiltonian extended to the two lowest subbands, including SOIs of the lowest order Dresselhaus and Rashba type. For GaAs a pronounced anisotropy in the plasmon spectrum and in the EHC can be seen. Depending on the direction of the external field, plasmons are either damped or long-lived. This opens, in principle, the possibility of filtering plasmons with distinct orientations. However, the main problem in GaAs is the disability of controlling this feature due to the negligible Rashba contribution. Here, InAs seems to be more promising.

We have shown that while long-wavelength plasmons in InAs do not decay if the Rashba contribution is small enough, the lifetime of the plasmons can be modulated by changing the electric field. Furthermore, we have demonstrated that the critical field at which a finite damping occurs is direction-dependent. These features might be interesting for applications such as plasmon transistors [64] or plasmon filters [65].

Let us stress that for an experimental realization of a plasmonic circuit, the effects described in this chapter probably need to be enhanced further. Although this study is based on realistic standard band parameters, the strength of the SOC contributions can be enlarged beyond that values by applying strain to the sample or using more advanced heterostructures [56]. The numerical code used in this chapter is not limited to GaAs or InAs, but can also be applied to more complicated compounds provided their single-particle description is known.

Chapter 8.

8 Interplay between spin-orbit interactions and a time-dependent electromagnetic field in graphene

Parts of this chapter have been published in collaboration with Alexander López and John Schliemann in Phys. Rev. B 88, 045118 (2013).

Up to now, we have discussed the responses of graphene, ML-MDS, and III-V semiconductor QWs to a weak electromagnetic potential. The systems were assumed to remain in thermal equilibrium in the presence of the probing field and the single-particle properties directly followed from the time-independent Schrödinger equation. In the present chapter we will investigate the influence of a strong time-dependent field with an energy in the THz regime on a monolayer of graphene, taking explicitly into account SOIs of the intrinsic and Rashba type. Our interest is motivated by a number of recent publications, demonstrating that the THz field can lead to significant changes in the energy spectrum and transport characteristics of various 2D materials. For example, in Refs. [66, 67] it has been shown that an electromagnetic field can induce a band gap in graphene and even move and merge the Dirac points [123], or Ref. [124] where the possibility of changing the topology of a HgTe/CdTe QW by applying linearly polarized light, leading to so-called Floquet topological insulators, has been reported.

We begin with a brief summary of Floquet's theory in Sec. 8.1. In Sec. 8.2 the energy spectrum and the DOS of irradiated graphene is discussed and signatures arising from the interplay of SOIs and the THz field are pointed out. It turns out that the field can be used not only to induce a gap in the energy spectrum, but also to close an existing gap due to the different reaction of the spin components with circularly polarized light. The dynamics of physical observables such as the spin polarization and the position operators is the subject of Sec. 8.3. It is shown that the time evolution of the spin polarization and the orbital dynamics of an initial wave packet can be modulated by varying the ratio of the Rashba and intrinsic SOC parameters. Assuming that the system acquires a quasi-stationary state, the optical conductivity of the irradiated sample is calculated in Sec. 8.4. In contrast to the static case, the optical conductivity shows a multistep structure as dis-

cussed previously in Ref. [68], where the number of intermediate steps can be changed by adjusting the SOC parameters, the field amplitude, and field orientation. In Sec. 8.5 we finally summarize the main results of this chapter.

8.1. The model

We use the KMM of Eq. (2.21),

$$\hat{H}_g^\tau = v_F \boldsymbol{k}\cdot\hat{\boldsymbol{\sigma}}_\tau + \tau\lambda_I\hat{\sigma}_z\hat{s}_z + \lambda_R\left(\tau\hat{\sigma}_x\hat{s}_y - \hat{\sigma}_y\hat{s}_x\right)$$

to describe graphene including SOIs of the intrinsic and Rashba type. In the following we concentrate on $\tau = +1$ as analogous results might be obtained for the other K point. The effect of an electromagnetic field can be incorporated by the minimal coupling scheme

$$\boldsymbol{k} \to \boldsymbol{k} + e\boldsymbol{A}(t). \tag{8.1}$$

As the vector potential does not depend on the position operators, the Hamiltonian remains diagonal in momentum space and we can treat $\boldsymbol{k}$ as a number instead of a differential operator. The time-dependent contribution to the Hamiltonian,

$$\hat{H}_1(t) = ev_F\boldsymbol{A}(t)\cdot\hat{\boldsymbol{\sigma}}, \tag{8.2}$$

is assumed to be periodic in time, i.e.,

$$\hat{H}_1(t+T) = \hat{H}_1(t), \tag{8.3}$$

where $T = 2\pi/\Omega$ and Ω is the frequency of the radiation field.

The vector potential of a monochromatic wave can be assumed to be either classical,

$$\boldsymbol{A}(t) = \frac{\sqrt{2}E_0}{\Omega}\left[\cos\theta_p\cos\Omega t\ \boldsymbol{e}_x + \sin\theta_p\sin\Omega t\ \boldsymbol{e}_y\right], \tag{8.4}$$

or quantized,

$$\boldsymbol{A}(t) = \mathcal{A}\left[\cos\theta_p\left(\hat{a}e^{-i\Omega t} + \hat{a}^\dagger e^{i\Omega t}\right)\ \boldsymbol{e}_x + i\sin\theta_p\left(\hat{a}e^{-i\Omega t} - \hat{a}^\dagger e^{i\Omega t}\right)\ \boldsymbol{e}_y\right], \tag{8.5}$$

where, among obvious notation, the parameter $\mathcal{A}$ contains geometric information about the cavity surrounding the system and $\boldsymbol{e}_x$ ($\boldsymbol{e}_y$) is the unit vector in x (y) direction. The field is either circularly ($\theta_p = 45°$) or linearly polarized, e.g., along the x direction for $\theta_p = 0°$. Quantizing the electromagnetic field adds a degree of freedom described by the bosonic operators $\hat{a}^{(\dagger)}$, which comes along with a new conserved quantity given by the helicity

$$\hat{h} = \hat{J} + \hat{a}^\dagger\hat{a}, \tag{8.6}$$

where the angular momentum

$$\hat{J} = xk_y - yk_x + \frac{\hat{\sigma}_z}{2} \tag{8.7}$$

generates rotations of the carrier degrees of freedom in real and pseudospin space. To treat the electromagnetic field as a quantized operator is important in situations where the charge carriers have a significant back-action on the field, which in turn can alter the particle dynamics itself.

To analyze this aspect further, let us consider the case of a vanishing field and neglect SOIs for the moment. Now assuming a wave packet with initial momentum along the y axis and the pseudospin initially in the x direction, the dynamics of the system in the Heisenberg representation is given by [125, 126, 127, 128]

$$\frac{d^2}{dt^2} x_H(t) = -2v_F^2 k \sin(2v_F k t) \tag{8.8}$$

and

$$\frac{d^2}{dt^2} y_H(t) = 0. \tag{8.9}$$

From the classical expression for the radiative power of dipolar radiation [129],

$$P = \frac{e^2 \ddot{\boldsymbol{r}}^2}{6\pi\epsilon_0 c^3}, \tag{8.10}$$

we find the time-averaged energy loss per time as

$$\bar{P} = \frac{e^2 v_F^4 k^2}{3\pi\epsilon_0 c^3} \approx 7.12 \cdot 10^{-2} \, \frac{k^2}{\mathrm{nm}^{-2}} \frac{\mathrm{meV}}{\mathrm{ps}}. \tag{8.11}$$

For a wave vector of $k = 0.1\ \mathrm{nm}^{-1}$ the radiative power is of order 10^{-4} meV/ps. Due to the very large Fermi velocity of $v_F = 10^6$ m/s in graphene, a time scale of 1 ps corresponds to a distance of 1 μm traveled by the wave packet. Therefore, the above loss rate should be seen as a small effect and the energy loss due to dipolar radiation induced by *Zitterbewegung* can be neglected compared to other energy scales in typical experimental situations.[1] Accordingly, in what follows we will treat the electromagnetic field as a classical quantity and not as an operator.

Due to the periodicity of

$$\hat{H}_{ir}(t) = \hat{H}_g^+ + \hat{H}_1(t), \tag{8.12}$$

[1] It is instructive to compare this result with the situation of *Zitterbewegung* in a 2DEG with SOC of, say, the Rashba type. Here, the Hamiltonian reads $\hat{H}_R = \boldsymbol{k}^2/2m + \alpha\,[k_x\sigma_y - k_y\sigma_x]$, where m is an effective band mass, and the Rashba parameter α is of order 10^{-11} eVm. Performing steps analogous to those above, it is easy to see that the radiative power here is given by Eq. (8.11) when v_F is replaced with (reintroducing $\hbar$ for the moment) $\alpha/\hbar \approx 1.5 \times 10^4$m/s and hence $\bar{P}_{2DEG}/\bar{P}_{gr} = (\alpha/\hbar v_F)^4 \approx 5 \cdot 10^{-8}$. The energy loss due to the dipolar radiation in a 2DEG is several orders of magnitude smaller than in graphene and thus a vanishingly small effect.

the solution of Schrödinger's equation

$$\left[i\frac{\partial}{\partial t} - \hat{H}_{ir}(t)\right]|\Psi_{\boldsymbol{k},\mu\nu}\rangle = 0 \tag{8.13}$$

obeys Floquet's theorem [130, 131] and thus is of the form

$$|\Psi_{\boldsymbol{k},\mu\nu}(t)\rangle = e^{-i\varepsilon_{\boldsymbol{k},\mu\nu}t}\,|\psi_{\boldsymbol{k},\mu\nu}(t)\rangle\,, \tag{8.14}$$

where $\mu,\nu = \pm 1$ are band indices. The Floquet states $|\psi_{\boldsymbol{k},\mu\nu}(t)\rangle$ have the same periodicity as the Hamiltonian and can be expanded in a Fourier series [132]:

$$|\psi_{\boldsymbol{k},\mu\nu}(t)\rangle = \sum_{n=-\infty}^{\infty} e^{in\Omega t}\left|\xi^n_{\boldsymbol{k},\mu\nu}\right\rangle. \tag{8.15}$$

The original problem can now be reduced to the diagonalization of the time-independent Floquet Hamiltonian whose components are defined by

$$\left(\hat{H}_F\right)_{nm} = \frac{1}{T}\int_0^T dt\,\hat{H}_{ir}(t)e^{i(n-m)\Omega t} - n\Omega\delta_{nm}. \tag{8.16}$$

The time evolution of an arbitrary state with respect to an initial time t_0 is captured by the operator

$$\hat{U}_{\boldsymbol{k}}(t,t_0) = \sum_{\mu',\nu'=\pm 1} e^{-i\varepsilon_{\boldsymbol{k},\mu'\nu'}(t-t_0)}\,|\psi_{\boldsymbol{k},\mu'\nu'}(t)\rangle\,\langle\psi_{\boldsymbol{k},\mu'\nu'}(t_0)|\,. \tag{8.17}$$

Notice that the energies and wave functions entering Eq. (8.14) are not uniquely defined as

$$\left|\Psi^n_{\boldsymbol{k},\mu\nu}(t)\right\rangle = e^{in\Omega t}\,|\Psi_{\boldsymbol{k},\mu\nu}(t)\rangle\,, \quad \text{with} \quad n\in\mathbb{Z}, \tag{8.18}$$

is a solution of Schrödinger's equation as well. The corresponding quasienergies,

$$\varepsilon^n_{\boldsymbol{k},\mu\nu} = \varepsilon_{\boldsymbol{k},\mu\nu} + n\Omega, \tag{8.19}$$

differ only by a multiple of the field energy. Therefore, the choice of the eigenenergies is ambiguous as they describe the same physical situation. In order to get a well-defined quantity that is the same for all $\varepsilon^n_{\boldsymbol{k},\mu\nu}$, we introduce the mean (or quasistationary) energy [68, 133, 134, 135]

$$\begin{aligned}\bar{\varepsilon}_{\boldsymbol{k},\mu\nu} &= \frac{1}{T}\int_0^T dt\left\langle\Psi_{\boldsymbol{k},\mu\nu}(t)|\hat{H}_{ir}(t)|\Psi_{\boldsymbol{k},\mu\nu}(t)\right\rangle \\ &= \varepsilon_{\boldsymbol{k},\mu\nu} - \Omega\sum_{n=-\infty}^{\infty} n\left\langle\xi^n_{\boldsymbol{k},\mu\nu}\middle|\xi^n_{\boldsymbol{k},\mu\nu}\right\rangle.\end{aligned} \tag{8.20}$$

In general, there is a nontrivial relation between the quasienergies and the mean energies. Notice that in the absence of the driving Eq. (8.20) reproduces the energies of the

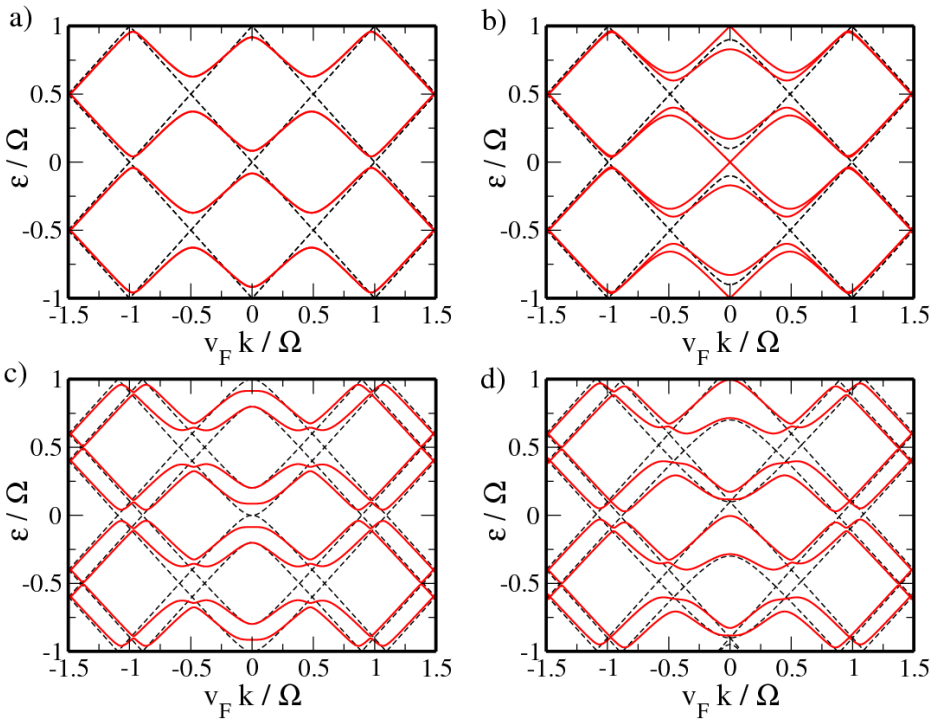

Figure 8.1.: Quasienergy spectrum of graphene under circularly polarized light ($\theta_p = 45°$) for various combinations of the SOC parameters: $(\lambda_R/\Omega, \lambda_I/\Omega)$ = (a) $(0, 0)$, (b) $(0, 0.1)$, (c) $(0.1, 0)$, and (d) $(0.1, 0.1)$. The field strength was set to $\alpha = 0.3$.

unperturbed system given in Eq. (2.22).

8.2. Energy spectrum and density of states

In most cases, the time-dependent Schrödinger equation (8.13) cannot be solved by closed analytical expressions, requiring solution strategies based on perturbation theory or numerics. For sufficiently small driving amplitudes and for wave vectors close to the resonant points $v_F k \approx \pm 0.5\Omega$, reasonable results can be obtained from the Rotating Wave Approximation [130, 136]. An analytical treatment is also possible within the Magnus-Floquet approach, where the wave function is expressed in a perturbative series of the field amplitude. However, using the Magnus expansion requires special attention regarding the convergence of the series as discussed in Refs. [137, 138, 139].

In this chapter we will concentrate on the numerical solution of the eigensystem by diagonalization of the time-independent Floquet Hamiltonian in Eq. (8.16). This leads to an infinite number of eigenenergies and states [132], where only four of them are physically independent (corresponding to the dimension of the problem), while all others follow from Eq. (8.19).

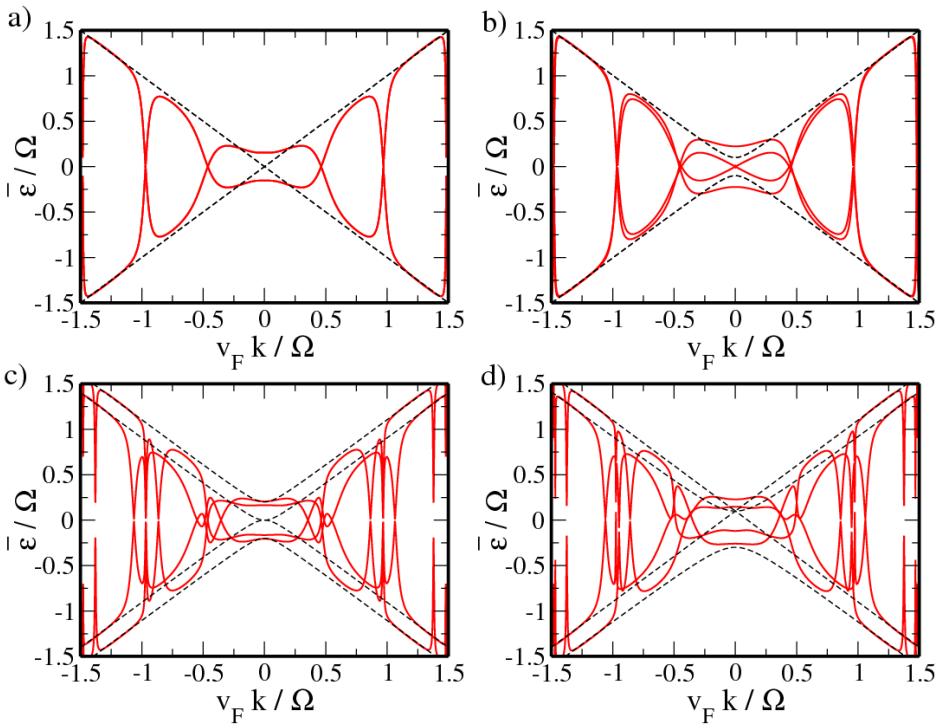

Figure 8.2.: Mean energies of graphene under circularly polarized light ($\theta_p = 45°$) for various combinations of the SOC parameters: $(\lambda_R/\Omega, \lambda_I/\Omega)$ = (a) $(0, 0)$, (b) $(0, 0.1)$, (c) $(0.1, 0)$, and (d) $(0.1, 0.1)$. The field strength was set to $\alpha = 0.3$.

8.2.1. Energy bands

In Figs. 8.1 and 8.3 the quasienergies within the first and second time Brillouin zones[2] (TBZs) are shown as red lines for different combinations of the SOC parameters for a fixed field strength of $\alpha = v_F e E_0/\Omega^2 = 0.3$. The black dashed lines show, for comparison, Eq. (2.22) projected to the TBZ. The SOC parameters are chosen to be of the order of the THz energy; in the present case $\lambda_{R(I)} \sim 0.1\Omega$. Our results depend only on the ratio $\lambda_{R(I)}/\Omega$ and on the coupling strength α. Therefore, they may also be applied to fields with larger frequencies (such as the mid-infrared), provided the SOC parameters are large enough. The advantage of a THz field, however, is that the field energies are far below the energies of optical phonons (of about 200 meV) [27], such that excitations of optical phonons are suppressed.

Circular polarization. The unperturbed energy spectrum of Eq. (2.22) consists of twofold spin-degenerate bands if $\lambda_R = 0$, while for a finite Rashba coefficient structure inversion symmetry is broken and the bands split up; see the dashed lines in Fig. 8.1. Once $\hat{H}_1(t)$ is turned on, in Figs. 8.1(a), (c), and (d) a gap opens up right the Dirac point, separating the valence and conduction bands. Here, the bands are parabolic around the K point but closely follow the linear behavior of the unperturbed result for $v_F k \gtrsim \Omega$. A finite gap also

[2]By analogy with the *ordinary* (spatial) first BZ, the first TBZ is defined as $|\varepsilon| \leq 0.5\Omega$.

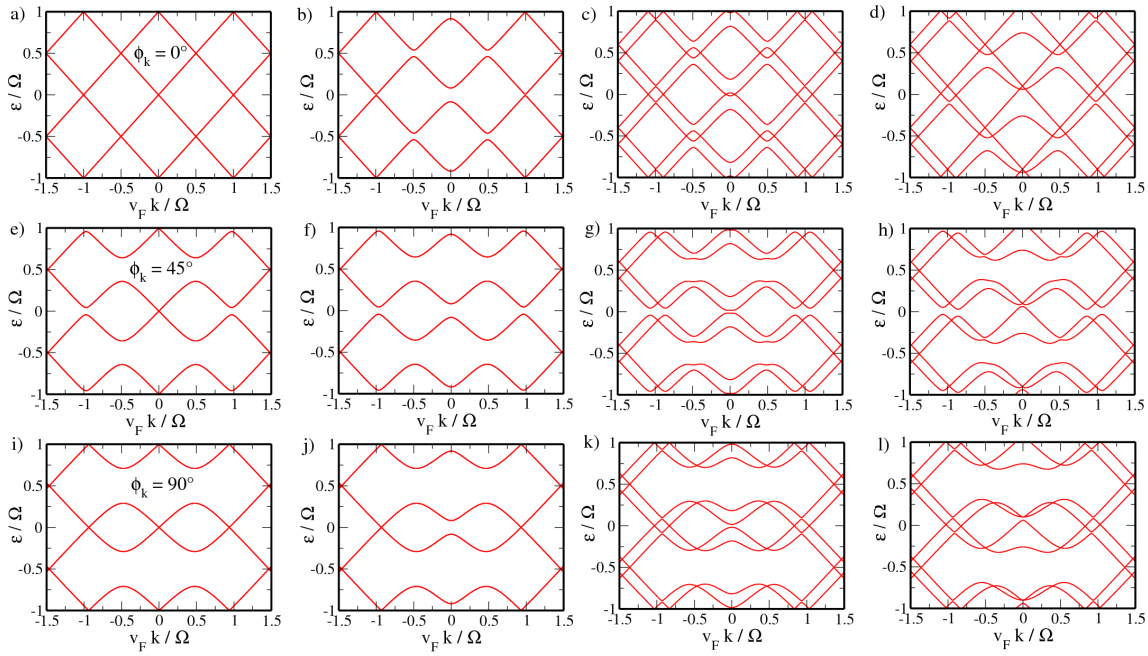

Figure 8.3.: Quasienergy spectrum of graphene under linearly polarized light ($\theta_p = 0°$) for various combinations of the SOC parameters and momentum in-plane orientations: $(\lambda_R/\Omega, \lambda_I/\Omega) = (0, 0)$ (left column), $(0, 0.1)$ (second from left), $(0.1, 0)$ (second from right), and $(0.1, 0.1)$ (right). The field strength was set to $\alpha = 0.3$.

appears in the mean energies lifting the K point degeneracy; in Fig. 8.2(a) this leads to a gap of [68]

$$\bar{\delta}_0 = \frac{4\Omega\alpha^2}{\sqrt{1+4\alpha^2}}. \tag{8.21}$$

For finite SOIs the bands react differently on the THz field and hence the spin degeneracy present in the static case of Fig. 8.1(b), where $\lambda_I = 0.1\Omega$ and $\lambda_R = 0$, disappears. Right at the Dirac point the quasienergy gap vanishes, while a new gap opens up between the conduction (or valence) band states with different spin orientations. Two of the four bands are now almost linear and not parabolic as in the case of $\alpha = 0$ and the gap in the time-averaged energies in Fig. 8.2(b) is closed. For larger momenta, $v_F k > \Omega$, the spin splitting in Fig. 8.2(b) eventually becomes so small that the bands are virtually degenerate again.

From Fig. 8.1 we can see that besides the gap at the Dirac point, additional gaps appear at $v_F k \approx 0.5n\Omega$ ($n \in \mathbb{Z}$). While these gaps are quite large for $v_F k \approx 0.5\Omega$ and Ω, their values strongly decrease for larger momenta and seem to vanish for $v_F k \gtrsim 1.5\Omega$. The reason for these gaps is the existence of photon resonances [68], i.e., the absorption and emission of photons, similar to the ac Stark effect in semiconductors [130, 140]. Here,

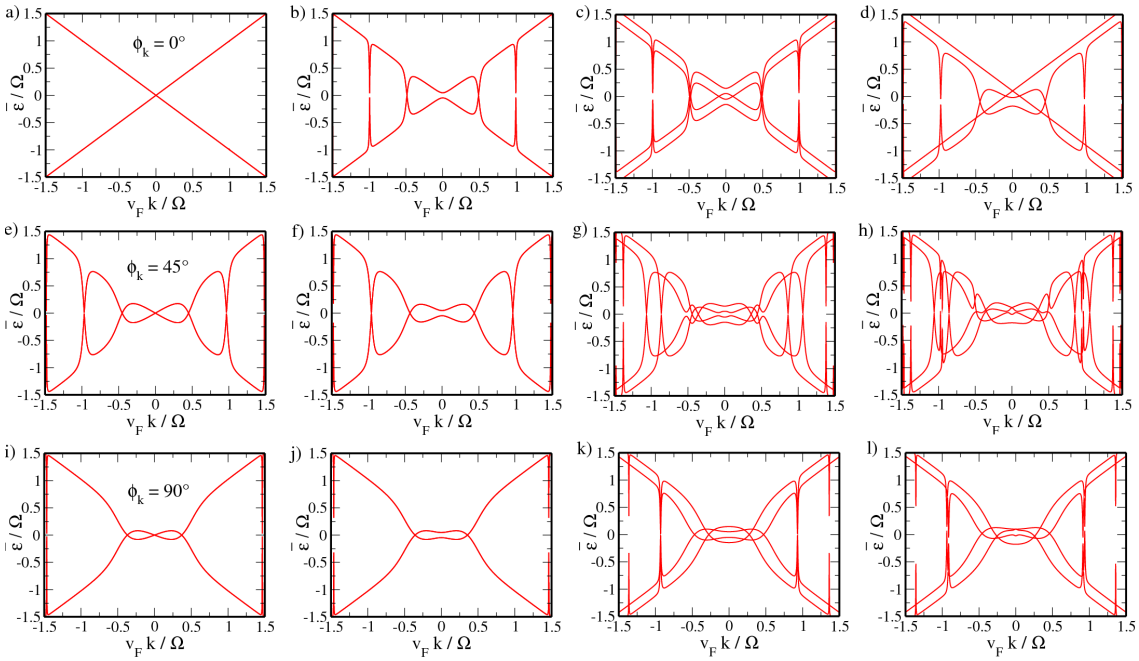

Figure 8.4.: Mean energies of graphene under linearly polarized light ($\theta_p = 0°$) for various combinations of the SOC parameters and momentum in-plane orientations: $(\lambda_R/\Omega, \lambda_I/\Omega) = (0, 0)$ (left column), $(0, 0.1)$ (second from left), $(0.1, 0)$ (second from right), and $(0.1, 0.1)$ (right). The field strength was set to $\alpha = 0.3$.

transitions might occur at the resonant points

$$E_{g,\mu\nu} - E_{g,\mu'\nu'} \approx n\Omega. \tag{8.22}$$

In the vicinity of the resonances $v_F k \approx 0.5n\Omega$, the average energies drop to zero. For large enough momenta the dips eventually become so narrow that they seem to disappear. In case the spin degeneracy is lifted ($E_{g,+\pm} \neq E_{g,-\pm}$), the above resonant condition can be fulfilled for multiple values of k and hence we observe not one but several nearby dips in the average energy spectrum, as shown in Figs. 8.2(c) and (d).

Linear polarization. If the field is linearly polarized, in the following along the x direction, the energy spectrum is expected to be strongly anisotropic. In contrast to the circular case spin degeneracy is lifted only if $\lambda_R \neq 0$.

From Fig. 8.3(a) we can see that for $\lambda_R = 0$ and $\lambda_I = 0$ the quasienergy spectrum for an in-plane angle of $\phi_k = 0°$, where $\tan\phi_k = k_y/k_x$, exactly follows the unperturbed spectrum, i.e., the field has no influence [68]. If the intrinsic SOC parameter is finite, the valence and conduction bands no longer touch at $v_F k \approx 0.5\Omega$ and the THz field induces a gap as shown in Fig. 8.3(b). The time-averaged energies in Figs. 8.4(b)-(d) exhibit characteristic dips at $v_F k \approx 0.5n\Omega$, as for circularly polarized light. However, from Figs. 8.4(a) and (d) we can see that only those bands are affected by the THz field that are (in the static limit) not linear but parabolic in momentum. Notice that contrary to the circular

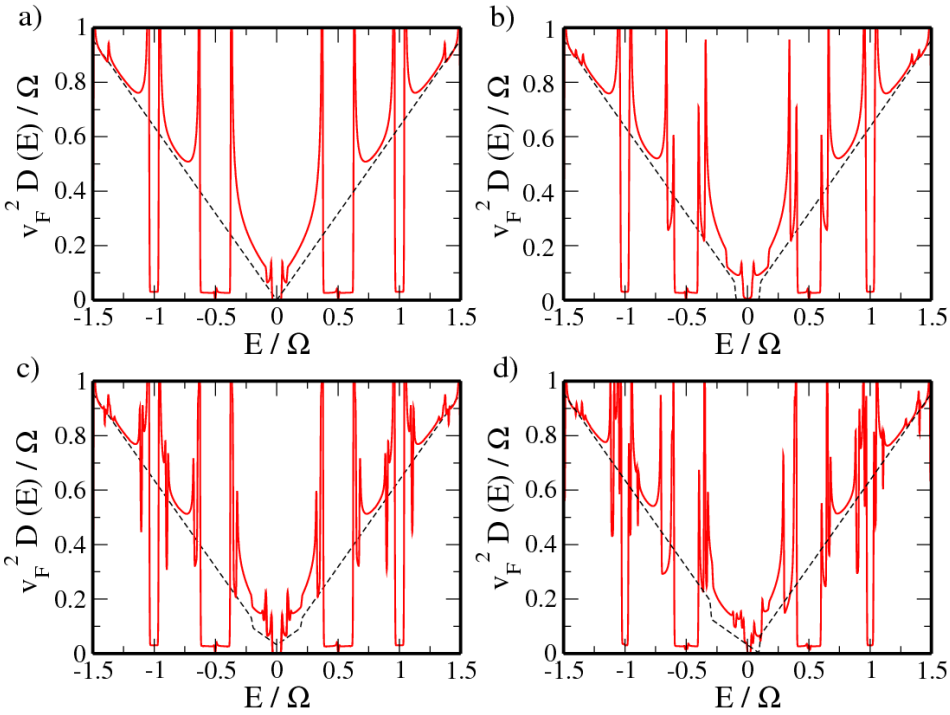

Figure 8.5.: Time-averaged DOS of graphene under circularly polarized light ($\theta_p = 45°$) for various combinations of the SOC parameters: $(\lambda_R/\Omega, \lambda_I/\Omega)$ = (a) $(0,0)$, (b) $(0,0.1)$, (c) $(0.1,0)$, and (d) $(0.1,0.1)$. The field strength was set to $\alpha = 0.3$.

case, the positions of the dips in the average energies are nearly the same for both spin orientations.

For $\phi_k = 45°$ we observe remarkable gaps in all quasienergy spectra at $v_F k \approx 0.5\Omega$ and $v_F k \approx \Omega$. In addition, for finite SOIs an additional small gap opens up at the K point separating the valence and conduction bands; see Figs. 8.3(g) and (h). The time-averaged energies resemble the circular result of Fig. 8.2. The important differences, however, are the absence [Fig. 8.4(e)] or reduction [Figs. 8.4(f)-(h)] of the gap at the Dirac point and the fact that the THz does not cause an additional spin splitting of the bands; compare Fig. 8.1(b) and Fig. 8.3(f). In contrast to the case of $\phi_k = 0°$ the positions of the resonant dips in the mean energies clearly split up for $\lambda_R \neq 0$.

Finally, for an in-plane angle perpendicular to the polarization direction ($\phi_k = 90°$), again in all four cases a distinct gap opens up at $v_F k \approx 0.5\Omega$. While for $\lambda_R = 0$ the K point energies do not change, a small gap opens up in the quasienergies in Figs. 8.3(k) and (l) where $\lambda_R \neq 0$. Furthermore, the dips in the mean energies in Figs. 8.4(i) and (j) are suppressed for $v_F k = \Omega$, but they are clearly present in Figs. 8.4(k) and (l).

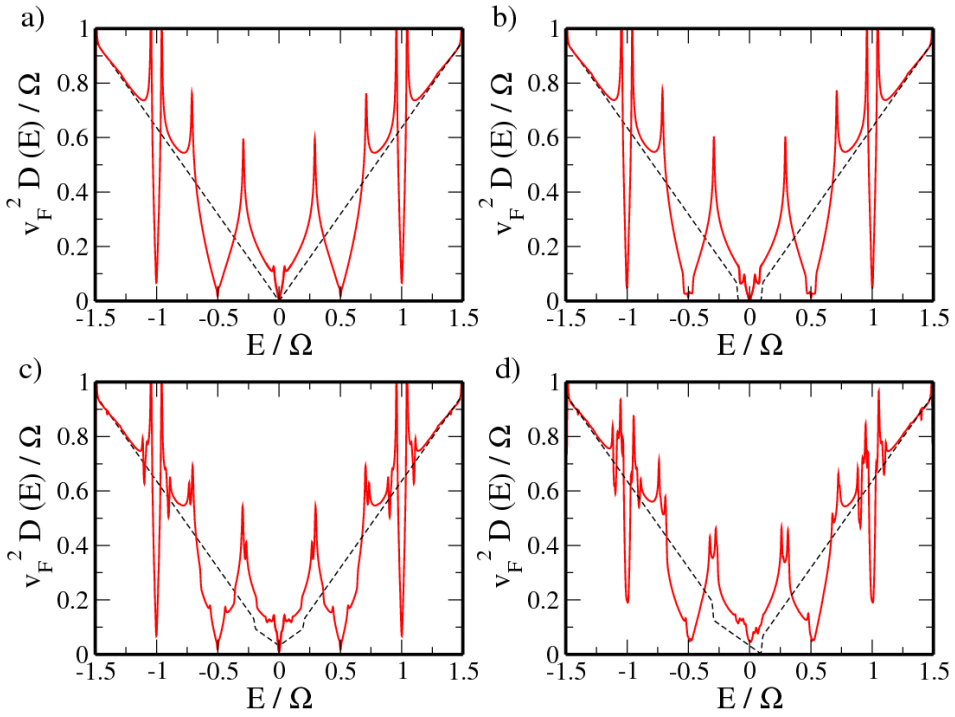

Figure 8.6.: Time-averaged DOS of graphene under linearly polarized light ($\theta_p = 0°$) for various combinations of the SOC parameters: $(\lambda_R/\Omega, \lambda_I/\Omega)$ = (a) $(0, 0)$, (b) $(0, 0.1)$, (c) $(0.1, 0)$, and (d) $(0.1, 0.1)$. The field strength was set to $\alpha = 0.3$.

8.2.2. Density of states

In Figs. 8.5 and 8.6 the time-averaged DOS [68],

$$D(E) = g_v \sum_{\mu,\nu=\pm 1} \sum_{n=-\infty}^{\infty} \int \frac{d^2k}{(2\pi)^2} \left\langle \xi^n_{\boldsymbol{k},\mu\nu} | \xi^n_{\boldsymbol{k},\mu\nu} \right\rangle \delta\left[E - \varepsilon_{\boldsymbol{k},\mu\nu} + n\Omega\right], \tag{8.23}$$

is shown for various combinations of the SOC parameters with (red solid line) and without (black dashed) electromagnetic field for circularly and linearly polarized light, respectively. The field amplitude was set to $\alpha = 0.3$. The prefactor $g_v = 2$ in Eq. (8.23) is due to the valley degeneracy of the problem.

The static DOS for zero energy (dashed lines in Figs. 8.5 and 8.6) is zero in (a) and (b) and finite in (c) and (d). In the latter case ($\lambda_R = \lambda_I$) the charge neutrality point is shifted to $\lambda_{R/I}$. The electromagnetic field yields a finite weight $\left\langle \xi^n_{\boldsymbol{k},\mu\nu} | \xi^n_{\boldsymbol{k},\mu\nu} \right\rangle$ to the subbands in the first TBZ even for momenta $v_F k > 0.5\Omega$. This leads to a distinct increase of the DOS for small energies compared to the field-free situation [67]. In Fig. 8.6(b), for example, one can see that the DOS is greatly enhanced for $|E| < \lambda_I$, while in the static case $D(E) = 0$ in this regime.

As the quasienergies $\varepsilon_{\boldsymbol{k},\mu\nu}$ have several extrema located at $v_F k \approx \pm 0.5\Omega$ and $\pm\Omega$ (see Figs. 8.1 and 8.3), the DOS exhibits pronounced Van Hove singularities [67, 68]. While due

to the isotropy of the quasienergy spectrum in the case of circularly polarized light these singularities occur for arbitrary angles of ϕ_k, for a linearly polarized field not all angles lead to Van Hove singularities. As a consequence, the associated peaks rise much stronger for $\theta_p = 45°$ compared to $\theta_p = 0°$. In the former, the DOS drops down almost vertically and remains roughly constant around $v_F k \approx 0.5\Omega$ and Ω. This is in clear contrast to the linearly polarized case, where the decrease of the DOS is much smoother and the DOS becomes peaked, with $D(E)$ being almost linear around $v_F k \approx 0.5\Omega$ and Ω [141]. If the spin degeneracy is lifted, the DOS shows additional dips in between neighboring Van Hove singularities. This is also true in Fig. 8.5(b), where the splitting is caused by the THz field and not by the Rashba term.

In the static limit signatures of SOIs in the DOS can be seen only in a narrow region with $E \lesssim 0.25\Omega$, while for larger energies it is virtually the same in all cases (see the dashed lines in Figs. 8.5 and 8.6). This changes once the field is switched on. Here, SOC manifests itself even for larger energies. Comparing Figs. 8.5(a) and (c), we see a noticeable difference even for energies $E \approx \Omega$ due to the additional dips and peaks in the DOS. This can be understood from the quasienergy spectrum, where due to the breaking of spin degeneracy several nearby points with a horizontal dispersion exist. For circularly polarized light qualitatively the same happens also for the case of a purely intrinsic coupling ($\lambda_R = 0$) as the bands split up for $\alpha \neq 0$. However, this splitting is significant only for small momenta and hence the multiple dips in Fig. 8.5(b) can be seen only for energies around $E \approx 0.5\Omega$.

8.3. Spin polarization and wave packet dynamics

We now discuss the dynamics of the real spin operators in the Heisenberg representation:

$$\hat{S}_{H,j}(t) = \hat{\sigma}_{H,0}\hat{s}_{H,j}(t), \quad \text{with} \quad j \in \{x, y, z\} \tag{8.24}$$

and $\hat{\sigma}_0$ being the unit matrix. We restrict ourselves to an initial state described by a Gaussian wave packet of width d for a single momentum, which is appropriate for a sufficiently broad initial wave packet [127]:

$$\langle \boldsymbol{r} | \Phi_{in}(t_0) \rangle = \frac{1}{\sqrt{\pi} d} e^{-\frac{r^2}{2d^2}} \begin{pmatrix} \eta_1 \\ \eta_2 \\ \eta_3 \\ \eta_4 \end{pmatrix}. \tag{8.25}$$

In the following the spinor components in Eq. (8.25) are chosen as

$$\eta_1 = -i\eta_2 = i\eta_3 = \eta_4 = 0.5, \tag{8.26}$$

i.e., the initial state is in general a linear combination of the static eigenvectors. Because of

$$\frac{d}{dt}\hat{S}_{H,z}(t) = -2\lambda_R \left[\hat{\sigma}_{H,x}\hat{s}_{H,x}(t) + \hat{\sigma}_{H,y}\hat{s}_{H,y}(t)\right], \tag{8.27}$$

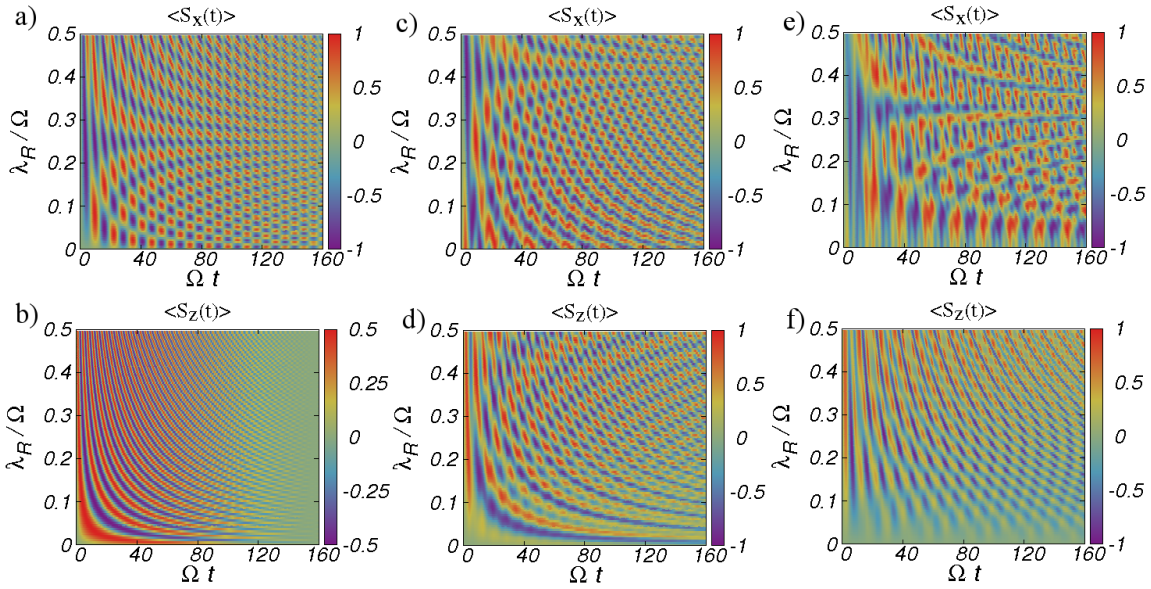

Figure 8.7.: Time evolution of the x and z components of the spin polarization without electric field (left column), under a linearly polarized field ($\theta_p = 0°$, $\alpha = 0.5$) (middle column), and for circular polarization ($\theta_p = 45°$, $\alpha = 0.5$) (right column) as a function of the Rashba coefficient. Parameters: $\lambda_I = 0.25\Omega$, $k = 0$.

changes in the initial out-of-plane spin polarization

$$\langle S_z(t_0)\rangle = |\eta_1|^2 + |\eta_2|^2 - |\eta_3|^2 - |\eta_4|^2\,, \tag{8.28}$$

where $\langle . \rangle \equiv \langle \Phi_{in}|.|\Phi_{in}\rangle$, can be induced only if the Rashba contribution is finite. Similarly, for the other two spin directions,

$$\langle S_x(t_0)\rangle = 2\,\mathrm{Re}\left\{\bar{\eta}_1\eta_3 + \bar{\eta}_2\eta_4\right\} \tag{8.29}$$

and

$$\langle S_y(t_0)\rangle = 2\,\mathrm{Im}\left\{\bar{\eta}_1\eta_3 + \bar{\eta}_2\eta_4\right\}, \tag{8.30}$$

whose dynamics are described by

$$\frac{d}{dt}\hat{S}_{H,x/y}(t) = 2\left[\lambda_R\hat{\sigma}_{H,x/y}\hat{s}_{H,z}(t) \mp \lambda_I\hat{\sigma}_{H,z}\hat{s}_{H,y/x}(t)\right], \tag{8.31}$$

at least one of the SOC coefficients has to be nonzero in order to get a nontrivial time evolution.

In Fig. 8.7 we fix the intrinsic parameter $\lambda_I = 0.25\Omega$ and vary the Rashba constant at the Dirac point. Without loss of generality, we choose $t_0 = 0$. The field strength is set to $\alpha = 0.5$. While for $\lambda_R \neq \lambda_I$ the in-plane spin polarization of the static system,

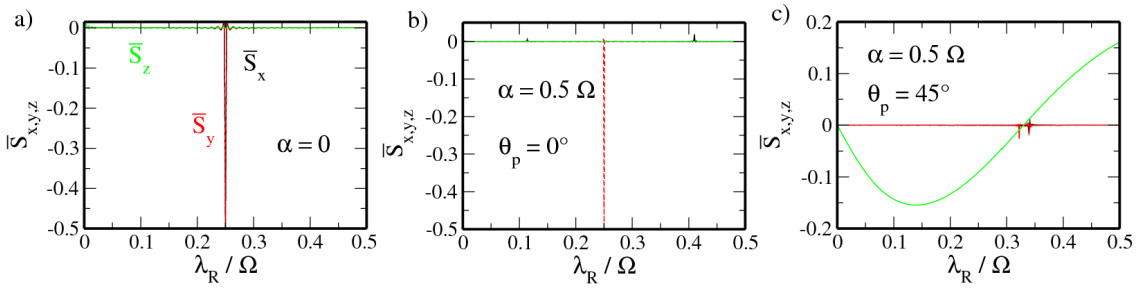

Figure 8.8.: Mean spin polarization as a function of the Rashba parameter (a) without electric field, (b) under a linearly polarized field ($\theta_p = 0°$, $\alpha = 0.5$), and (c) for circular polarization ($\theta_p = 45°$, $\alpha = 0.5$). The total simulation time is $\Omega t = 10\,000$. Parameters: $\lambda_I = 0.25\Omega$, $k = 0$.

exemplarily shown for the x component in Fig. 8.7(a), shows fast oscillations around zero, right at the point $\lambda_R = \lambda_I$ the expectation values $\langle S_x(t)\rangle$ and $\langle S_y(t)\rangle$ oscillate around a finite value. Subsequently, the mean polarization $\bar{S}_{x/y}$ [shown as black and red lines in Fig. 8.8(a)], calculated for a total simulation time of $\Omega t = 10\,000$, vanishes or is very small for $\lambda_R \neq \lambda_I$, while $\bar{S}_{x/y} = -0.5$ for $\lambda_R = \lambda_I$. If we now turn on the THz field, the time evolution of the spin operators clearly becomes more complicated; see Figs. 8.7(c) and (e). If the field is linearly polarized along the x direction, $\bar{S}_y$ is finite only for $\lambda_R = \lambda_I$ with $\bar{S}_y = -0.5$ at that point, as in the static case. However, this is no longer true for $\bar{S}_x$ as can be seen from Fig. 8.8(b) where the peak for the x component disappears. For circularly polarized light the peaks for $\bar{S}_x$ and $\bar{S}_y$ at $\lambda_R = \lambda_I$ vanish and a significantly reduced dip at $\lambda_R \approx 0.34\Omega$ appears.

The out-of-plane spin polarization ($\bar{S}_z$) of the static system oscillates around zero, where the period of the oscillations increases for larger λ_R; see Fig. 8.7(b). Therefore, in contrast to $\bar{S}_{x/y}$ the mean polarization $\bar{S}_z$ vanishes for arbitrary values of λ_R, as can be seen from the green line in Fig. 8.8(a). This remains true for linearly polarized light where $\bar{S}_z \approx 0$ in all cases. Compared to that, the situation for circularly polarized light is quite different. Here, the z component of the averaged spin oscillates as a function of λ_R and, depending on the magnitude of the Rashba parameter, $\bar{S}_z$ can be either positive, negative, or zero for $\lambda_R = 0$ and $\lambda_R \approx 0.33\Omega$. Notice that even though the intrinsic parameter has been fixed to $\lambda_I = 0.25\Omega$ in the above discussion, our findings are qualitatively insensitive to the precise value of λ_I.

The time evolution of the position operators in the Heisenberg representation is given by

$$\frac{d}{dt}\hat{\boldsymbol{r}}_H(t) = i\left[\hat{H}_{ir}, \hat{\boldsymbol{r}}_H\right] = v_F \hat{\boldsymbol{\sigma}}_{\boldsymbol{H}} \hat{s}_{H,0}(t). \tag{8.32}$$

Contrary to electron and hole gas systems [125, 127] the dissipative term proportional to momentum is missing in Eq. (8.32) due to the Dirac-like nature of the charge carriers in graphene. By calculating the usual velocity operator,

$$\hat{\boldsymbol{v}}_H(t) = v_F \hat{\boldsymbol{\sigma}}_H \hat{s}_{H,0}(t), \tag{8.33}$$

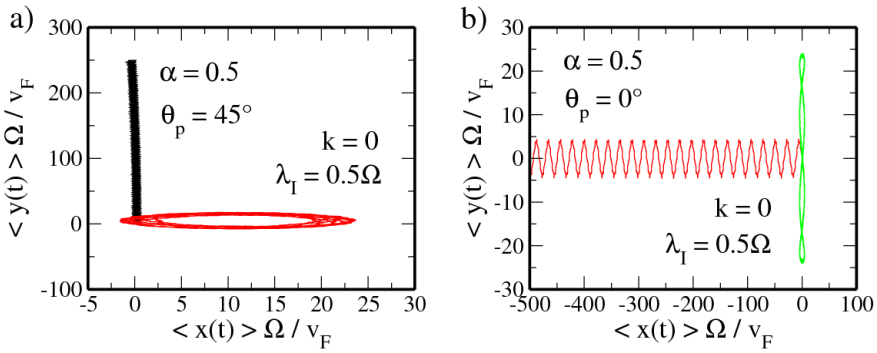

Figure 8.9.: Orbital dynamics $\langle \boldsymbol{r}(t) \rangle$ calculated for a total simulation time of $\Omega t = 1000$ for (a) circularly ($\theta_p = 45°$) and (b) linearly ($\theta_p = 0°$) polarized light for various Rashba SOC coefficients: $\lambda_R = 0$ (black line), 0.5 (red), and 0.6 (green). Parameters: $\lambda_I = 0.5\Omega$, $\alpha = 0.5$, $k = 0$.

it is thus possible to extract the orbital dynamics of the system,

$$\langle \boldsymbol{r}(t) \rangle = \langle \Phi_{in} | \hat{\boldsymbol{r}}_H(t) | \Phi_{in} \rangle, \tag{8.34}$$

with respect to the initial wave packet given in Eq. (8.25). In Fig. 8.9 this is shown for (a) circularly and (b) linearly polarized light of strength $\alpha = 0.5$ for fixed $\lambda_I = 0.5\Omega$ and two different values of the Rashba SOC parameters for a total simulation time of $\Omega t = 1000$. While for $\theta_p = 45°$ and $\lambda_R \neq 0$ the trajectory resembles an ellipse, and hence the particle becomes localized, as exemplarily shown in the red curve in Fig. 8.9(a) for $\lambda_R = 0.5\Omega$, the basic propagation is along the y direction if the Rashba contribution vanishes and compared to $\langle y \rangle$ only moderate deviations from the initial position in the x direction can be seen. For $\theta_p = 0°$ and $\lambda_R = 0.5\Omega$ [see the red curve in Fig. 8.9(b)], the main dynamics is along the x axis with small oscillations around $\langle y \rangle = 0$, while in the other case of $\lambda_R = 0.6\Omega$ (green line) the trajectory is again bounded in a finite region around $\langle x \rangle = \pm 5 v_F/\Omega$ and $\langle y \rangle = \pm 25 v_F/\Omega$, respectively.

8.4. Optical conductivity

Finally, we want to calculate the optical conductivity of irradiated graphene. As we are not interested in processes that appear right after or before the THz field is turned on and off, we consider the system in a quasistationary state and assume the probability distribution to be of the form [68, 133, 134, 135]

$$P_{\boldsymbol{k},\mu\nu} \propto e^{-\beta \bar{\varepsilon}_{\boldsymbol{k},\mu\nu}}, \tag{8.35}$$

where $\bar{\varepsilon}_{\boldsymbol{k},\mu\nu}$ are the average energies introduced in Eq. (8.20) and $\beta = 1/k_B T$ the inverse temperature. The quasiequilibrium density matrix in the basis of the Floquet states then reads [68, 133, 134, 135]

$$\langle \xi_{\boldsymbol{k},\mu\nu} | \hat{\rho}^{qe} | \xi_{\boldsymbol{k},\mu'\nu'} \rangle = \delta_{\mu,\mu'} \delta_{\nu,\nu'} f[\bar{\varepsilon}_{\mu,\nu}(\boldsymbol{k})]. \tag{8.36}$$

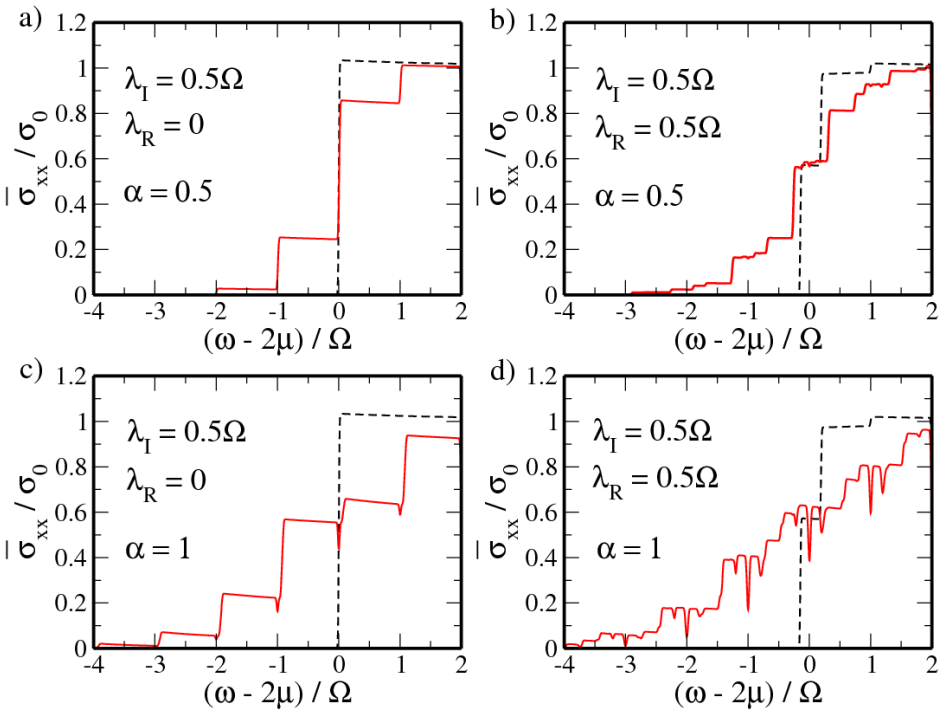

Figure 8.10.: Optical conductivity under circularly polarized light ($\theta_p = 45°$) for various field strengths $\alpha = 0$ (black dashed curves), 0.5 [red lines in (a) and (b)], and 1.0 [(c) and (d)], and SOC parameters in units of $\sigma_0 = e^2/4$.

The expression for the dissipative part of the time-averaged longitudinal optical conductivity, obtained from the nonequilibrium Green's function method derived in Ref. [68], then reads

$$\mathrm{Re}\left\{\bar{\sigma}_{xx}(\omega)\right\} = \frac{g_v \pi e^2}{\omega} \sum_{n,j=-\infty}^{\infty} \sum_{\mu,\nu,\mu',\nu'=\pm 1} \int \frac{d^2k}{(2\pi)^2} \left|\left\langle \xi^{n-j}_{\boldsymbol{k},\mu'\nu'} \middle| \hat{v}_x \middle| \xi^{n}_{\boldsymbol{k},\mu\nu} \right\rangle\right|^2 \times \\ \times \left(f\left[\bar{\varepsilon}_{\boldsymbol{k},\mu\nu}\right] - f\left[\bar{\varepsilon}_{\boldsymbol{k},\mu'\nu'}\right]\right) \delta\left[\omega + \varepsilon_{\boldsymbol{k},\mu\nu} - \varepsilon_{\boldsymbol{k},\mu'\nu'} - j\Omega\right]. \tag{8.37}$$

The quasienergies and states entering Eq. (8.37) are chosen to be in the first TBZ, although any other choice is possible as well. From the delta function in Eq. (8.37) we can see that, in principle, transitions between all kinds of subbands are possible. In the static limit only those subbands that correspond to the energies of Eq. (2.22) have a nonzero weight and Eq. (8.37) reproduces previous results [142, 143]. However, for a finite driving the weight of the other subbands becomes nonzero, whereas it increases for larger driving amplitudes and hence additional transitions become possible.

In Figs. 8.10 and 8.11 we show the optical conductivity calculated at zero temperature for a fixed Fermi energy of $\mu = 3\Omega$ under the influence of circularly and linearly polarized light, respectively. The field strength is $\alpha = 0$, 0.5, and 1.0. The main feature of the static conductivity, as shown in the dashed curves of Fig. 8.10, is its steplike behavior at $\omega = 2\mu$,

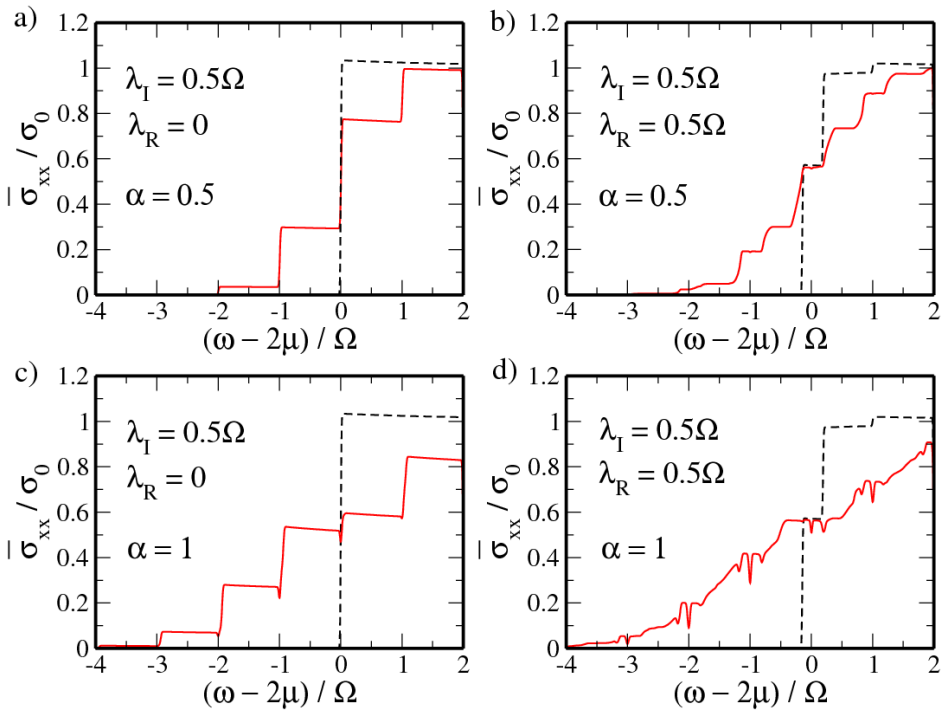

Figure 8.11.: Optical conductivity under linearly polarized light ($\theta_p = 0°$) for various field strengths $\alpha = 0$ (black dashed curves), 0.5 [red lines in (a) and (b)], and 1.0 [(c) and (d)], and SOC parameters in units of $\sigma_0 = e^2/4$.

where transitions from the valence to the conduction bands become possible. Switching on the time-dependent field leads to several additional steps in $\bar{\sigma}_{xx}$ due to photon-assisted processes [68]. By comparing Figs. 8.10(a) and (c) it becomes clear that the number of steps increases for larger coupling strengths α as the band weight is distributed over a broader range of subbands. The effect of the Rashba term, which in turn leads to a distinct breaking of the spin degeneracy of each subband, furthermore induces several intermediate steps as the number of possible transitions in the delta function of Eq. (8.37) becomes larger. From Figs. 8.10(b) and 8.11(b) we can see that the basic structure of $\bar{\sigma}_{xx}$ is the same for $\theta_p = 45°$ and $\theta_p = 0°$, but in the latter the conductivity turns out to be slightly smoother.

By increasing the field strength to $\alpha = 1.0$ we observe dips in the conductivity at $\omega = n\Omega$ [68], where the effect is clearly larger for $\theta_p = 45°$ than $\theta_p = 0°$; compare Figs. 8.10(d) and 8.11(d). These dips are due to the appearance of gaps in the quasienergy spectrum, as some transitions are no longer possible. From Figs. 8.10(c) and (d) one can see that while the static conductivities (dashed curves) are quite similar in both cases, i.e., the effect of λ_R is only slight, remarkable differences occur in the driven case, and hence SOC effects are clearly enhanced.

8.5. Summary

In this chapter we have investigated the effect of a time-dependent electromagnetic field on a monolayer of graphene in the presence of SOIs of the intrinsic and Rashba type.

We have demonstrated that a circularly polarized THz field can both induce a gap in the quasienergy spectrum and close an existing gap. In the opposite case of a linear polarization the spectrum was shown to be highly anisotropic and, depending on the strength of the SOC parameters and on the orientation of the field, gaps in the spectrum might appear at the Dirac point and at the photon resonances $v_F k \approx 0.5n\Omega$, or become suppressed. While the effect of SOIs on the DOS of the static sample can be seen only for energies smaller than $E \lesssim 0.25\Omega$, due to the existence of a multiple number of dips and peaks, signatures of SOC in the DOS of irradiated graphene appear even at larger energies.

By introducing a time-dependent electromagnetic field it is possible to induce a finite net out-of-plane spin polarization in the sample, where its sign and magnitude can be modulated by changing the ratio of the SOC parameters. Experimentally this can be done by adjusting the Rashba coefficient via an electric gate.

In the final part of the chapter the dissipative part of the longitudinal optical conductivity has been calculated. As reported already in Ref. [68], the conductivity of irradiated graphene exhibits a multistep structure as transitions between a variety of subbands become possible. The number of steps depends not only on the coupling strength, but also on the magnitude of the Rashba parameter and on the polarization direction. For large coupling strengths the conductivity furthermore drops down for frequencies close to the THz energy as some transitions become suppressed due to the appearance of gaps in the quasienergy spectrum.

Chapter 9.

9 Conclusions

The intent of this thesis is to present a thorough discussion of the dynamical charge and current responses of various promising 2D materials, putting special emphasis on the effects arising from the different types of SOIs.

In Chap. 2 we have introduced the single-particle Hamiltonian of graphene, ML-MDS, and hole-doped III-V semiconductors. Without giving many details on the elongate TB and $k \cdot p$ calculations, we summarized the basic steps to derive an adequate model to properly describe the noninteracting systems for realistic charge carrier concentrations.

This is followed by a chapter, where the basic ingredients to investigate many-body effects in low-dimensional solid-state systems are summarized. In Sec. 3.1 we have recapitulated the Kubo formalism and introduced the charge and current susceptibilities as the central transport quantities. A simple but powerful way to incorporate many-body effects by means of the RPA has been described in Sec. 3.2. We have shown how substantial information on the internal excitations of the system, such as the plasmon spectrum and the dissipative EHC, can be extracted from the RPA-improved DF.

As a first application, we have discussed the DF of graphene in Chap. 4, taking into account the effect of SOIs of the intrinsic and Rashba type. The main accomplishment of this chapter is the solution of the free polarizability in terms of closed analytical expressions for arbitrary wave vector, frequency, chemical potential, and SOC parameters. Often, SOIs in graphene are neglected as their effect on the energy spectrum is considered to be very small. However, the inclusion of SOIs is an important step in view of recent advances in the fabrication of other 2D honeycomb structures with similar properties than graphene such as silicene [46, 47] or ML-MDS [48, 53, 54]. Moreover, a number of recent works have proposed ways to enlarge the SOC parameters in graphene-like materials significantly by changing the environment of the sample [41, 42, 43, 44, 45]. In this chapter we have shown how SOIs in graphene-based plasmonic circuitries can possibly be used to manipulate the plasmon energy and lifetime. For example, for sufficiently large intrinsic SOC the plasmon mode remains undamped even for larger wave vectors as a gap opens up between the intra- and interband EHC [99]. In the other case of a large Rashba contribution damping appears already for small wave vectors due to interband transitions between conduction (or valence) band states with different spin orientations. Based on a combined analytical and numerical analysis of the screened Coulomb potential in Sec. 4.4, we could

predict a beating of Friedel oscillations in doped graphene if the spin degeneracy is lifted by a sufficiently large Rashba SOC.

Restricting ourselves to a purely intrinsic SOI, analytical results for the transversal and longitudinal parts of the current-current susceptibility of gapped graphene are presented in Chap. 5. Their static limits allow to determine the orbital and Pauli part of the magnetic susceptibility of the sample. While in gapless graphene the orbital magnetic susceptibility diverges at the charge neutrality point [109], the band gap leads to a finite value being proportional to the inverse of the SOC parameter λ_I [110]. In doped samples, on the other hand, the orbital magnetic susceptibility vanishes independently of the value of λ_I. The nonrelativistic limit of gapped graphene was shown to reproduce the results of an ordinary 2DEG, but with the peculiarity of a pseudospin Zeeman term due to the existence of a pseudospin degree of freedom [60]. This limit is not of purely academic interest, but is closely related to other honeycomb structures with a large band gap such as ML-MDS, where electrons and holes are separated by an energy gap of 1.82 eV.

This leads us to Chap. 6, where we have investigated the plasmon spectrum of ML-MDS for various carrier concentrations. Due to the complicated analytical structure of the eigensystem, the analytical treatment of the problem seems to be very difficult and the DF was solved by numerical methods. We have shown that while in graphene damping of plasmons is caused by interband transitions [61, 62], collective charge excitations in ML-MDS rather enter the intraband EHC. Another noteworthy difference between graphene and ML-MDS is the carrier density dependence of the plasmon energies being $\omega_q \propto n^{1/4}$ in graphene, while $\omega_q \propto n^{1/2}$ in ML-MDS. Moreover, a thorough analysis of the plasmon spectrum predicts a clear asymmetry in the plasmon energies of p- and n-doped samples due to the lack of electron-hole symmetry in ML-MDS. A numerical inspection of the screened Coulomb potential shows that the breaking of spin degeneracy caused by the considerable intrinsic SOI (of 80 meV) leads to a beating of Friedel oscillations for sufficiently large carrier concentrations.

Motivated by recent works on the effects of SOIs on the collective charge excitations of 2DEGs [64, 65] and by our results regarding graphene and ML-MDS, we asked ourselves in Chap. 7 how SOIs manifest themselves in the plasmon spectrum of p-doped GaAs and InAs QWs. We also tried to find ways to manipulate the plasmon properties by adjusting the SOC parameters in a suitable way. In contrast to graphene, the SOC strengths in III-V semiconductors are notable [56] and do not need to be enlarged by deliberate manipulation of the sample. Our findings show that for GaAs a pronounced anisotropy in the plasmon spectrum occurs. Depending on the direction of the incident beam, plasmons are either damped or long-lived. This opens, in principle, the possibility of filtering plasmons with distinct orientations. Although this was proposed earlier in Refs. [65] for an electron gas, the anisotropy is expected to be more pronounced in hole gases. Our results on InAs have furthermore demonstrated that the lifetime of the long-wavelength plasmons can be modulated by changing the Rashba coupling strength via an electric field. Interestingly, the critical field at which a finite damping occurs is direction-dependent. These features might be useful for applications such as plasmon transistors [64], where excitations in the source can be detected in the drain, depending on the Rashba field.

In Chap. 8 we have driven a monolayer of graphene out of equilibrium by applying a

strong time-dependent electromagnetic field. We could show that the field might cause significant changes in the single-particle properties by opening [66, 67] or closing band gaps in the energy spectrum. It turns out to be possible to induce a finite net out-of-plane spin polarization in the sample, where its sign and magnitude can be modulated by changing the ratio of the SOC parameters. Using the nonequilibrium formalism applied to the conductivity as described in Ref. [68], the dissipative part of the optical conductivity of irradiated graphene has been calculated. The conductivity of the irradiated sample exhibits a multistep structure as transitions between a variety of subbands become possible. Furthermore, as a consequence of the appearance of gaps in the quasienergy spectrum, the conductivity drops down for frequencies close to the photon energy.

Having summarized the main accomplishments of this thesis, let us comment on what has yet to be done and could be the subject of future works. The numerical codes used in Chaps. 6-8 are quite general and can be applied to a variety of other promising materials without large effort. As examples, we mention the irradiation of a monolayer of silicene, n- or p-doped semiconductor QWs, particularly taking into account the different subbands in the QW, and topological insulators. Due to the rich physics of all of these systems, it is worth to have a closer look on the changes in the carrier dynamics induced by a time-dependent field, and try to find possibilities to change the topology of the material. In Ref. [124] the latter has been discussed for HgTe/CdTe QWs in the context of Floquet topological insulators. Another interesting topic is the analysis of the plasmon spectrum in finite-size samples such as graphene ribbons [144] or quantum rings [145]. In this case the numerical code needs to be adjusted in order to first solve for the eigensystem of the finite sample, e.g., using the finite difference method. In the second step, the imaginary and real parts of the DF and hence the ELF can be calculated using the methods described in Chap. 3.

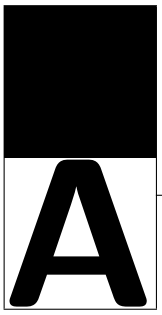

Appendix A.

Details on the calculation of the free polarizability of graphene

In this chapter we summarize major steps in the calculation of the free polarizability of graphene. We begin with the undoped case in Sec. A.1 and generalize the result to the case of a finite doping in Sec. A.2. For brevity, we set $v_F = 1$ throughout this chapter.

A.1. Zero doping

The undoped polarizability in Eq. (4.6) is composed of four parts:

$$\chi^{0,un}_{\rho\rho}(q,\omega) = \sum_{\eta_1,\eta_3=\pm 1} \chi^{\eta_1 - \to \eta_3 +}(q,\omega). \tag{A.1}$$

Here, we introduced the notation

$$\chi^{\eta_1\eta_2\to\eta_3\eta_4}(q,\omega) = g_v \int \frac{d^2k}{(2\pi)^2} \left| \left\langle \xi_{g,\eta_1\eta_2}(\boldsymbol{k}) \middle| \xi_{g,\eta_3\eta_4}(\boldsymbol{k}+\boldsymbol{q}) \right\rangle \right|^2 \times \\ \times \frac{f\left[E_{g,\eta_1\eta_2}(k)\right] - f\left[E_{g,\eta_3\eta_4}(|\boldsymbol{k}+\boldsymbol{q}|)\right]}{\omega - E_{g,\eta_3\eta_4}(|\boldsymbol{k}+\boldsymbol{q}|) + E_{g,\eta_1\eta_2}(k) + i0} \tag{A.2}$$

describing transitions from the initial band $E_{g,\eta_1\eta_2}(k)$ to the final band $E_{g,\eta_3\eta_4}(|\boldsymbol{k}+\boldsymbol{q}|)$. The eigenstates $\xi_{g,\eta_1\eta_2}(\boldsymbol{k})$ and $\xi_{g,\eta_3\eta_4}(\boldsymbol{k}+\boldsymbol{q})$ can be found in Eqs. (4.1) and (4.2). Due to the relations

$$\chi^{--\to++}_{(\lambda_R)}(q,\omega) = \chi^{+-\to-+}_{(-\lambda_R)}(q,\omega) \tag{A.3}$$

and

$$\chi^{+-\to++}_{(\lambda_R)}(q,\omega) = \chi^{--\to-+}_{(-\lambda_R)}(q,\omega), \tag{A.4}$$

only two independent contributions remain. With the help of the Dirac identity in Eq. (3.8), the imaginary parts read

$$\begin{aligned}
\mathrm{Im}\left\{\chi^{--\to-+}(q,\omega)\right\} &= -\frac{g_v}{4\pi}\int_0^\infty dkk\int_0^{2\pi}d\phi_k\sum_{\alpha=\pm1}\alpha\left|\left\langle\xi_{g,--}(\boldsymbol{k})\middle|\xi_{g,-+}(\boldsymbol{k}+\boldsymbol{q})\right\rangle\right|^2\times\\
&\qquad\times\delta\left[\omega-\alpha\left(E_{g,-+}\left(|\boldsymbol{k}+\boldsymbol{q}|\right)-E_{g,--}(k)\right)\right]\\
&= \frac{g_v}{16}\,\theta\left[\omega^2-q^2-4{\lambda_+}^2\right]\left[\frac{3q^4-4{\lambda_+}^2q^2-5q^2\omega^2+2\omega^4}{\left(\omega^2-q^2\right)^{3/2}}\right.\\
&\qquad\left.-\frac{\left|q^2-\omega\left(\omega-2\lambda_+\right)\right|+\left|q^2-\omega\left(\omega+2\lambda_+\right)\right|}{\omega}\right]
\end{aligned}\tag{A.5}$$

and

$$\begin{aligned}
\mathrm{Im}\left\{\chi^{+-\to-+}(q,\omega)\right\} &= -\frac{g_v}{4\pi}\int_0^\infty dkk\int_0^{2\pi}d\phi_k\sum_{\alpha=\pm1}\alpha\left|\left\langle\xi_{g,+-}(\boldsymbol{k})\middle|\xi_{g,-+}(\boldsymbol{k}+\boldsymbol{q})\right\rangle\right|^2\times\\
&\qquad\times\delta\left[\omega-\alpha\left(E_{g,-+}\left(|\boldsymbol{k}+\boldsymbol{q}|\right)-E_{g,+-}(k)\right)\right]\\
&= -\frac{g_v}{8\pi}\int_{|\lambda_-|}^\infty dy\,\frac{\sqrt{\omega_+^2-q^2}\sqrt{\frac{q^2}{4}\frac{\left(q^2-\omega_+^2+4\lambda_I^2\right)\left(q^2-\omega_+^2+4\lambda_R^2\right)}{\left(q^2-\omega_+^2\right)^2}-\left[y-\frac{\omega_+}{2}\left(1+\frac{4\lambda_R\lambda_I}{q^2-\omega_+^2}\right)\right]^2}}{(y-\lambda_-)(\omega-y+\lambda_-)}\times\\
&\qquad\times\theta\left[1-\left(\frac{\omega_+^2-q^2-2\omega_+y-4\lambda_R\lambda_I}{2q\sqrt{y^2-\lambda_-^2}}\right)^2\right]\theta\left[\omega_+^2-q^2-4\gamma^2\right]\\
&= -\frac{g_v}{8}\,\theta\left[\omega_+^2-q^2-4\gamma^2\right]\left[\sqrt{\omega_+^2-q^2}-\frac{\left|q^2-\omega\left(\omega+2\lambda_-\right)\right|}{2\omega}-\frac{\left|q^2-\omega\left(\omega+2\lambda_+\right)\right|}{2\omega}\right].
\end{aligned}\tag{A.6}$$

Here, we have introduced the notations

$$\lambda_\pm = \lambda_R \pm \lambda_I, \tag{A.7}$$

$$\omega_\pm = \omega \pm 2\lambda_R, \tag{A.8}$$

$$\gamma = \max\left\{\lambda_R, \lambda_I\right\}, \tag{A.9}$$

and

$$y = \sqrt{k^2+\lambda_-^2}. \tag{A.10}$$

We can now make use of Eq. (3.9) to get the real part. The first contribution reads

$$\begin{aligned}
&\mathrm{Re}\left\{\chi^{--\to-+}(q,\omega)\right\} = \frac{2}{\pi}\mathcal{P}\int_0^\infty d\omega' \frac{\omega'}{\omega'^2-\omega^2}\,\mathrm{Im}\left\{\chi^{--\to-+}(q,\omega')\right\} \\
&= \frac{g_v}{8\pi}\left\{\frac{3q^2\omega^2+4q^2\lambda_+^2-3q^4-2\omega^4}{(q^2-\omega^2)^{3/2}}\frac{\pi}{2}\,\theta\left[q-\omega\right] - K_{\lambda_+}\left(4\lambda_+^2\right) + \mathcal{L}_{\lambda_+}\left(\sqrt{q^2+4\lambda_+^2}\right)\right. \\
&\qquad \left. + 2\,\mathcal{L}_{-\lambda_+}\left(\sqrt{q^2+\lambda_+^2}+\lambda_+\right) - \mathcal{L}_{-\lambda_+}\left(\sqrt{q^2+4\lambda_+^2}\right)\right\},
\end{aligned} \tag{A.11}$$

where we introduced the functions

$$K_{\lambda_\pm}(x) = 2\sqrt{x} + \frac{4q^2\lambda_\pm^2}{(q^2-\omega^2)\sqrt{x}} - \left(3q^4-5q^2\omega^2+2\omega^4-4q^2\lambda_\pm^2\right)\mathrm{Re}\left\{\frac{\arctan\left(\frac{\sqrt{x}}{\sqrt{q^2-\omega^2}}\right)}{(q^2-\omega^2)^{3/2}}\right\} \tag{A.12}$$

and

$$\mathcal{L}_{\lambda_\pm}(x) = x + \lambda_\pm \ln\left|x^2-\omega^2\right| - \frac{\omega^2-q^2}{2\omega}\ln\left|\frac{x+\omega}{x-\omega}\right|. \tag{A.13}$$

The second contribution can be solved in a similar way:

$$\begin{aligned}
&\mathrm{Re}\left\{\chi^{+-\to-+}(q,\omega)\right\} = \frac{2}{\pi}\mathcal{P}\int_0^\infty d\omega' \frac{\omega'}{\omega'^2-\omega^2}\,\mathrm{Im}\left\{\chi^{+-\to-+}(q,\omega')\right\} \\
&= \frac{g_v}{4\pi}\left[-2\lambda_R(1+\ln 4) + \frac{1}{2}\,\mathrm{Re}\left\{\sqrt{q^2-\omega_+^2}\arcsin\frac{\omega_+}{q} - \sqrt{q^2-\omega_-^2}\arcsin\frac{-\omega_-}{q}\right\}\right. \\
&\qquad + \frac{1}{2}\left[G_{\frac{\omega_+}{2}}\left(\sqrt{q^2+4\gamma^2}-\omega_+\right) + G_{-\frac{\omega_-}{2}}\left(\sqrt{q^2+4\gamma^2}+\omega_-\right)\right] \\
&\qquad -\theta\left[\lambda_+\right]\mathcal{L}_{\lambda_-}\left(\sqrt{q^2+\lambda_-^2}-\lambda_-\right) + \frac{1}{2}\,\mathrm{sign}\left(\lambda_+\right)\mathcal{L}_{\lambda_-}\left(\sqrt{q^2+4\gamma^2}-2\lambda_R\right) \\
&\qquad \left. -\theta\left[\lambda_-\right]\mathcal{L}_{\lambda_+}\left(\sqrt{q^2+\lambda_+^2}-\lambda_+\right) + \frac{1}{2}\,\mathrm{sign}\left(\lambda_-\right)\mathcal{L}_{\lambda_+}\left(\sqrt{q^2+4\gamma^2}-2\lambda_R\right)\right],
\end{aligned} \tag{A.14}$$

with

$$\begin{aligned}
G_\omega(x) &= \sqrt{(x+\omega)^2-q^2} + \omega\ln\left(\sqrt{(x+\omega)^2-q^2}+x+\omega\right) \\
&\quad - \sqrt{\omega^2-q^2}\ln\frac{\omega x+\omega^2-q^2+\sqrt{\omega^2-q^2}\sqrt{(x+\omega)^2-q^2}}{x}.
\end{aligned} \tag{A.15}$$

Equations (A.11) and (A.14) can now further be simplified to the final results in Eqs. (4.13) and (4.14), respectively.

A.2. Finite doping

The free polarizability in the n-doped case can be expressed as

$$\chi_{\rho\rho}^{0,do}(q,\omega) = \chi_{\rho\rho}^{0,un}(q,\omega) + \delta\chi_{k_{F+}}(q,\omega) + \delta\chi_{k_{F-}}(q,\omega). \tag{A.16}$$

The contribution to the doped polarizability with an initial state in band E_{-+},

$$\delta\chi_{k_{F-}}(q,\omega) = g_v \sum_{\mu,\nu=\pm1} \int_0^{k_{F-}} \frac{d^2k}{(2\pi)^2} \sum_{\alpha=\pm1} \frac{\alpha \left|\left\langle \xi_{g,-+}(\boldsymbol{k}) \middle| \xi_{g,\mu\nu}(\boldsymbol{k}+\boldsymbol{q}) \right\rangle\right|^2}{\omega - \alpha\left[E_{g,\mu\nu}\left(|\boldsymbol{k}+\boldsymbol{q}|\right) - E_{g,-+}(k)\right] + i0}, \tag{A.17}$$

can be written as

$$\begin{aligned}
\delta\chi_{k_{F-}}(q,\omega) = g_v \int_0^{k_{F-}} \frac{d^2k}{(2\pi)^2} \times \\
\times \Bigg[& \frac{\left(\omega + i0 + \sqrt{k^2+\lambda_+^2} + \sqrt{|\boldsymbol{k}+\boldsymbol{q}|^2+\lambda_+^2}\right) \left|\left\langle \xi_{g,-+}(\boldsymbol{k}) \middle| \xi_{g,-+}(\boldsymbol{k}+\boldsymbol{q}) \right\rangle\right|^2}{\left(\omega + i0 + \sqrt{k^2+\lambda_+^2}\right)^2 - \left(|\boldsymbol{k}+\boldsymbol{q}|^2+\lambda_+^2\right)} \\
& + \frac{\left(\omega + i0 + \sqrt{k^2+\lambda_+^2} - \sqrt{|\boldsymbol{k}+\boldsymbol{q}|^2+\lambda_+^2}\right) \left|\left\langle \xi_{g,-+}(\boldsymbol{k}) \middle| \xi_{g,--}(\boldsymbol{k}+\boldsymbol{q}) \right\rangle\right|^2}{\left(\omega + i0 + \sqrt{k^2+\lambda_+^2}\right)^2 - \left(|\boldsymbol{k}+\boldsymbol{q}|^2+\lambda_+^2\right)} \\
& + \frac{\left(\omega_- + i0 + \sqrt{k^2+\lambda_+^2} - \sqrt{|\boldsymbol{k}+\boldsymbol{q}|^2+\lambda_-^2}\right) \left|\left\langle \xi_{g,-+}(\boldsymbol{k}) \middle| \xi_{g,+-}(\boldsymbol{k}+\boldsymbol{q}) \right\rangle\right|^2}{\left(\omega_- + i0 + \sqrt{k^2+\lambda_+^2}\right)^2 - \left(|\boldsymbol{k}+\boldsymbol{q}|^2+\lambda_-^2\right)} \\
& + \frac{\left(\omega_- + i0 + \sqrt{k^2+\lambda_+^2} + \sqrt{|\boldsymbol{k}+\boldsymbol{q}|^2+\lambda_-^2}\right) \left|\left\langle \xi_{g,-+}(\boldsymbol{k}) \middle| \xi_{g,++}(\boldsymbol{k}+\boldsymbol{q}) \right\rangle\right|^2}{\left(\omega_- + i0 + \sqrt{k^2+\lambda_+^2}\right)^2 - \left(|\boldsymbol{k}+\boldsymbol{q}|^2+\lambda_-^2\right)} \\
& + (\omega \to -\omega) \Bigg],
\end{aligned} \tag{A.18}$$

where $(\omega \to -\omega)$, and thus $(\omega_- \to -\omega_+)$, denotes terms with the sign of the frequency changed compared to the preceding expression. The corresponding expression for band E_{++} can be obtained by substituting $\lambda_R \to -\lambda_R$ and $k_{F-} \to k_{F+}$, with $k_{F\pm}$ being the Fermi wave vector given in Eq. (2.23).

In the doped case the analytical solution of the imaginary part is quite complicated and the Kramers-Kronig relation in Eq. (3.9) does not seem to be helpful to obtain the real part. Therefore, we calculate the real part independently of the imaginary part by solving the 2D integral in momentum space instead. After carrying out the angle integration and choosing a proper substitution,

$$x = \sqrt{k^2+\lambda_+^2} - \lambda_+, \tag{A.19}$$

we arrive at

$$\begin{aligned}\mathrm{Re}\left\{\delta\chi_{k_{F-}}(q,\omega)\right\} = -\frac{g_v}{2\pi}\,\mathrm{Re}\Bigg\{\mathcal{P}\int_\epsilon^{\mu-\lambda_I} dx\;\Bigg[&\frac{x+\lambda_R}{2x}\\ &+\frac{\left[q^2-(x+\frac{\omega}{2})(x+\frac{\omega}{2}+\lambda_+)\right]^2}{x(x+\frac{\omega}{2})}\,\frac{\mathrm{sign}\left[q^2-\omega^2-2\omega(x+\lambda_+)\right]}{\sqrt{q^2-\omega^2}\sqrt{\frac{q^2}{4}\left(1+\frac{4\lambda_+^2}{q^2-\omega^2}\right)-(x+\frac{\omega}{2}+\lambda_+)^2}}\\ &-\frac{\sqrt{q^2-\omega_-^2}\,\sqrt{\frac{q^2}{4}\frac{\left(q^2-\omega_+^2+4\lambda_I^2\right)\left(q^2-\omega_+^2+4\lambda_R^2\right)}{\left(q^2-\omega_+^2\right)^2}-\left(x+\frac{\omega_+}{2}\left(1+\frac{4\lambda_R\lambda_I}{q^2-\omega_+^2}\right)+\lambda_+\right)^2}}{4x(x+\omega)}\times\\ &\qquad\times\mathrm{sign}\left(q^2-\omega_-^2-2\omega_-(x+\lambda_+)-4\lambda_R\lambda_I\right)\Bigg]\\ &+(\omega\to-\omega)\Bigg\}.\end{aligned} \tag{A.20}$$

The infinitesimal parameter $\epsilon \to 0$ is required to avoid a divergence in the polarizability for $x \to 0$. The integrals in Eq. (A.20) can now be solved in terms of trigonometric and hyperbolic functions [146]. In order to simplify the expressions, we use the shorthand notation [100]

$$\hat{f}(x)\Big|_a^b = \mathrm{sign}\,(b-x)\,[f(b)-f(x)] - \mathrm{sign}\,(a-x)\,[f(a)-f(x)]\,. \tag{A.21}$$

The result can then be written as

$$\begin{aligned}\mathrm{Re}\left\{\delta\chi_{k_{F-}}(q,\omega)\right\} = &-\frac{g_v\,(\mu-\lambda_I)}{2\pi}-\frac{g_v\lambda_R}{4\pi}\ln\frac{\mu-\lambda_I}{\epsilon}\\ &+\frac{g_v}{2\pi\omega}\,\mathrm{Re}\Bigg\{\mathrm{sign}\,(\omega)\left[\hat{\mathcal{R}}_1^{\omega}\left(\frac{q^2-\omega^2-2\lambda_+\omega}{2\omega}\right)\Big|_\epsilon^{\mu-\lambda_I}-\hat{\mathcal{R}}_1^{-\omega}\left(\frac{q^2+\omega^2-2\lambda_+\omega}{2\omega}\right)\Big|_\omega^{\mu-\lambda_I+\omega}\right]\\ &\qquad-\mathrm{sign}\,(\omega_-)\left[\hat{\mathcal{R}}_2^{\omega}\left(\frac{q^2-\omega^2+2\lambda_-\omega}{2\omega_-}\right)\Big|_\epsilon^{\mu-\lambda_I}-\hat{\mathcal{R}}_2^{-\omega}\left(\frac{q^2+\omega^2-2\lambda_+\omega}{2\omega_-}\right)\Big|_\omega^{\mu-\lambda_I+\omega}\right]\Bigg\}\\ &+\quad(\omega\to-\omega)\,,\end{aligned} \tag{A.22}$$

with

$$\mathcal{R}_i^{\omega}(x) = \frac{c_i^{\omega}}{\gamma_i^{\omega}}\sqrt{r_i^{\omega}}-\frac{\sqrt{\alpha_i^{\omega}}}{4}\ln\frac{2\alpha_i^{\omega}+\beta_i^{\omega}x+2\sqrt{\alpha_i^{\omega}}\sqrt{r_i^{\omega}}}{x}+\frac{\tilde{c}_i^{\omega}}{\sqrt{\gamma_i^{\omega}}}\ln\left(2\sqrt{\gamma_i^{\omega}}\sqrt{r_i^{\omega}}+2\gamma_i^{\omega}x+\beta_i^{\omega}\right) \tag{A.23}$$

and $r_i^\omega = \alpha_i^\omega + \beta_i^\omega x + \gamma_i^\omega x^2$. The coefficients read:

$$\alpha_1^\omega = \frac{\left[q^2 - \omega\left(\omega + 2\lambda_+\right)\right]^2}{4}, \tag{A.24}$$

$$\alpha_2^\omega = \frac{\left[q^2 - \omega\left(\omega_- - 2\,\mathrm{sign}\left(\omega\right)\lambda_I\right)\right]^2}{4}, \tag{A.25}$$

$$\beta_1^\omega = \left(\omega^2 - q^2\right)\left(2\lambda_+ + \omega\right), \tag{A.26}$$

$$\beta_2^\omega = 8\lambda_R^2\lambda_I - 2\lambda_R\lambda_I\left(\omega + |\omega|\right) - \mathrm{sign}\left(\omega\right)\left(\omega - 2\lambda_R\right)\left(q^2 - \omega_-^2\right), \tag{A.27}$$

$$\gamma_1^\omega = \omega^2 - q^2 \quad , \quad \gamma_2^\omega = |\omega|_-^2 - q^2, \tag{A.28}$$

$$c_1^\omega = \frac{\omega^2}{3} + \frac{2\lambda_+ + 7\omega}{12}\omega + \frac{12\lambda_+^2 - 4q^2 + 5\omega^2}{8} - \frac{2\alpha_1^\omega}{3\gamma_1^\omega}, \tag{A.29}$$

$$\tilde{c}_1^\omega = \frac{\alpha_1^\omega\left(2\lambda_+ - \omega\right)}{4\gamma_1^\omega} + \frac{3\omega^3 + 6\lambda_+\omega^2 - 4(q^2 + \lambda_+^2)\omega - 8\lambda_+^3}{16}, \tag{A.30}$$

$$c_2^\omega = \frac{\gamma_2^\omega}{4} \quad , \quad \tilde{c}_2^\omega = \frac{\beta_2^\omega}{8}. \tag{A.31}$$

The calculation of the imaginary part is similar. Starting from Eq. (A.18) and carrying out the angle integration, we arrive at

$$\begin{aligned}
\mathrm{Im}\left\{\delta\chi_{k_{F-}}(q,\omega)\right\} = \frac{g_v}{2\pi}\,\mathrm{Re}\Bigg\{\mathcal{P}\int_\epsilon^{\mu-\lambda_I} dx \times \\
\times \Bigg[\frac{\left[q^2 - (x+\frac{\omega}{2})(x+\frac{\omega}{2}+\lambda_+)\right]^2}{x(x+\frac{\omega}{2})}\,\frac{\mathrm{sign}\left(x - \lambda_- + \omega\right)}{\sqrt{\omega^2 - q^2}\sqrt{\frac{q^2}{4}\left(1 + \frac{4\lambda_+^2}{q^2-\omega^2}\right) - (x + \frac{\omega}{2} + \lambda_+)^2}} \\
- \frac{\sqrt{\omega_-^2 - q^2}\sqrt{\frac{q^2}{4}\frac{\left(q^2-\omega_+^2+4\lambda_I^2\right)\left(q^2-\omega_+^2+4\lambda_R^2\right)}{\left(q^2-\omega_+^2\right)^2} - \left(x + \frac{\omega_+}{2}\left(1 + \frac{4\lambda_R\lambda_I}{q^2-\omega_+^2}\right) + \lambda_+\right)^2}}{4x(x+\omega)} \times \\
\times\,\mathrm{sign}\left(x + \lambda_+ + \omega\right)\Bigg] \\
- \left(\omega \to -\omega\right)\Bigg\}.
\end{aligned} \tag{A.32}$$

The result can be written as

$$\begin{aligned}\mathrm{Im}\left\{\delta\chi_{k_{F-}}(q,\omega)\right\} = \frac{g_v}{2\pi\omega}\,\mathrm{Re}\Big\{ & \frac{1}{i}\hat{\mathcal{R}}_1^{\omega}\left(-\lambda_+ - \omega\right)\Big|_{\epsilon}^{\mu-\lambda_I} - \frac{1}{i}\hat{\mathcal{R}}_1^{\omega}\left(-\lambda_+\right)\Big|_{\omega}^{\mu-\lambda_I+\omega} \\ & -\frac{1}{i}\theta\left[-\omega\right]\theta\left[\mu-\lambda_I+\omega\right]\mathrm{sign}\left(\lambda_+\right)\left[R_1^{\omega}(-\epsilon) - R_1^{\omega}(\epsilon)\right] \\ & + i\hat{\mathcal{R}}_2^{\omega}\left(\lambda_- - \omega\right)\Big|_{\epsilon}^{\mu-\lambda_I} - i\hat{\mathcal{R}}_2^{\omega}\left(\lambda_-\right)\Big|_{\omega}^{\mu-\lambda_I+\omega} \\ & - i\theta\left[-\omega\right]\theta\left[\mu-\lambda_I+\omega\right]\mathrm{sign}\left(-\lambda_-\right)\left[R_2^{\omega}(-\epsilon) - R_2^{\omega}(\epsilon)\right]\Big\} \\ & - \left(\omega \to -\omega\right). \end{aligned} \tag{A.33}$$

The limit $\epsilon \to 0$ in Eqs. (A.22) and (A.33) can now be taken safely giving finite results.

B

Appendix B.

Details on the calculation of the current susceptibility of graphene

Appendix B presents details on the calculation of the transversal part of the current-current susceptibility. We start with the imaginary part in Sec. B.1, followed by the real part in Sec. B.2. For brevity, we set $v_F = 1$ throughout the chapter.

We notice that Eq. (5.6) can be written as

$$\chi^0_{\boldsymbol{j}_x\boldsymbol{j}_x}(\boldsymbol{q},\omega) = \xi^+_\mu(\boldsymbol{q},\omega) + \xi^-_\mu(\boldsymbol{q},\omega) - \xi^-_D(\boldsymbol{q},\omega), \tag{B.1}$$

where

$$\xi^\pm_\Lambda(\boldsymbol{q},\omega) = g_v g_s \int \frac{d^2k}{(2\pi)^2}\,\frac{1}{2}\left(1 \mp \frac{\lambda_I^2 - k^2\left(1-2\sin^2\phi_k\right) - qk\cos\left(\phi_k+\phi_q\right)}{E_g(k)E_g(|\boldsymbol{k}+\boldsymbol{q}|)}\right)\times$$
$$\times\left(\frac{1}{\omega \mp E_g(|\boldsymbol{k}+\boldsymbol{q}|) + E_g(k) + i0} - \frac{1}{\omega \pm E_g(|\boldsymbol{k}+\boldsymbol{q}|) - E_g(k) + i0}\right)\theta\left[\Lambda^2 - \lambda_I^2 - k^2\right]. \tag{B.2}$$

D is a cutoff parameter, $\tan\phi_k = k_y/k_x$ ($\tan\phi_q = q_y/q_x$) the in-plane angle, $g_v = g_s = 2$ the valley and spin degeneracy factors, and $E_g = \sqrt{k^2+\lambda_I^2}$ the energy of gapped graphene. The plus (minus) sign in Eq. (B.2) corresponds to the initial and final bands being equal (not equal). For the longitudinal case ($\boldsymbol{q} = q\,\boldsymbol{e}_x$), we get

$$\cos\left(\phi_k+\phi_q\right) = \cos\phi_k, \tag{B.3}$$

whereas the overlap for the transversal part ($\boldsymbol{q} = q\,\boldsymbol{e}_y$) is given by

$$\cos\left(\phi_k+\phi_q\right) = -\sin\phi_k. \tag{B.4}$$

B.1. Imaginary part

Using the Dirac identity in Eq. (3.8), the above integral for the imaginary part of the transversal current-current susceptibility simplifies considerable. We define the expression

$$\begin{aligned} I_{\Lambda}^{\rho\nu} &= \frac{g_v g_s}{8\pi} \int_0^{\sqrt{\Lambda^2-\lambda_I^2}} dk k \int_0^{2\pi} d\phi_k \left[1 - \rho \frac{\lambda_I^2 - k^2\left(1-2\sin^2\phi_k\right) + qk\sin\phi_k}{E_g(k) E_g\left(|\boldsymbol{k}+\boldsymbol{q}|\right)}\right] \times \\ &\qquad \times \delta\left[\nu\omega - E_g(k) + \rho E_g\left(|\boldsymbol{k}+\boldsymbol{q}|\right)\right] \\ &= \frac{g_v g_s \rho \sqrt{\omega^2-q^2}}{16\pi}\, \theta\left[1 - \left|\frac{\omega^2 - q^2 - 2\nu\omega E_g(k)}{2qk}\right|\right] \times \begin{cases} G_<^+\left(\frac{2\sqrt{k^2+\lambda_I^2}-\nu\omega}{q}\right) & \text{for } \omega > q \\ G_>^+\left(\frac{2\sqrt{k^2+\lambda_I^2}-\nu\omega}{q}\right) & \text{for } q > \omega \end{cases}. \end{aligned} \tag{B.5}$$

The functions $G_{>,<,0}^{\pm}$ are defined as [99]

$$G_<^{\pm} = x\sqrt{x_0^2 - x^2} \pm \left(2 - x_0^2\right) \arccos\left(\frac{x}{x_0}\right), \tag{B.6a}$$

$$G_>^{\pm} = x\sqrt{x^2 - x_0^2} \pm \left(2 - x_0^2\right) \operatorname{arccosh}\left(\frac{x}{x_0}\right), \tag{B.6b}$$

$$G_0^{\pm} = x\sqrt{x^2 - x_0^2} \pm \left(2 - x_0^2\right) \operatorname{arcsinh}\left(\frac{x}{|x_0|}\right), \tag{B.6c}$$

and x_0 reads

$$x_0 = \sqrt{1 + \frac{\lambda_I^2}{q^2 - \omega^2}}. \tag{B.7}$$

The imaginary part for undoped graphene is now given by

$$\operatorname{Im}\left\{\chi_{jj}^{0,T,un}(q,\omega)\right\} = \lim_{D\to\infty}\left[I_D^{--} - I_D^{-+}\right] = -\frac{g_v g_s \sqrt{\omega^2-q^2}}{16}\left(1 + \frac{4\lambda_I^2}{\omega^2-q^2}\right)\theta\left[\omega^2 - q^2 - \lambda_I^2\right]. \tag{B.8}$$

In the doped case the upper integration limit is not a cutoff but the Fermi wave vector. Therefore, in the above integral we need to distinguish whether k is larger than k_F or not. For this we define different regions given in Table 5.1 and shown in Fig. 5.1 for the special case of $\lambda_I = 0.9\mu$; see also Ref. [99]. The intraband contribution to the imaginary part

then reads

$$\mathrm{Im}\left\{\delta\chi_{jj}^{0,T,do}\left(q,\omega\right)\right\}=\sum_{\rho,\nu=\pm1}\nu I_{\mu}^{\rho\nu}=-\frac{g_v g_s\sqrt{|\omega^2-q^2|}}{16\pi}\begin{cases}G_{>}^{+}\left(\frac{2\mu+\omega}{q}\right)-G_{>}^{+}\left(\frac{2\mu-\omega}{q}\right) & \text{1A}\\ -\pi\left(1+\frac{4\lambda_I^2}{\omega^2-q^2}\right) & \text{1B}\\ G_{>}^{+}\left(\frac{2\mu+\omega}{q}\right) & \text{2A}\\ G_{<}^{+}\left(\frac{2\mu-\omega}{q}\right)-\pi\left(1+\frac{4\lambda_I^2}{\omega^2-q^2}\right) & \text{2B}\\ 0 & \text{3A}\\ 0 & \text{3B}\\ 0 & \text{4A}\\ 0 & \text{4B}\\ 0 & \text{5B}\end{cases}. \tag{B.9}$$

Adding now the intrinsic part in Eq. (B.8) yields the final result of Eq. (5.11).

B.2. Real part

The simplest way to get the real part of the undoped susceptibility is via Eq. (3.9):

$$\begin{aligned}\mathrm{Re}\left\{\chi_{jj}^{0,T,un}\left(q,\omega\right)\right\}&=\frac{2}{\pi}\mathcal{P}\int_0^D d\omega'\frac{\omega'\,\mathrm{Im}\left\{\chi_{jj}^{0,T,un}\left(q,\omega'\right)\right\}}{\omega'^2-\omega^2}\\ &=-\frac{g_v g_s\left(D-2\lambda_I\right)}{8\pi}-\frac{g_v g_s\left(4\lambda_I^2-q^2+\omega^2\right)}{16\pi\sqrt{|q^2-\omega^2|}}\times\\ &\quad\times\left[\theta\left[q-\omega\right]\arccos\left(\frac{q^2-\omega^2-4\lambda_I^2}{\omega^2-q^2-4\lambda_I^2}\right)-\theta\left[\omega-q\right]\ln\frac{\left(2\lambda_I+\sqrt{\omega^2-q^2}\right)^2}{|\omega^2-q^2-4\lambda_I^2|}\right].\end{aligned} \tag{B.10}$$

Notice the cutoff-dependent part on the right-hand side due to the anomalous commutator; see also the discussion in Sec. 3.1.

To obtain the real part of doped graphene we start from Eq. (B.2):

$$\mathrm{Re}\left\{\delta\chi_{jj}^{0,T,do}\left(q,\omega\right)\right\}=\frac{g_v g_s}{2(2\pi)^2}\sum_{\nu=\pm1}\int_0^{k_F}dkk\int_0^{2\pi}d\phi_k\left(1-\nu\frac{\lambda_I^2-k^2\left(1-2\sin^2\phi_k\right)+qk\sin\phi_k}{E_g(k)E_g(|\boldsymbol{k}+\boldsymbol{q}|)}\right)\times$$
$$\times\left[\frac{1}{\omega+E_g(k)-\nu E_g(|\boldsymbol{k}+\boldsymbol{q}|)}-\frac{1}{\omega-E_g(k)+\nu E_g(|\boldsymbol{k}+\boldsymbol{q}|)}\right]$$

$$= \frac{g_v g_s \omega^2 (\mu - \lambda_I)}{2\pi q^2} + \frac{g_v g_s \sqrt{|\omega^2 - q^2|}}{16\pi} \times$$
$$\times \sum_{\nu=\pm 1} \text{sign}\left(\frac{q^2-\omega^2}{2\omega} - \nu E_g(k)\right) \begin{cases} \left[G^+_< \left(\frac{2E_g(k)+\nu\omega}{q}\right)\right]_{k_{low}}^{k_{up}} & \text{for } q^2 > \omega^2 \\ \left[G^+_> \left(\frac{2E_g(k)+\nu\omega}{q}\right)\right]_{k_{low}}^{k_{up}} & \text{for } \omega^2 > 4\lambda_I^2 + q^2 \\ \left[G^+_0 \left(\frac{2E_g(k)+\nu\omega}{q}\right)\right]_{k_{low}}^{k_{up}} & \text{for } q^2 < \omega^2 < 4\lambda_I^2 + q^2 \end{cases}, \tag{B.11}$$

where the limits k_{low} and k_{up} are determined by the condition

$$\left(\frac{q^2 - \omega^2 - 2\nu\omega E_g(k)}{2qk}\right)^2 > 1. \tag{B.12}$$

The intraband part of the susceptibility thus reads

$$\text{Re}\left\{\delta\chi^{0,T,do}_{jj}(q,\omega)\right\} = \frac{g_v g_s \omega^2 (\mu - \lambda_I)}{2\pi q^2}$$
$$- \frac{g_v g_s \sqrt{|\omega^2 - q^2|}}{16\pi} \begin{cases} G^+_<\left(\frac{2\lambda_I-\omega}{q}\right) + \text{sign}\left(\frac{q^2-\omega^2}{2\omega} - \lambda_I\right) G^+_<\left(\frac{2\lambda_I+\omega}{q}\right) & \text{A} \\ \text{sign}\left(\frac{q^2-\omega^2}{2\omega} + \lambda_I\right) G^+_>\left(\frac{2\lambda_I-\omega}{q}\right) - G^+_>\left(\frac{2\lambda_I+\omega}{q}\right) & \text{1-4 B} \\ G^+_0\left(\frac{2\lambda_I-\omega}{q}\right) - G^+_0\left(\frac{2\lambda_I+\omega}{q}\right) & \text{5B} \end{cases}$$
$$- \frac{g_v g_s \sqrt{|\omega^2 - q^2|}}{16\pi} \begin{cases} 0 & \text{1A} \\ G^+_>\left(\frac{2\mu+\omega}{q}\right) - G^+_>\left(\frac{2\mu-\omega}{q}\right) & \text{1B} \\ -G^+_<\left(\frac{2\mu-\omega}{q}\right) & \text{2A} \\ G^+_>\left(\frac{2\mu+\omega}{q}\right) & \text{2B} \\ -G^+_<\left(\frac{2\mu-\omega}{q}\right) - G^+_<\left(\frac{2\mu+\omega}{q}\right) & \text{3A} \\ G^+_>\left(\frac{2\mu+\omega}{q}\right) - G^+_>\left(\frac{-2\mu+\omega}{q}\right) & \text{3B} \\ -G^+_<\left(\frac{2\mu-\omega}{q}\right) + G^+_<\left(\frac{2\mu+\omega}{q}\right) & \text{4A} \\ G^+_>\left(\frac{-2\mu+\omega}{q}\right) + G^+_>\left(\frac{2\mu+\omega}{q}\right) & \text{4B} \\ G^+_0\left(\frac{2\mu+\omega}{q}\right) - G^+_0\left(\frac{2\mu-\omega}{q}\right) & \text{5B} \end{cases}. \tag{B.13}$$

Adding the interband part Eq. (B.10) yields the final result given by Eq. (5.12).

Bibliography

[1] E. Osawa, Kagaku **25**, 854 (1970); Z. Yoshida and E. Osawa, Kagaku Dojin **22**, 174 (1971).

[2] H. W. Kroto, J. R. Heath, S. C. O'Brien, R. F. Curl, and R. E. Smalley, Nature **318**, 162 (1985).

[3] Official web site of the Nobel Prize: http://www.nobelprize.org/nobel_prizes/chemistry/laureates/1996/ (as of September 2013).

[4] Official web site of Wikipedia: http://de.wikipedia.org/wiki/Fullerene (as of September 2013).

[5] S. Iijima, Nature **354**, 56 (1991).

[6] M. F. L. De Volder, S. H. Tawfick, R. H. Baughman, and A. J. Hart, Science **339**, 535 (2013).

[7] L. D. Landau, Phys. Z. Sowjetunion **11**, 26 (1937).

[8] N. D. Mermin and H. Wagner, Phys. Rev. Lett. **17**, 1133 (1966).

[9] K. S. Novoselov, A. K. Geim, S. V. Morozov, D. Jiang, Y. Zhang, S. V. Dubonos, I. V. Grigorieva, and A. A. Firsov, Science **306**, 666 (2004).

[10] H.-P. Boehm, A. Clauss, G. O. Fischer, and U. Hofmann, Z. Anorg. Allg. Chem. **316**, 119 (1962); Z. Naturforsch. B **17**, 150 (1962).

[11] H.-P. Boehm, Angew. Chem. **122**, 9520 (2010).

[12] A. H. Castro Neto, F. Guinea, N. M. R. Peres, K. S. Novoselov, and A. K. Geim, Rev. Mod. Phys. **81**, 109 (2009).

[13] K. S. Novoselov, Rev. Mod. Phys. **83**, 837 (2011).

[14] P. R. Wallace, Phys. Rev. **71**, 622 (1947).

[15] A. K. Geim and K. S. Novoselov, Nat. Mat. **6**, 183 (2007).

[16] Official web site of the Nobel Prize: http://www.nobelprize.org/nobel_prizes/physics/laureates/2010/ (as of September 2013).

[17] Official web site of the Graphene Flagship project: http://www.graphene-flagship.eu/ (as of September 2013).

[18] K. S. Novoselov, D. Jiang, F. Schedin, T. J. Booth, V. V. Khotkevich, S. V. Morozov, and A. K. Geim, Proc. Natl. Acad. Sci. U.S.A. **102**, 10451 (2005).

[19] K. F. Mak, C. Lee, J. Hone, J. Shan, and T. F. Heinz, Phys. Rev. Lett. **105**, 136805 (2010).

[20] B. Aufray, A. Kara, S. Vizzini, H. Oughaddou, C. Léandri, B. Ealet, and G. Le Lay, Appl. Phys. Lett. **96**, 183102 (2010).

[21] B. Lalmi, H. Oughaddou, H. Enriquez, A. Kara, S. Vizzini, B. Ealet, and B. Aufray, Appl. Phys. Lett. **97**, 223109 (2010).

[22] J. O. Sofo, A. S. Chaudhari, and G. D. Barber, Phys. Rev. B **75**, 153401 (2007).

[23] D. C. Elias, R. R. Nair, T. M. G. Mohiuddin, S. V. Morozov, P. Blake, M. P. Halsall, A. C. Ferrari, D. W. Boukhvalov, M. I. Katsnelson, A. K. Geim, and K S. Novoselov, Science **323**, 610 (2009).

[24] M. Gmitra, D. Kochan, and J. Fabian, Phys. Rev. Lett. **110**, 246602 (2013).

[25] K. A. Worsley, P. Ramesh, S. K. Mandal, S. Niyogi, M. E. Itkis, and R. C. Haddon, Chem. Phys. Lett. **445**, 51 (2007).

[26] S.-H. Cheng, K. Zou, F. Okino, H. R. Gutierrez, A. Gupta, N. Shen, P. C. Eklund, J. O. Sofo, and J. Zhu, Phys. Rev. B **81**, 205435 (2010).

[27] T. Ando, J. Phys. Soc. Jpn. **76**, 024712 (2007).

[28] R. R. Nair, P. Blake, A. N. Grigorenko, K. S. Novoselov, T. J. Booth, T. Stauber, N. M. R. Peres, and A. K. Geim, Science **320**, 1308 (2008).

[29] M. Jablan, H. Buljan, and M. Soljačić, Phys. Rev. B **80**, 245435 (2009).

[30] F. H. L. Koppens, D. E. Chang, and F. J. García de Abajo, Nano Lett. **11**, 3370 (2011).

[31] L. Ju, B. Geng, J. Horng, C. Girit, M. Martin, Z. Hao, H. A. Bechtel, X. Liang, A. Zettl, Y. R. Shen, and F. Wang, Nat. Nano. **6**, 630 (2011).

[32] J. Chen, M. Badioli, P. Alonso-González, S. Thongrattanasiri, F. Huth, J. Osmond, M. Spasenović, A. Centeno, A. Pesquera, P. Godignon, A. Z. Elorza, N. Camara, F. J. García de Abajo, R. Hillenbrand, and F. H. L. Koppens, Nature **487**, 77 (2012).

[33] Z. Fei, A. S. Rodin, G. O. Andreev, W. Bao, A. S. McLeod, M. Wagner, L. M. Zhang, Z. Zhao, M. Thiemens, G. Dominguez, M. M. Fogler, A. H. Castro Neto, C. N. Lau, F. Keilmann, and D. N. Basov, Nature **487**, 82 (2012).

[34] Q. Bao and K. P. Loh, Nano **6**, 3677 (2012).

[35] A. N. Grigorenko, M. Polini, and K. S. Novoselov, Nat. Phot. **6**, 749 (2012).

[36] Y. V. Bludov, A. Ferreira, N. M. R. Peres, and M. I. Vasilevskiy, Int. J. Mod. Phys. B **27**, 1341001 (2013).

[37] P. M. Krstajić and F. M. Peeters, Phys. Rev. B **85**, 205454 (2012).

[38] A. Bostwick, F. Speck, T. Seyller, K. Horn, M. Polini, R. Asgari, A. H. MacDonald, and E. Rotenburg, Science **328**, 999 (2010).

[39] A. L. Walter, A. Bostwick, K.-J. Jeon, F. Speck, M. Ostler, T. Seyller, L. Moreschini, Y. J. Chang, M. Polini, R. Asgari, A. H. MacDonald, K. Horn, and E. Rotenberg, Phys. Rev. B **84**, 085410 (2011).

[40] M. Gmitra, S. Konschuh, C. Ertler, C. Ambrosch-Draxl, and J. Fabian, Phys. Rev. B **80**, 235431 (2009).

[41] Y. S. Dedkov, M. Fonin, U. Rüdiger, and C. Laubschat, Phys. Rev. Lett. **100**, 107602 (2008).

[42] A. Varykhalov, J. Sánchez-Barriga, A. M. Shikin, C. Biswas, E. Vescovo, A. Rybkin, D. Marchenko, and O. Rader, Phys. Rev. Lett. **101**, 157601 (2008).

[43] A. H. Castro Neto and F. Guinea, Phys. Rev. Lett. **103**, 026804 (2009).

[44] C. Weeks, J. Hu, J. Alicea, M. Franz, and R. Wu, Phys. Rev. X **1**, 021001 (2011).

[45] D. Ma, Z. Li, and Z. Yang, Carbon **50**, 297 (2012).

[46] C.-C. Liu, H. Jiang, and Y. Yao, Phys. Rev. B **84**, 195430 (2011).

[47] L. Chen, C.-C. Liu, B. Feng, X. He, P. Cheng, Z. Ding, S. Meng, Y. Yao, and K. Wu, Phys. Rev. Lett. **109**, 056804 (2012).

[48] B. Radisavljevic, A. Radenovic, J. Brivio, V. Giacometti, and A. Kis, Nat. Nano. **6**, 147 (2011).

[49] D. Xiao, W. Yao, and Q. Niu, Phys. Rev. Lett. **99**, 236809 (2007).

[50] T. Cao, G. Wang, W. Han, H. Ye, C. Zhu, J. Shi, Q. Niu, P. Tan, E. Wang, B. Liu, and J. Feng, Nat. Commun. **3**, 887 (2012).

[51] H. Zeng, J. Dai, W. Yao, D. Xiao, and X. Cui, Nat. Nano. **7**, 490 (2012).

[52] J. Klinovaja and D. Loss, Phys. Rev. B **88**, 075404 (2013).

[53] D. Xiao, G.-B. Liu, W. Feng, X. Xu, and W. Yao, Phys. Rev. Lett. **108**, 196802 (2012).

[54] H. Rostami, A. G. Moghaddam, and R. Asgari, Phys. Rev. B **88**, 085440 (2013).

[55] A. Kormányos, V. Zólyomi, N. D. Drummond, P. Rakyta, G. Burkard, and V. I. Fal'ko, Phys. Rev. B **88**, 045416 (2013).

[56] R. Winkler, *Spin-Orbit Coupling Effects in Two-Dimensional Electron and Hole Systems*, Springer, Berlin Heidelberg, 2003.

[57] For an overview on spintronics see: I. Žutić, J. Fabian, and S. Das Sarma, Rev. Mod. Phys. **76**, 323 (2004); J. Fabian, A. Matos-Abiague, C. Ertler, P. Stano, and I. Žutić, Acta Phys. Slov. **57**, 565 (2007); M. W. Wu, J. H. Jiang, and M. Q. Weng, Phys. Rep. **493**, 61 (2010).

[58] Y. Liu, R. F. Willis, K. V. Emtsev, and T. Seyller, Phys. Rev. B **78**, 201403(R) (2008).

[59] S. Y. Shin, C. G. Hwang, S. J. Sung, N. D. Kim, H. S. Kim, and J. W. Chung, Phys. Rev. B **83**, 161403(R) (2011).

[60] M. Koshino and T. Ando, Phys. Rev. B **81**, 195431 (2010).

[61] B. Wunsch, T. Stauber, F. Sols, and F. Guinea, New J. Phys. **8**, 318 (2006).

[62] E. H. Hwang and S. Das Sarma, Phys. Rev. B **75**, 205418 (2007).

[63] F. Stern, Phys. Rev. Lett. **18**, 546 (1967).

[64] C. Li and X. G. Wu, Appl. Phys. Let. **93**, 251501 (2008).

[65] S. M. Badalyan, A. Matos-Abiague, G. Vignale, and J. Fabian, Phys. Rev. B **79**, 205305 (2009).

[66] T. Oka and H. Aoki, Phys. Rev. B **79**, 081406 (R) (2009).

[67] H. L. Calvo, H. M. Pastawski, S. Roche, and L. E. F. Foa Torres, Appl. Phys. Lett. **98**, 232103 (2011).

[68] Y. Zhou and M. W. Wu, Phys. Rev. B **83**, 245436 (2011).

[69] R. Saito, G. Dresselhaus, and M. S. Dresselhaus, *Physical Properties of Carbon Nanotubes*, Imperial College Press, London, 1998.

[70] F. Schwabl, *Quantum Mechanics*, Springer, Berlin Heidelberg, 2002.

[71] C. L. Kane and E. J. Mele, Phys. Rev. Lett. **95**, 226801 (2005).

[72] H. Min, J. E. Hill, N. A. Sinitsyn, B. R. Sahu, L. Kleinman, and A. H. MacDonald, Phys. Rev. B **74**, 165310 (2006).

[73] S. Konschuh, M. Gmitra, and J. Fabian, Phys. Rev. B **82**, 245412 (2010).

[74] Y. Yao, F. Ye, X.-L Qi, S.-C. Zhang, and Z. Fang, Phys. Rev. B **75**, 041401(R) (2007).

[75] S. Abdelouahed, A. Ernst, J. Henk, I. V. Maznichenko, and I. Mertig, Phys. Rev. B **82**, 125424 (2010).

[76] E. McCann and M. Koshino, Rep. Prog. Phys. **76**, 056503 (2013).

[77] E. Cappelluti, R. Roldán, J. A. Silva-Guillén, P. Ordejón, and F. Guinea, Phys. Rev. B **88**, 075409 (2013).

[78] K. Kośminder and J. Fernández-Rossier, Phys. Rev. B **87**, 075451 (2013).

[79] H. Peelaers and C. G. Van de Walle, Phys. Rev. B **86**, 241401(R) (2012).

[80] B. Radisavljevic and A. Kis, Nat. Mat. **12**, 815 (2013).

[81] T. Stauber, J. Schliemann, and N. M. R. Peres, Phys. Rev. B **81**, 085409 (2010).

[82] D. J. Chadi and M. L. Cohen, Phys. Stat. Sol. B **68**, 405 (1975).

[83] P. Y. Yu and M. Cardona, *Fundamentals of Semiconductors: Physics and Materials Properties*, Springer, Berlin Heidelberg, 2005.

[84] J. M. Luttinger, Phys. Rev. **102**, 1030 (1956).

[85] A. Matos-Abiague, personal notes.

[86] E. O. Kane, J. Phys. Chem. Solids **1**, 249 (1957).

[87] The Semiconductors-Information web site:
http://www.semiconductors.co.uk/propiiiv5653.htm (as of September 2013).

[88] J. Schliemann, Phys. Rev. B **74**, 045214 (2006); Europhys. Lett. **91**, 67004 (2010); Phys. Rev. B **84**, 155201 (2011).

[89] G. Dresselhaus, Phys. Rev. **100**, 580 (1955).

[90] Y. A. Bychkov and E. I. Rashba, JETP Lett. **39**, 78 (1984).

[91] G. F. Giuliani and G. Vignale, *Quantum Theory of the Electron Liquid*, Cambridge University Press, Cambridge, 2005.

[92] H. Bruus and K. Flensberg, *Many-Body Quantum Theory in Condensed Matter Physics*, Oxford University Press, Oxford, 2004.

[93] T. Frederiksen, M. Paulsson, M. Brandbyge, and A.-P. Jauho, Phys. Rev. B **75**, 205413 (2007).

[94] J. Sabio, J. Nilsson, and A. H. Castro Neto, Phys. Rev. B **78**, 075410 (2008).

[95] S. H. Abedinpour, G. Vignale, A. Principi, M. Polini, W.-K. Tse, and A. H. MacDonald, Phys. Rev. B **84**, 045429 (2011).

[96] T. Stauber and G. Gómez-Santos, Phys. Rev. B **82**, 155412 (2010).

[97] R. Sensarma, E. H. Hwang, and S. Das Sarma, Phys. Rev. **B** 82, 195428 (2010).

[98] Official web site of Wikipedia: http://en.wikipedia.org/wiki/High_resolution_electron_energy_loss_spectroscopy (as of September 2013).

[99] P. K. Pyatkovskiy, J. Phys.: Condens. Mat. **21**, 025506 (2009).

[100] O. V. Gamayun, Phys. Rev. B **84**, 085112 (2011).

[101] S. Yuan, R. Roldán, and M. I. Katsnelson, Phys. Rev. B **84**, 035439 (2011).

[102] M. Busl, G. Platero, and A.-P. Jauho, Phys. Rev. B **85**, 155449 (2012).

[103] S. Gangadharaiah, A. M. Farid, and E. G. Mishchenko, Phys. Rev. Lett. **100**, 166802 (2008).

[104] X.-F. Wang and T. Chakraborty, Phys. Rev. B **75**, 041404(R) (2007).

[105] M. J. Lighthill, *Introduction to Fourier Analysis and Generalized Functions*, Cambridge University Press, Cambridge, 1958.

[106] T. Ando, J. Phys. Soc. Jpn. **75**, 074716 (2006).

[107] G. Gómez-Santos and T. Stauber, Phys. Rev. Lett. **106**, 045504 (2011).

[108] H. Fukuyama, J. Phys. Soc. Jpn. **76**, 043711 (2007).

[109] J. W. McClure, Phys. Rev. **104**, 666 (1956).

[110] S. G. Sharapov, V. P. Gusynin, and H. Beck, Phys. Rev. B **69**, 075104 (2004).

[111] A. Principi, M. Polini, and G. Vignale, Phys. Rev. B **80**, 075418 (2009).

[112] A. Principi, M. Polini, G. Vignale, and M. I. Katsnelson, Phys. Rev. Lett. **104**, 225503 (2010).

[113] S. Y. Zhou, G.-H. Gweon, A. V. Fedorov, P. N. First, W. A. de Heer, D.-H. Lee, F. Guinea, A. H. Castro Neto, and A. Lanzara, Nat. Mat. **6**, 770 (2007).

[114] Y. Yoon, K. Ganapathi, and S. Salahuddin, Nano Lett. **11**, 3768 (2011).

[115] M.-W. Lin, L. Liu, Q. Lan, X. Tan, K. S. Dhindsa, P. Zeng, V. M. Naik, M. M.-C. Cheng, and Z. Zhou, J. Phys. D: Appl. Phys. **45**, 345102 (2012).

[116] J. Schliemann, J. C. Egues, and D. Loss, Phys. Rev. Lett. **90**, 146801 (2003).

[117] F. V. Kyrychenko and C. A. Ullrich, Phys. Rev. B **83**, 205206 (2011).

[118] S. M. Badalyan, C. S. Kim, and G. Vignale, Phys. Rev. Lett. **100**, 016603 (2008).

[119] O. Betbeder-Matibet, M. Combescot, and C. Tanguy, Phys. Rev. B **53**, 12929 (1996).

[120] T. Kernreiter, M. Governale, R. Winkler, and U. Zülicke, Phys. Rev. B **88**, 125309 (2013).

[121] C. Schüller, J. Kraus, G. Schaack, G. Weimann, and K. Panzlaff, Phys. Rev. B **50**, 18387 (1994).

[122] S.-J. Cheng and R. R. Gerhardts, Phys. Rev. B **63**, 035314 (2001).

[123] P. Delplace, Á. Gómez-León, and G. Platero, arXiv:1304.6272 (2013).

[124] N. H. Lindner, G. Refael, and V. Galitski, Nat. Phys. **7**, 490 (2011).

[125] J. Schliemann, D. Loss, and R. M. Westervelt, Phys. Rev. Lett. **94**, 206801 (2005); Phys. Rev. B **73**, 085323 (2006).

[126] J. Cserti and G. Dávid, Phys. Rev. B **74**, 172305 (2006); Phys. Rev. B **81**, 121417(R) (2010).

[127] J. Schliemann, Phys. Rev. B **75**, 045304 (2007); New J. Phys. **10**, 043024 (2008).

[128] B. Trauzettel, Y. M. Blanter, and A. F. Morpurgo, Phys. Rev. B **75**, 035305 (2007).

[129] L. D. Landau and E. M. Lifshitz, *Classical Theory of Fields*, Butterworth-Heinemann, London, 1987.

[130] M. Grifoni and P. Hänggi, Phys. Rep. **304**, 229 (1998).

[131] S. Kohler, J. Lehmann, and P. Hänggi, Phys. Rep. **406**, 379 (2005).

[132] J. H. Shirley, Phys. Rev. **138**, B979 (1965).

[133] F. H. M. Faisal and J. Z. Kamiński, Phys. Rev. A **54**, R1769 (1996); Phys. Rev. A **56**, 748 (1997).

[134] A. K. Gupta, O. E. Alon, and N. Moiseyev, Phys. Rev. B **68**, 205101 (2003).

[135] H. Hsu and L. E. Reichl, Phys. Rev. **B** 74, 115406 (2006).

[136] J. Schliemann, personal notes.

[137] A. López, Z. Z. Sun, and J. Schliemann, Phys. Rev. B **85**, 205428 (2012).

[138] Y. Zhou and M. W. Wu, arXiv:1206.4093 (2012).

[139] A. López, A. Scholz, Z. Z. Sun, and J. Schliemann, Eur. Phys. J. B **86**, 366 (2013).

[140] A. Mysyrowicz, D. Hulin, A. Antonetti, A. Migus, W. T. Masselink, and H. Morkoc, Phys. Rev. Lett. **56**, 2748 (1986).

[141] E. Suárez Morell and L. E. F. Foa Torres, Phys. Rev. B **86**, 125449 (2012).

[142] T. Stauber, N. M. R. Peres, and A. K. Geim, Phys. Rev. B **78**, 085432 (2008).

[143] P. Ingenhoven, J. Z. Bernád, U. Zülicke, and R. Egger, Phys. Rev. B **81**, 035421 (2010).

[144] K. Nakada, M. Fujita, G. Dresselhaus, and M. S. Dresselhaus, Phys. Rev. B **54**, 17954 (1996).

[145] P. Recher, B. Trauzettel, A. Rycerz, Y. M. Blanter, C. W. J. Beenakker, and A. F. Morpurgo, Phys. Rev. B **76**, 235404 (2007).

[146] I. S. Gradshteyn and I. M. Ryzhik, *Table of Integrals, Series, and Products*, Academic Press, London, 2000.

List of publications

(i) A. Scholz and J. Schliemann,
Dynamical current-current susceptibility of gapped graphene,
Phys. Rev. B **83**, 235409 (2011).

(ii) A. Scholz, T. Stauber, and J. Schliemann,
Dielectric function, screening, and plasmons of graphene in the presence of spin-orbit interactions,
Phys. Rev. B **86**, 195424 (2012).

(iii) A. Scholz, T. Dollinger, P. Wenk, K. Richter, and J. Schliemann,
Plasmons in spin-orbit coupled two-dimensional hole gas systems,
Phys. Rev. B **87**, 085321 (2013).

(iv) A. Scholz, A. López, and J. Schliemann,
Interplay between spin-orbit interactions and a time-dependent electromagnetic field in monolayer graphene,
Phys. Rev. B **88**, 045118 (2013).

(v) A. Scholz, T. Stauber, and J. Schliemann,
Plasmons and screening in a monolayer of MoS_2,
Phys. Rev. B **88**, 035135 (2013).

(vi) T. Dollinger, A. Scholz, P. Wenk, R. Winkler, J. Schliemann, and K. Richter,
Signatures of spin-preserving symmetries in two-dimensional hole gases,
arXiv:1304.7747 (2013).

(vii) A. López, A. Scholz, Z. Z. Sun, and J. Schliemann,
Graphene with time-dependent spin-orbit coupling: Truncated Magnus expansion approach,
Eur. Phys. J. B **86**, 366 (2013).

Acknowledgment

At this point, I would like to take the opportunity to thank a few people, without whose help and support this thesis would not exist.

First of all, I thank my supervisor Prof. Dr. John Schliemann for guiding me during my diploma thesis and PhD, for providing me with a variety of interesting research projects, but at the same time giving me the freedom to investigate problems I considered as being interesting. Moreover, I thank Prof. Dr. Schliemann for giving me possibility to attend to a number of conferences and summer schools, to the Lindau Nobel Laureate Meeting 2012, and to go for a research stay to Madrid in January 2012.

My gratitude also goes to Dr. Tobias Stauber for his longstanding collaboration with us, resulting in two joint publications. I appreciate that Dr. Stauber gave me his *Fortran* code to calculate the free polarizability of the honeycomb lattice of graphene, for inviting me to a research stay at his home university, Universidad Autonoma de Madrid, and for a variety of very useful discussions and comments.

I thank Tobias Dollinger, Dr. Alexander López, Prof. Dr. Klaus Richter, and Dr. Paul Wenk for a fruitful collaboration in the context of the SFB 689 and the GRK 1570, respectively.

For proofreading the thesis I want to express my deepest gratitude to Dr. Alexander López and Donald Wayne Rummage.

I am very grateful to Dr. Tyler Cocker, Max Eisele, Prof. Dr. Rupert Huber, Prof. Dr. Guillermo Gómez-Santos, and Priv.-Doz. Dr. Tobias Korn for informative discussions on graphene- and MoS_2-based plasmonics. I thank Dr. Maria Busl, Prof. Dr. Milena Grifoni, Dr. Sigmund Kohler, and Prof. Dr. Ming-Wei Wu for useful information regarding driven quantum systems. Furthermore, I appreciate helpful discussions about spin physics and beyond with Dr. Alex Matos-Abiague and Prof. Dr. Francisco Mireless.

Support regarding all kinds of administrative issues is gratefully acknowledged from Ulla Franzke, Robert Hrdina, and Lizy Lazar.

I thank Jan Bundesmann, Dr. Björn Erbe, Dr. Carlos López-Monis, Sebastian Pfaller, Dr. Prakash Parida, Dr. Martin Raith, Sascha Ratz, Benjamin Siegert, Dr. Maxim Trushin, and the other members the Condensed Matter Theory for the pleasant working atmosphere.

Due to my position as a system administrator I had the pleasure to work with and learn from a variety of people. Therefore, I am deeply grateful for support from my colleagues Dr. Manohar Awasthi, Jan Bundesmann, Tobias Dollinger, Sven Essert, Timo Hartmann, Dr. Michael Hartung, Dr. Johannes Hausinger, Rudolf Holzer, Benjamin Siegert, and Dr. Fritz Wünsch.

For financial support during my PhD, I thank the Deutsche Forschungsgemeinschaft for support via Grants No. GRK 1570 and SFB 631.

I thank my parents, without whose help I would never had the possibility to study

physics, and my two sisters including their families for moral support.

My biggest thanks, however, goes to my girlfriend Judith for her enduring and endless support and for her understanding during all ups and downs of my studies and PhD.

Andreas Scholz
Regensburg
October 2013